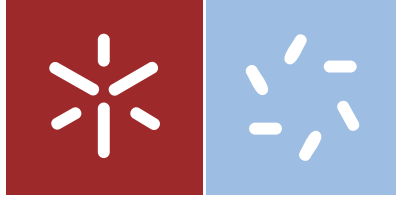




Universidade do Minho
Escola de Ciências

Armando José Barros Ferreira

Development of a pressure sensor
network system for static and dynamic
pressure measurements. Application
to the limb/prosthesis pressure mapping.



Universidade do Minho
Escola de Ciências

Armando José Barros Ferreira

Development of a pressure sensor
network system for static and dynamic
pressure measurements. Application
to the limb/prosthesis pressure mapping.

Tese de Doutoramento em Ciências - Física

Trabalho efectuado sob a orientação do
Professor Doutor José Filipe Vilela Vaz
Professor Doutor Senentxu Lanceros-Mendez

*to my PARENTS,
my wife and my daughters*

Acknowledgements

I would like to thank to Portuguese Foundation for Science and Technology – FCT for the financial support (SFRH/BD/69796/2010) and to University of Minho for providing me all the conditions to develop my work.

It is known that this kind of journey becomes more difficult done alone. There are several people that helped and crossed my way, which I must express my gratitude for all that they represented.

To Professor Filipe Vaz I manifest the sincere gratitude for the opportunity conceded, the enormous contribution to my formation and the transmission of knowledge and experience. For your suggestions and clarifying the ways to go. Not letting to emphasize the friendship dispensed.

To Professor Senentxu thank you for everything you taught me and for every support and encouragement along this journey. For every good mood and the time you dedicated me to help solving all my obstacles along the way. You will be always remembered.

Thank you Professor Maria Teresa Martinez for all your support at the SCIC and availability that you always showed.

Many thanks to Emilia and Cristina for all your support at the CRPG and constant presence throughout these years.

I would like also to all my fellow group members for the team spirit and collaboration. Without you my journey would be much harder, less productive and no fun.

To all the people who somehow had contact with this thesis, thank you.

Last but not least, I would like to leave a warm thank you to my Parents, my wife, Celia, and my daughters, Mariana and Lara, who have the patience and the presence to never fail to encourage and support me in my walk.

Abstract

The present work relates to the development of a sensors network for mapping the pressure fields at the external prosthesis socket/stump interface, in particular at lower limbs. The project consists on the design and implementation of a sensor array from piezoresistive polymer based materials to measure quasi-static and dynamic deformations. The sensors were prepared from poly(vinylidene fluoride) – PVDF and epoxy nanocomposites with carbon nanotubes or nanofibres. The development of thin film-based stretchable electrodes was carried out using the *GLancing Angle Deposition*, GLAD, technique. A specific electronic circuit for signal processing was used with a wireless data acquisition system. Finally, a prototype was designed, constructed and tested in four lower limb amputees, in laboratory conditions, under different types of solicitations at the Vocational Rehabilitation Center - CRPG (Centro de Reabilitação Profissional de Vila Nova de Gaia).

The piezoresistive-based sensors were developed using two different approaches; a) nanocomposites composed of poly(vinylidene fluoride) filled with carbon nanotubes (CNT/PVDF); and b) epoxy resins filled with carbon nanotubes or nanofibres (CNT/EPOXY). The PVDF samples were prepared by hot pressing and spray printing with CNT sample concentrations up to loadings of 10 wt.%. The phase present in the composites CNT/PVDF was the alfa-phase. Due to the fact that external limb prostheses must sustain cyclic loading and unloading during normal walking conditions, the correlation between the electrical resistivity and mechanical solicitations was obtained for different mechanical solicitations, including variations in deformation, temperature and velocity.

In relation to CNT/EPOXY, the electrical response is linear over a wide strain range and the values of the maximum gauge factor is ~ 2.8 . The stability of the signal over 32 cycles, the time response to deformations from 0.1 to 50 mm min⁻¹ and the stable temperature behaviour up to 60 °C shows the viability of these materials to be used as piezoresistive sensors.

In the same way, the electrical and piezoresistive response of CNT/PVDF composites has been studied. The piezoresistive response, quantitatively analysed by the gauge factor, is maximized at concentrations around the percolation threshold, around 2 wt.% loading, and the maximum value of the gauge factor is ~ 6.2 . The piezoresistive response is stable with the number of cycles and reversible up to temperatures below 100 °C. The linearity of the

response over a wide strain range shows the viability of these materials to be used as piezoresistive sensors.

The development of stretchable electrodes was carried out using columnar Ti-Ag thin films with a Ag content of 8 at.% prepared by D.C. magnetron sputtering on CNT/PVDF piezoresistive composites. The Ti-Ag system was chosen to coat the polymers due to some important points related to its characteristics. First of all, Ti-Ag thin films combine the excellent biocompatibility of Ti with the Ag antimicrobial properties, offering also good thermal, electrical, chemical and mechanical properties, together with good wear and corrosion resistance. Secondly, the addition of Ag was also thought in order to tailor the elasticity of the Ti films, allowing a better response of the coated polymer under any particular deformation or stretching of the composite sensor when in-service. Additionally, the deposition of the films by *GLancing Angel Deposition*, GLAD, instead of conventional *Magnetron Sputtering Deposition*, MSD, was also carried to allow and even extend this elasticity resistance. In fact, by depositing films with some particular architectures, inclined, zigzag, etc., there is a real possibility to deposit thin films with extended capacities to resist to stretching or any common deformation that a polymeric-based sensor induce when in-service. Furthermore, there is also the possibility to improve the electrical response of the system and this, all together, to improve the response and the adequacy of the all sensor arrangement in this particular type of applications. By changing the typical columnar growth microstructure, obtained by conventional sputtering, the goal was to tune the mechanical and electrical responses of the materials.

Upon uniaxial stretching of the prepared zigzag thin films, the resistance of the thin film starts increasing smoothly for strains up to 3%. Above 10% strain a sharp increase of the electrical resistance is observed due to film mechanical failure and therefore interruption of the electrical conductivity pathways. The best results were obtained when the polymer was coated with intermediate incident angles ($\alpha = 60^\circ$). The results show that the electrodes structure has a pronounced influence on the overall sensor response leading to values of the *GF* up to 85 mainly due to the electromechanical contribution of the thin film, which stability has to be studied for potential use for sensor applications itself.

Human study was conducted at the Vocational Rehabilitation Center - CRPG (Centro de Reabilitação Profissional de Vila Nova de Gaia). The subjects transfemoral (TF) and transtibial (TT) amputees, walked for 2 minutes in a crosswalk at a relatively comfortable speed of 0.33 m/s. During this time it was possible to simulate a normal walk of

approximately 40 m and the results provided good indications that it is possible to identify areas of critical pressure. Thus, it is expected that the present method will become helpful for comprehensively evaluating the biomechanical conditions of the residual limb and prosthesis interface. The system developed in this project may allow monitoring of the process of rehabilitation with a new prosthesis and will support clinical decisions in relation to the potential effects of modifications on the socket, when adjustments are required.

Resumo

O presente trabalho descreve o desenvolvimento de uma matriz de sensores para mapear as pressões exercidas em próteses externas dos membros inferiores, na interface coto/prótese, baseados em materiais piezoresistivos para medir as deformações dinâmicas e quasi-estáticas. Os sensores foram preparados a partir de nanocompósitos de poli(fluoreto de vinilideno) – PVDF e resinas epoxy com nanotubos – CNT ou nanofibras - CNF de carbono. Adicionalmente, foram desenvolvidos elétrodos estiráveis baseados em filmes finos através da técnica de pulverização catódica GLAD, *Glancing Angle Deposition*. O circuito electrónico usado para o processamento de sinal foi desenvolvido com um sistema de aquisição de dados sem fios. Finalmente, foi construído um protótipo que foi testado em quatro pacientes amputados dos membros inferiores em condições de laboratório, sob diferentes tipos de solicitações no centro de reabilitação vocacional - CRPG (Centro de Reabilitação Profissional de Vila Nova de Gaia).

Com base no efeito piezoresistivo, os sensores foram obtidos usando duas diferentes abordagens; a) compósitos de poli(fluoreto de vinilideno) com nanotubos de carbono (CNT/PVDF); e b) compósitos de resinas epóxi com nanotubos de carbono ou nanofibras (CNT/epóxi). As amostras de PVDF foram preparadas por prensagem a quente e/ou por spray com concentrações de CNT até 10 % em peso. A fase cristalina presente nos compósitos CNT/PVDF foi a fase alfa-PVDF. Foi obtida a correlação entre a resistividade elétrica e as diferentes solicitações mecânicas, através da deformação, da variação da temperatura, da velocidade e do tempo de resposta do compósito.

Em relação aos compósitos de CNT/epóxi, obteve-se uma resposta elétrica linear e os valores de sensibilidade máxima (gauge factor) foram de ~ 2.8 . Através das diferentes solicitações mecânicas, a estabilidade do sinal para mais de 32 ciclos, o tempo de resposta para deformações de 0.1 a 50 mm min⁻¹ e a estabilidade com a temperatura até 60 °C mostram a viabilidade destes materiais para serem utilizados como sensores piezoresistivos. Da mesma forma, a resposta elétrica e piezoresistiva dos compósitos de CNT/PVDF foi estudada. A resposta piezoresistiva foi quantitativamente analisada pela sensibilidade do material (gauge factor) e verificou-se que é máxima para concentrações em torno do limiar de percolação, ~ 2 % de CNT em peso, e o valor máximo obtido foi de ~ 6.2 . A resposta piezoresistiva é estável em função do número de ciclos e reversível até temperaturas inferiores a 100 °C. A linearidade da resposta com a deformação mostra a viabilidade destes materiais para serem utilizados como sensores piezoresistivos.

O desenvolvimento de elétrodos estiráveis foi realizado usando filmes finos com estrutura colunar de titânio e prata - Ti-Ag com um teor de Ag de 8 at.% preparados por pulverização catódica em compósitos piezoresistivos de CNT/PVDF. O sistema Ti-Ag foi escolhido para revestir os polímeros devido a alguns pontos importantes relacionados com as suas características. Primeiro de tudo, filmes finos de Ti-Ag combinam a excelente biocompatibilidade do titânio com as propriedades anti-microbianas da prata, oferecendo deste modo boas propriedades químicas, mecânicas e elétricas, juntamente com boas propriedades de resistência ao desgaste e corrosão. Segundo, a adição de prata também foi incluída com o objetivo de promover a elasticidade do filme de modo a permitir uma melhor adaptação do filme ao polímero. Por outro lado, o sistema GLAD teve por grande objetivo este mesmo propósito: melhorar a resposta elétrica e a elasticidade do sistema de modo a permitir uma melhor adequação à deposição dos elétrodos em materiais flexíveis. A técnica de GLAD foi usada para alterar a microestrutura típica de crescimento colunar obtida por pulverização catódica convencional, *Magnetron Sputtering Deposition*, MSD, em diferentes arquiteturas de crescimento, tais como colunas inclinadas e em ziguezague, a fim de ajustar as respostas mecânicas e elétricas dos materiais. Após estiramento uniaxial dos filmes finos em ziguezague, a resistência elétrica do filme fino começa a aumentar tenuemente para tensões até 3%. Acima de 10% de estiramento dá-se um aumento acentuado da resistência elétrica que é observado devido à falha mecânica do filme. Os melhores resultados foram obtidos quando o polímero foi revestido com filmes depositados com ângulos incidentes intermédios ($\alpha = 60^\circ$). Os resultados mostram que a estrutura dos elétrodos tem uma acentuada influência sobre a resposta global do sensor levando a valores de sensibilidade até 85. Esta contribuição deve-se essencialmente à contribuição eletromecânica do filme fino.

O estudo com Pacientes foi realizado no centro de reabilitação profissional- CRPG (Centro de Reabilitação Profissional de Gaia), com amputados transfemoral (TF) e amputados transtibial (TT), que caminharam durante 2 minutos numa passadeira elétrica com uma velocidade relativamente confortável de 0,33 m/s. Durante este tempo, foi possível simular uma marcha normal de aproximadamente 40m. Deste modo demonstrou-se que é possível identificar as áreas críticas de pressão. Espera-se que, o presente método, se torne útil para avaliar exaustivamente as interações biomecânicas entre o membro amputado e a prótese. O sistema desenvolvido neste projeto poderá permitir o monitoramento durante o processo de reabilitação e apoiar em decisões clínicas em relação aos potenciais efeitos e modificações do encaixe da prótese no coto.

Table of Contents

Acknowledgements.....	v
Abstract.....	vii
Resumo.....	xi
List of figures.....	xv
List of tables.....	xix
List of Abbreviations.....	xix
List of symbols.....	xxi
Framework.....	1
1. Introduction.....	5
1.1. People with incapacities.....	6
1.2. Prosthesis control.....	7
1.2.1. Commercial available systems.....	7
1.2.2. Sensors based on metal.....	10
1.2.3. Piezoresistive sensors based on polymers.....	12
1.2.4. Signal acquisition.....	14
1.2.4.1. The thin film electrode.....	14
1.2.4.2. Readout system for the sensor array.....	16
1.3. Thesis structure.....	18
2. Materials and methods.....	19
2.1. Experimental.....	20
2.1.1. Processing of the materials and composite samples preparation.....	20
2.1.1.1. SWCNT preparation by arc discharge.....	20
2.1.1.2. Functionalization of the SWCNT.....	21
2.1.1.3. Processing of the carbon nanotubes/polymer composites.....	22
2.1.1.3.1. CNT/epoxy composites preparation.....	22
2.1.1.3.2. SWCNT/PVDF composite preparation by hot-pressing.....	24
2.1.1.3.3. CNT/PVDF composites preparation by spray-coating.....	25
2.1.2. Sample characterization.....	25
2.1.2.1. Morphology and CNT dispersion.....	25
2.1.2.2. Thermal properties and degree of crystallinity.....	26
2.1.2.3. Electrical and electromechanical properties.....	26
3. Transducers based on CNT/EPOXY composites.....	29
3.1. Results and discussion.....	30
3.1.1. Composites structural characterization.....	30
3.1.2. Electrical Conductivity.....	32
3.1.3. Electromechanical response.....	33
3.1.3.1. Dependence of the GF with the number of cycles.....	34
3.1.3.2. Dependence of the GF with increasing transversal deformation.....	35
3.1.3.3. Dependence of the GF with increasing deformation rate.....	35
3.1.3.4. Dependence of the GF with increasing temperature.....	36
3.1.4. Conclusion.....	36
4. Transducers based on CNT/PVDF composites.....	37
4.1. Results and discussion.....	38
4.1.1. Composites structural characterization.....	38

4.1.2.	Electrical Conductivity.....	39
4.1.3.	Electromechanical response	42
4.1.3.1.	Effect of CNT concentration	42
4.1.3.2.	Stability of the signal and time response	44
4.1.3.3.	Temperature behaviour.....	45
4.1.3.4.	Physical interpretation of the piezoresistive response.....	46
4.1.4.	Conclusion.....	51
5.	Spray printed CNT/PVDF transducers	53
5.1.	Results and discussion	54
5.1.1.	Morphology and dispersion	54
5.1.2.	Electrical Conductivity.....	55
5.1.3.	Electromechanical response	56
5.1.4.	Conclusion.....	60
6.	Development of stretchable interconnections.....	61
6.1.	Experimental details	62
6.1.1.	Titanium – Silver thin films	62
6.1.2.	Electrical resistance measurements.....	64
6.1.3.	Electromechanical characterization	64
6.2.	Morphological analysis.....	65
6.3.	Results and discussion	66
6.3.1.	Electrical properties of Ti-Ag electrodes	66
6.3.2.	Electrical behaviour of Ti-Ag films under uniaxial stretching	67
6.3.3.	Morphological analyses of Ti-Ag films.....	69
6.3.4.	Electromechanical response of the films.....	71
6.4.	Conclusion	74
7.	Prototype fabrication and testing	75
7.1.	Results and discussion	76
7.1.1.	Sensors construction process.....	76
7.1.2.	Prototyping test.....	77
7.2.	Conclusion	81
8.	General conclusions	83
9.	Future work.....	85
10.	Bibliography.....	87

List of figures

Figure 1: Representation of the main objective and development route of the work.	2
Figure 1.1 Main type of activity limitation, adapted from [2].	6
Figure 1.2: Standard A201 <i>FlexiForce</i> sensor, adapted from [9].	9
Figure 1.3 Metal strain gauge for pressure sensors.	10
Figure 1.4: Percolation route in conductive composites.	12
Figure 1.5: b) Relative change in electrical resistance due to mechanical deformation.	13
Figure 1.6: Schematic representation of the thin film microstructural features.	15
Figure 1.7: Block diagram of the piezoresistive multi-sensor interface circuit.	16
Figure 1.8: Implemented a monitoring platform, for real time sensor monitoring.	17
Figure 2.1: SWCNT soot prepared by the arc discharge method, a) preparation of the graphite electrodes, b) electrodes mounted in the arc discharge apparatus, c) reactor under a helium atmosphere and d) SWCNT soot.	21
Figure 2.2: Reaction route applied for the functionalization of single- and multi-walled carbon nanotubes.	22
Figure 2.3: a) Purification treatment of the nanotubes filtered with a Teflon membrane and washed with DMF and methanol, b) single-walled carbon nanotubes wrapped by Pluronic block copolymer.	23
Figure 2.4: Hot-pressing system.	24
Figure 2.5: Spray-coating system.	25
Figure 2.6: Schematic representation of the 4-point bending tests: z is the vertical displacement of the piston, d is the thickness of the sample (~ 1 mm) and a is the distance between the first and the second bending points (15 mm) and l the distance between the lower supports (45 mm).	27
Figure 3.1: Electron microscopy images of epoxy/CNT nanocomposites; a) fracture edge SEM image of nanocomposite containing 0.5 wt.% CNTs, and b) TEM image of nanocomposite at 0.1 wt.% CNT.	30
Figure 3.2: AFM images of epoxy/CNT nanocomposites specimen at 0.1 wt% CNT loading, a) topography image, b) current mapping.	31
Figure 3.3: Resistance measures from slope of I-V curves (a). Electrical volume resistivity values vs volume fraction of CNT (b).	32
Figure 3.4: Strain applied to a sample and the corresponding resistance variation with time (a), and relative change in electrical resistance due to mechanical deformation, for four up-down	

cycles applied to a sample with 0,5 wt.% CNTs, z-deformation of 1 mm, deformation velocity of 2 mm/min at room temperature. The R-square of the fit is 0.96 (b).	33
Figure 3.5: Sensing resistance of the sample at 0.1 wt.% as a function of time, during a four-point bending experiment consisting of 32 cycles at 1 mm in z-displacement. Only the first 15 cycles are shown.	34
Figure 3.6: <i>GF</i> as a function of the number of cycles (a), z-displacement (b), deformation velocity (c) and temperature (d).	35
Figure 4.1: XRD patterns of a) PVDF (without SWCNTs) and b) the SWCNT(1.7%)/PVDF sample.	38
Figure 4.2: a) Typical I-V curves for the different concentrations of PVDF/CNT samples; b) Electrical conductivity and Gauge factor values as a function of the weight fraction of CNT in samples; c) Typical I-V curves for the different concentrations of PVDF/CNT samples SWCNT – 1,5 wt.%, MWCNTs – 0,75 wt.%, SWCNT – Func. – 4,6 wt.%, MWCNT – Func. – 1 wt.%. d) Concentration dependence of the electrical conductivity for the different composites.	40
Figure 4.3: SEM images of CNT/PVDF composites at 2 wt.%. a) SWCNT, b) SWCNT - Func, c) MWCNT, d) MWCNT – Func.	41
Figure 4.4: a) Strain applied to a sample with 2 wt.% CNT's and the corresponding resistance variation with time, and b) relative change in electrical resistance due to mechanical deformation, for four up-down cycles applied to a sample with 2 wt.% CNTs, z-deformation of 1 mm, deformation velocity of 2 mm/min at room temperature. The R-square of the fit is 0.99.	43
Figure 4.5: Change in <i>GF</i> as a function of the number of bending cycles (left) and test velocity, for a sample with 2 % CNTs.	44
Figure 4.6: Four deformation cycles of 1 mm in z direction; a) room temperature, b) 100 °C, c) 150 °C. d) Gauge factor dependence as a function of temperature for cycles taken at a testing velocity of 2 mm min ⁻¹ for a sample with 2% CNTs.	45
Figure 4.7: Cyclic piezoresistive response as a function of time for a) SWCNT – 1,5 wt.%, b) MWCNT – 0,75 wt.%, c) SWCNT - Func – 4,6 wt.%, d) MWCNT - Func – 1 wt.% for the following conditions: bending of 1 mm, deformation velocity of 2 mm min ⁻¹ at room temperature.	47
Figure 4.8: Relative resistance variation vs. strain curves and the corresponding fit with equation 3 for the determination of the Gauge Factor.	48
Figure 4.9: Surface sensing resistance change $\ln(R(\epsilon)/R_0)$ as function of stress and corresponding fittings with Equation 4.6.	49

Figure 5.1: SEM images of CNT/PVDF composites with 2 wt.% CNT filler content and prepared by a) spray-coating and b) hot-pressing.	54
Figure 5.2: a) Typical I-V plots for the composite samples prepared with CNT at a concentration of 2 wt.% over the percolation threshold; b) Concentration dependence of the electrical conductivity for the different composites.	55
Figure 5.3: a) Cyclic piezoresistive response as a function of time for 2 wt.% CNT content in composites prepared by spray-coating and b) relative resistance variation vs. strain curves and the corresponding fit with for the determination of the Gauge Factor.	56
Figure 5.4: Cyclic piezoresistive response over 100 cycles as a function of time for 2 wt.% CNT content samples prepared by spray-coating and b) change in GF as a function of the number of bending cycles. Experimental conditions: bending of 1 mm, deformation velocity of 2 mm min ⁻¹ , room temperature. The data for the samples prepared after hot pressing are obtained from [52].	57
Figure 5.5: Surface sensing resistance change $\ln(R(\varepsilon)/R_0)$ as function of stress and corresponding fittings with equation 5.3.	59
Figure 6.1: Schematic representation of the GLAD system, where α is the orientation of the substrate relative to the impinging vapor flux.	62
Figure 6.2: Schematic representation of the thin film microstructural features.	63
Figure 6.3: Schematic representation of the experimental configuration of the, a) clamps for the stress-strain experiments with simultaneous electrical measurements for electrical response evaluation of the samples by applying uniaxial stress, b) Representation of the 4-point bending tests (method 2) apparatus where z is the vertical displacement, d is the thickness of the sample and a is the distance between the first and the second bending points (15 mm). The electrodes are in the center of the sample.	65
Figure 6.4 - Electrical conductivity of Ti-Ag films as a function of the incident angle (α) and the number of periods, and electrical conductivity of polymer composite as a function of CNT (wt.%).	66
Figure 6.5: Electrical resistance of the band R as a function of the tensile strain ε of the sputtered Ti-Ag samples for the different incident angles $\alpha = 0, 40, 60$ and 80° and geometries: a) 1 zigzag period; b) 2 zigzags periods.	67
Figure 6.6 - SEM cross-section micrographs of the sputtered Ti-Ag samples for incident angles $\alpha = 0, 40, 60$ and 80° and $\frac{1}{2}, 1$ and 2 zigzags periods.	70
Figure 6.7: AFM topographic images of sputtered Ti-Ag samples with 2 zigzag periods and for different incident angles: a) $\alpha = 40^\circ$; b) $\alpha = 60^\circ$; c) $\alpha = 80^\circ$	71
Figure 6.8: Strain applied to 2 zigzag periods Ti-Ag films deposited on PVDF substrates with 3 wt.% CNT's and the corresponding resistance variation vs. time for four up-down cycles. The	

z -deformation is 1 mm and the deformation velocity is 0.5 mm/min at room temperature.

The incident angle is a) $\alpha = 40^\circ$; b) $\alpha = 60^\circ$ and c) $\alpha = 80^\circ$ 72

Figure 7.1: Sensors construction process, a) Set of sensors was prepared from CNT/ PVDF with 2 wt.% with dimensions of $10 \times 25 \text{ mm}^2$ and 1mm thickness, b) Sensors tested one by one. 76

Figure 7.2: a) Set of sensors connected in an array, b) The block of sensors to monitor the prosthesis. 77

Figure 7.3: Identification of the planes of the body. 78

Figure 7.4: Transducers placed at different planes of the body, subject #1. 78

Figure 7.5: Pressure measured at the stump/sock/socket interface. 79

Figure 7.6: Measurements performed at the stump/sock/socket interface. 80

Figure 7.7: Pressure sensor prototype placement at the stump/sock/socket interface. 80

List of tables

Table 1-1: Commercially available activity monitors [8-10].	8
Table 1-2: Advantages and disadvantages of sensors with foil strain gauge [25].	11
Table 2-1: Preparation of anode with graphite electrodes and Ni/Y catalysts (4/1 atomic %).	20
Table 4-1: GF values resulting of the linear fit of $\Delta R/R_0$ as function of stress.	47
Table 4-2: Distance between two CNT, results of Equation 4.6 as function of stress.	50
Table 5-1: <i>GF</i> values obtained from the linear fit of $\Delta R/R_0$ as function of stress.	57
Table 5-2: Distance between two CNT, results of Equation 5.3 as function of stress.	59
Table 6-1: Surface roughness of the Ti-Ag films with different incident angles of deposition and 2 zigzag periods.	71
Table 6-2: <i>GF</i> values resulting of the linear fit of $\Delta R/R_0$ as function of stress ε .	73
Table 7-1: Patients studies of internal pressures in a transfemoral and transtibial amputee of the residual limb.	77

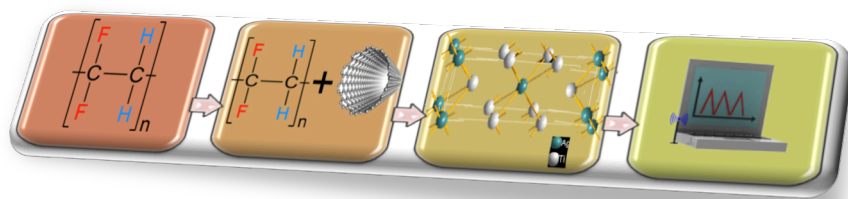
List of Abbreviations

ADC	Analogic digital converter
Ag	Silver
AFM	Atomic Force Microscopy
CB	Carbon Black
CNF	Carbon Nanofibers
CNT	Carbon Nanotubes
CRPG	Centro de Reabilitação Profissional de Gaia
DC	Direct Current
DDS	4,4'-diaminodiphenil sulfone
DMF	N,N-dimethylformamide (Merck 99.5%)
DSC	Differential scanning calorimetry
GF	Gauge Factor
GLAD	Glancing Angle Deposition
MC	Microcontroler

MCU	Microcontroller unit
MP	Metal Powder
MSD	Magnetron Sputtering Deposition
MWCNT	Multi-Wall Carbon Nanotubes
Ni	Nickel
NIR	Near infra-red
PAM	Patient Activity Monitor
PDMS	Polydimethylsilicone
PVDF	Poly(vinylidene fluoride)
RF	Radio frequency
SDBS	Sodium dodecylbenzene sulphonate
SEM	Scanning electron microscopy
SPI	Serial peripheral interface
SWCNT	Single Wall Carbon
T	Temperature
TEM	Transmission electron microscopy
Ti	Titanium
TiO ₂	Oxide-base matrix
T _g	Glass transition temperature
TGAP	triglycidyl-p-aminophenol
TF	Transfemoral
TT	Transtibial
USB	Universal serial bus
XRD	X-ray diffraction
Y	Yttrium
α-phase	Conformation trans-cis PVDF
ΔH _m	Melting enthalpy
ΔX _c	Degree of crystallinity

List of symbols

D	Length of the electrode
d	Film thickness
ε_1	Strain
L	Distance between the electrodes
r	Radius of curvature
R	Surface resistance
α	Orientation of the substrate relative to impinging vapor flux
β	Column angle
λ_c	Mean free path of the film
ν	Poisson ratio
ρ	Sheet resistivity
σ	Electrical conductivity



Framework

Body movements impose static as well as dynamic loads upon mechanical devices. External limb prostheses sustain cyclic loading and unloading during normal walking conditions, which is superimposed on the loading caused by the body weight. The prostheses transmit the forces through the body/device interface. If this transmission is inefficient it can cause pain and uncomfortable situations to the user. A pure static overload seldom occurs in well-designed and properly applied prostheses. However, the dynamic load character may cause failures on the prosthesis and affect the skin and stump condition. Dynamic measurements of strain, taken regularly, are reliable indicators of potential failure. Besides that, prostheses strain and stress monitoring is also very useful with well performing prostheses providing valuable information on the prosthesis varying environment.

Figure 1 shows the main objective of this work, which is the development and implementation of materials and devices capable of monitoring the pressure distribution on custom-made sockets for lower limb prosthetics. Custom made medical devices need strict control in all production phases, and for the object of the project – lower limb prostheses- the control is nowadays mainly performed by qualitative methods. There is thus an increasing need to improve the quality in selecting, producing, adapting and using the product, by applying quantitative methods of control.

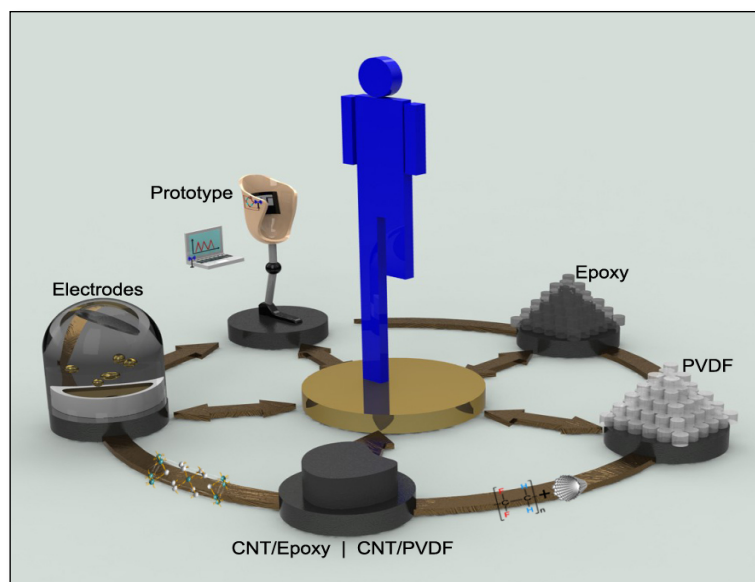


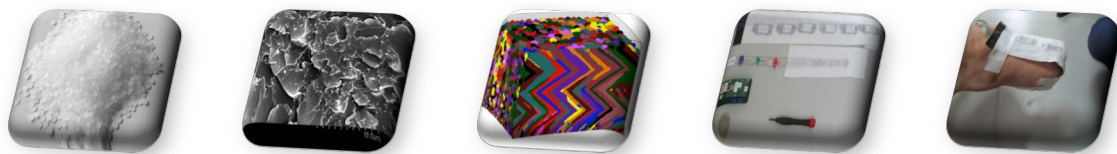
Figure 1: Representation of the main objective and development route of the work.

The knowledge of force distribution within the socket helps the practitioner to assess the fit of the socket on an object in a reproducible and systematic way, helping to reduce the time and materials used on this step, and leading to improve substantially the comfort and

quality of life of the end user. If the validation information is stored, comparisons inter and intra subjects may help to the assessment for different socket types and production methodologies. On a subsequent step it will allow to improve force distribution within the socket. For that, polymer composites were prepared based on epoxies and thermoplastics filled with carbon nanotubes or nanofibres, close to the percolation thresholds. In order to increase their compatibility with organic polymers and to improve processability, CNT are often functionalized with organic chemical groups. These composites were subjected to experimental sets of cyclic loading and unloading simulating normal walking conditions. After its preparation, the piezoresistive polymers to be used in the prostheses were subjected to an experimental protocol of optimization of a metallic-like coating that is expected to be compliant and stretchable. The depositions were carried out by co-sputtering (varying amounts of silver pellets were placed within the erosion zone of pure Ti targets).

The sensor configurations developed in this work were further connected in an array to monitor the prosthesis dynamic forces. The data acquisition system was based on National Instruments hardware and LabVIEW software. A specific electronic circuit for signal processing was used. To support the field tests, a wireless data acquisition system for a reduced number of channels was used.

Finally, the prototype was tested at the CRPG – *Centro de Reabilitação Profissional de Vila Nova de Gaia* by selected patients under different solicitations.



1. Introduction

This chapter presents the main topics related to the present thesis. A contextualization of the work is provided in accordance to current needs. The general and specific objectives of the study are defined together with the main structure of the document.

1.1. People with incapacities

The history of people with incapacities is an important chapter of the history of social discriminations. People with debilities have been the object of preconception and discrimination along the History and in different cultures. The negative discrimination is a powerful factor for generating inequalities and consequently the exclusion from society life. The growing process of rationalization of social life, associated to the emergence of industrialization and capitalism, favoring the increase in social differentiation and specialization, lead to a social and administrative definition of disability [1].

In Portugal there are no exact statistics about the number of existing amputees, the last one (*CENSOS 2001*) refer they have in Portugal about 6.1 % of the population with disability, and these 1.5% have some kind of disability with mobility, Figure 1.1 [2]. From the group of people using some technical aid/assistive product, 70.8 % use assistive products for personal mobility and 33.1 % used orthosis and/or prosthesis, the distribution by regions in Portugal Continental is 10 % in the Northern region, 7.8 % in Alentejo, 7.5 % in Lisbon and 7.7% in the Islands [1].

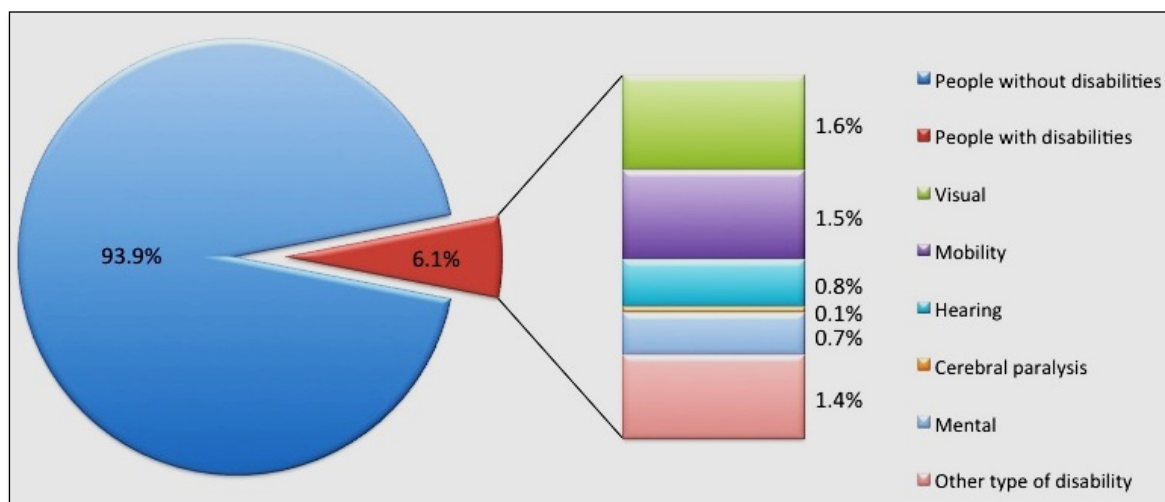


Figure 1.1 Main type of activity limitation, adapted from [2].

The promotion of health and quality of life associated to the functionality and physical activity represents a challenge for the scientific society. The diagnosis and assessment of the person and context, to identify the needed of interventions related to the production and adaptation of medical devices to individual characteristics, are essential phases that contribute for the success of the individual life project.

Body movements impose static as well as dynamic loads upon mechanical devices. In

particular, external limb prostheses sustain cyclic loading and unloading during normal walking conditions, which is superimposed on the loading caused by the body weight. The prostheses transmit the forces through the body/device interface. If this transmission is inefficient it can cause pain and uncomfortable situations to the user. The production of the prosthesis fitting to amputees implies alignment of the socket and structure under specific parameters. These assessments are performed using qualitative methods, which are not reliable and are based on the experience of the practitioner. The results of the non-adequate fit of the prosthesis are poor static and dynamic weight support, gait deviations and non-efficient gait. As a consequence, in most cases, there is overload of the non-amputated side and high-energy consumption. In extreme situations the amputee stops using the device [3].

1.2. Prosthesis control

The production of a socket is, with traditional methods, a long process: negative plaster mold, positive mold and rectification, transparent socket check and, if necessary, revision sockets, before a definitive socket is produced. The socket may be considered as the most important prosthetic component, as it ensures correct suspension of the prosthesis and adequate transmission of forces during gait. However socket fit is usually assessed by the subjective information given by the amputee and visual inspection of excessive pressure areas within the transparent socket walls. The possibility of having a direct, real-time method of assessing the pressure distribution and/or relative distribution can contribute significantly to the efficiency and efficacy of the process and therefore reduce the associated costs and increase the quality of life of the patients.




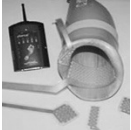






1.2.1. Commercial available systems

The purpose of a sensor is to provide information about physical, chemical or biological environments. In the field of physical environments, the use of the electromechanical coupling effects, such as piezoelectric, electrostrictive, magnetostrictive or piezoresistive materials [4-6], among others, constitutes a very attractive application for strain or strain-rate measurements in mechanical and structural monitoring.

In terms of prosthesis control, the first available systems (Table 1.1) were the simple

walking controller (Step-o-meters or Step Counters) and the PAM (Patient Activity Monitor) system [7], which measures the amputee's walking activity over prolonged periods of time. The Pliance-RLS system [8], which measures the pressure at the residual limb/socket interface during static and dynamic movements. The PEDAR system [8], which captures tridimensional trajectories of the patients by using a set of infrared cameras. And finally the EMED platform [8], which are electronic systems that record and evaluate pressure distribution under the foot in static and dynamic conditions. Recently, there are some systems in the market that allow to have an idea, at least qualitative, about the field of pressures that are felt by the patient. One of such systems is the pressure sensor from Tekscan [9], which is a resistive-type sensor that detects the pressure that is developed in the prosthetic when the patient moves. They are very thin (not interfering with the socket placement), simple to manufacture and relatively cheap.

Table 1-1: Commercially available activity monitors [8-10].

	<p>PAM™ : (Patient Activity Monitor)</p> 	<p>Developed specifically for the Orthotist & Prosthesis industry.</p>	<p>Time spent not active, active, and locomotion. Total number of steps taken. Average step length. Distance travelled. Maximum speed in locomotion. Average speed in locomotion. Impact.</p>
	<p>Pliance-RLS</p> 	<p>Developed for socket evaluation and fit.</p>	<p>Quantification of the level of pressure at the residual limb/socket interface during static and dynamic movements.</p>
	<p>Pedar</p> 	<p>For monitoring local loads between the foot and the shoe.</p>	<p>System extremely mobile and flexible to meet virtually all testing</p>
	<p>Emed</p> 	<p>Measure foot pressure in static and dynamic mode.</p>	<p>Can be used as a general diagnostic tool to describe plantar pressures.</p>
	<p>F-Socket System</p> 	<p>Developed to the needs of the Orthotist & Prosthetist professional by enabling improved design, fit, and function of prosthetics.</p>	<p>Provides pressure profiles and graphical displays for quantitative analysis. Examines the formation of pressures within the socket interface during the various phases of gait allowing you to modify the socket/stump interface accordingly.</p>

Most of these systems are used only in terms of controlling the walking characteristics; these kinds of sensing systems are particularly sensitive to low range dynamic pressure fields. Thus, when in static position or in slow walking, bending or any other kind of static movements of the body, the sensing device has very limited accuracy and does not give adequate information about the pressures at the patient's stump. Moreover, the device from Tekscan is known to be non water-proof (meaning that it may be destroyed by sweat) and having severe problems when used for high loads. Another serious problem about these sensors is related with the existence of creep and high hysteresis effects [11-13]. Therefore, these sensors are also known for repeatability problems, signal drift and cross-talk problems [11-13]. Besides, another problematic issue about these types of sensors relies on the proper manufacturing itself. Figure 1.2 shows the individual layers of the standard sensor construction.

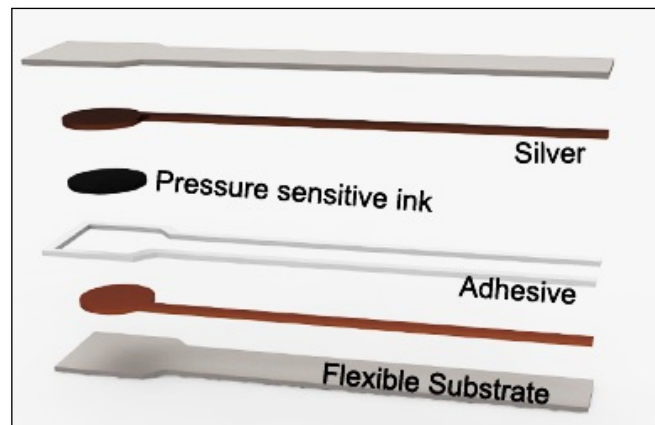


Figure 1.2: Standard A201 *FlexiForce* sensor, adapted from [9].

The sensor is composed by two layers of polyester film, where a conductive material (silver) is applied on each layer. Then an adhesive is used to glue the two layers of the substrate together to form the force sensor. The silver circle on top of the pressure-sensitive ink defines the active sensing area. This sensor fabrication technique implies, according to Tekscan [9], that shear-stresses are a major problem, leading to detachment of the two layers and thus malfunctioning problems of the sensing units. Bending of the glued layers is also a source of proper signal acquisition problems.

A second type of sensors that are recently launched in the market are those from NOVEL [8], Table 1.1, which are constituted by a matrix of sensors that allow their insert in the prosthesis itself and acquire a set of results related with the field of pressures that are present during the patient's move. This second type of sensors are of capacitive type and thus

sensitive to the change of sensing area. Relatively to these sensors, comparative research papers [11-13] show that they are better than Tekscan ones, but again with some problems related with high compliance and their relatively high prices [11-13]. Beyond these, these sensors are thicker than the Tekscan ones, and thus may interfere with the prosthesis and patient comfort (1 mm against < 0.3 mm) [11-13]. Although quite innovative, there are some problems related with their limited sensing capacities for high-pressure measurements.

1.2.2. Sensors based on metal

Several methods are relatively specific for a given application and only a few are applicable to a wide range of materials and surfaces [14-16]. The main parameter to be taken into account in strain sensing applications is the sensitivity to strain, expressed quantitatively as the gauge factor [17]. Most metals have gauge factors around 2.0–3.2 [18], in the case of the silicon semiconductor, can be 120, depending of on the temperature, doping level and crystalline structure, among other factors. Further, devices based on silicon have been fabricated with gauge factors as high as 843 [19]. Several technologies have been proposed to develop strain sensors, pre-stressed metal conductors [20, 21] or in plane patterned metal conductors [22, 23]. Metals can be deposited in thin layers on a broad range of substrates by electron beam evaporation, cathodic sputtering or electroplating and patterned down to the nm scale using photolithographic processes [24].

Perhaps the most popular version is the foil-type gauge, produced by photo-etching techniques and using similar metals to the wire types (alloys of copper-nickel (Constantan), nickel-chromium (Nichrome), nickel-iron, platinum-tungsten, etc.). Typical strain gauge patterns are shown in Figure 1.3. A zigzagged conductor path is commonly used to effectively increase the length of the resistor and the total resistance under a given area.

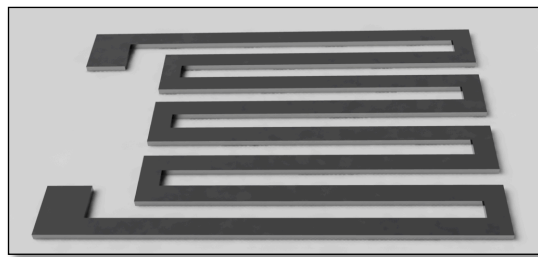


Figure 1.3 Metal strain gauge for pressure sensors.

However, these sensors have usually high densities, are mechanically fragile, show very limited flexibility and are difficult to shape. They typically require complex manufacturing processes and are not suitable for large area applications. Table 1.2 indicates the advantages and disadvantages of some of such sensors.

Table 1-2: Advantages and disadvantages of sensors with foil strain gauge [25].

Type of sensors	Advantages	Disadvantages
Metal strain gauges	Resistant to vibrations Low cost Adaptability to various technology applications Simple to implement	Problems attaching the foil gauges to the sensing element Low gauge factors
Gauges with deposited film	Resistant to vibrations Good stability Low cost Relatively simple technology	Sensitive to electric overloads Average integration potential, especially for thick layer gauges
Gauges with diffused piezoresistors	High gauge factor High potential for integration: possibility of producing a diaphragm Cost reduced by mass production	Operation temperature limited to approx. 120°C
Standard capacitive pressure sensors	Compactness Low drift High bandwidth	Sensitive to stray capacitance Sensitive to vibrations
Capacitance thin – film sensors	Compactness Resistant to vibrations High bandwidth: 50 to 200 kHz	Sensitive to temperature
Conversion by piezoelectric effect	Large bandwidth Possible miniaturization	High sensitivity to temperature Processing of low-level signals is necessary Need for special connecting cable for dynamic measurements Cannot measure static pressures
Oscillator with vibrating blade or cylinder	Information carried by the frequency High output signal Excellent repeatability Excellent resolution Excellent precision Low cost	Large size Limited bandwidth
Optical conversion	Good resistance to mechanically and electrically harsh environments Remote electronics	Very expensive Low accuracy

These facts led to the development of piezoresistive polymer based sensors, than can overcome the aforementioned limitations. Polymer based piezoresistive sensors are typically based either in conductive polymers [26] or in polymer composites with conductive fillers [27].

1.2.3. Piezoresistive sensors based on polymers

In recent years, studies about polymer based smart materials, and particularly about polymer sensors, are strongly growing in terms of financial investment, published articles and number of active researchers [28-31]. Polymeric materials are known to be able to increase functionality by adding to their mechanical response varying electrical properties, which are typically achieved by suitable nanofillers [5, 6, 32]. The materials most commonly used as conductive fillers include Carbon Black (CB) [33, 34], Metal Powder (MP) [35], Carbon Nanofibers (CNF) [36] and Carbon Nanotubes (CNT) [37], among others. In particular, the concentration region around the percolation threshold shows suitable characteristics for strain sensor applications [38, 39]. The variation of electrical conductivity of composites with increasing filler concentration can be divided into three regions, as shown in Figure 1.4. In the first phase, the electrical conductivity is very low due to the low conductive filler content, as shown in Figure 1.4 (zone a). The electrical conductivity of the composites is thus close to that of the polymer matrices. However (Figure 1.4 (zone b)) increasing filler concentration leads to the formation of large interconnected clusters of fillers. Consequently, in this region “b”, the electrical conductivity of the composites increases gradually. As demonstrated later this phase “b” is very important for the strong piezoresistive response of the composites. In the third region, as the amount of fillers increases, the electrical conductivity of composites increases remarkably following a percolation power law.

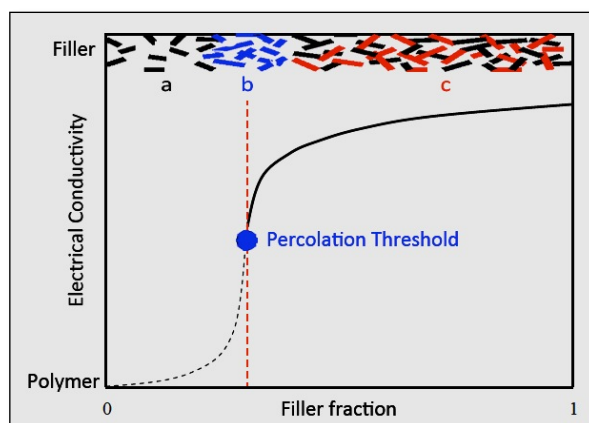


Figure 1.4: Percolation route in conductive composites.

The volume fraction of filler particles at this concentration is called the percolation threshold. At the percolation threshold concentration, in contrast with the classical percolation theory that just includes the formation of a contact network [40], conducting

inclusions such as the filler are sufficiently close to each other to be within the tunneling distance to create a conducting network [41-43]. So, three possible contributions are considered to play a role in the physical mechanism responsible for the piezoresistive response of CNT/polymer composites:

- Variation of the conductive networks formed by CNT, e.g., loss of contact among CNT, under the applied strain [44, 45];
- Tunneling resistance change in neighboring CNT due to strain induced distance variations among CNT [44, 46-48];
- Piezoresistivity of CNT themselves due to their deformation [49-51].

The first two contributions are maximized in composites with filler concentrations close to the percolation threshold and the overall piezoresistive properties of CNT composites are therefore determined by CNT dispersion and interactions between the CNT (CNT network). The third contribution corresponds to the intrinsic piezoresistive effect of individual CNT. Consequently, the study of the piezoresistive response of the composites is of critical importance also in order to bring some insights on the basic conduction mechanism and electrical properties of the composites. A common feature of these piezoresistive composite is that, as a result of straining, they exhibit a fairly linear and reversible electrical resistance change [52], Figure 1.5, and, most important, as compared to conventional strain sensors, such as strain gauges, a relatively higher sensitivity has been observed [53].

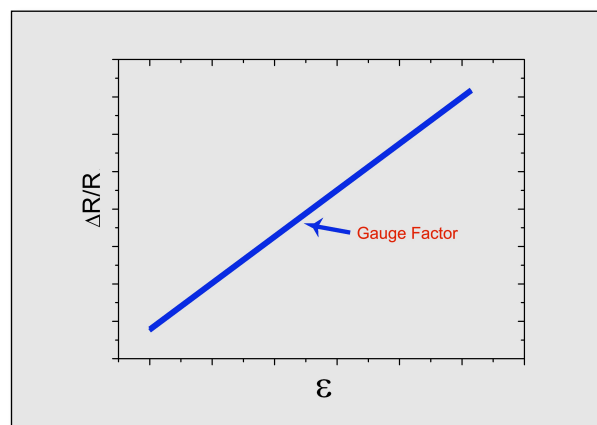


Figure 1.5: b) Relative change in electrical resistance due to mechanical deformation.

Following this idea, some works have demonstrated that after direct dispersion of individual CNT in a polymer, the electrical resistance of the resulting composite changes with strain [39, 47, 54]. The type and characteristics of the conductive filler and polymer matrix

material have strong influence on the piezoresistive response and therefore on the application potential. About a decade ago, a significant correlation between a reversible mechanical deformation and electrical resistance of single- and multi-walled carbon nanotubes was discovered, showing that CNT composites may be used as accurate strain (or stress) nano, micro and macroscale sensors [55, 56].

Composite materials can be developed with the ability to change significantly the electrical response when subjected to strains, which is suitable for the development of high sensitive polymer-based strain sensors [55-57]. However, one of the critical issues of these sensors is the reliability of the electrodes, which link the responsive polymer composite to the signal acquisition circuit. This is particularly challenging given the relatively high and complex mechanical solicitation expected for these applications, i.e. bending, elongation and torsion. In fact, these sensors must be reliable and retain reproducibility and structural integrity over their lifetime. Furthermore, corrosive and mechanical failures must not occur. Thus, these materials, though not selected exclusively at the base of their mechanical and chemical properties, must provide adequate mechanical and chemical resistance that arise in any given application.

1.2.4. Signal acquisition

1.2.4.1. The thin film electrode

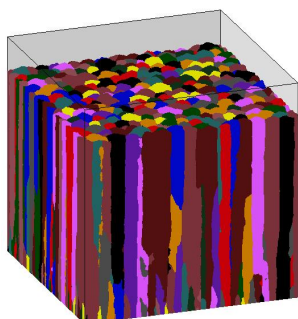
As previously mentioned, composite materials can be developed with the ability to significantly change the electrical response when subjected to strains, which is suitable for the development of polymer-based strain sensors [55-57]. However, one of the critical issues of large strain sensors is the reliability of the elastic interconnections between the polymer composite and the signal acquisition circuit. This is particularly challenging given the relatively high and complex mechanical loadings expected for these applications, i.e. bending, elongation and torsion. These devices must be reliable, with structural integrity and retain that integrity over their lifetime. Furthermore, corrosive and mechanical failures must not occur. Thus, these materials must provide adequate resistance to the mechanical and chemical degradation during applications. Several technologies have been proposed in recent years, including the use of intrinsic conductive polymers [58, 59], pre-stressed metal conductors [20, 21] or in plane patterned metal conductors [22, 23].

Currently, metals can be deposited in thin layers on a broad range of substrates by electron beam evaporation, cathodic sputtering or electroplating and patterned down to the nm scale using photolithographic processes. These processes are the best options to realize these interconnections because of their high electrical performance and relatively low cost. Though, in all cases, the main challenge is maintaining the integrity of the electrodes under mechanical solicitation. Reproducible results at a large throughput can be obtained with these methods, which consequently have the potential of moving the technology from the lab to the industry. In order to produce the electrodes, there are two major obstacles to the direct use of metallic thin films:

1. The Young modulus of metals is some orders of magnitude higher than that of polymers (50–100 GPa compared to 0.2–1 MPa) [60];
2. The limit of elasticity for metals is around 2%. If a metal electrode is strained above this limit it will crack and form islands separated by non-conductive polymer [60].

Concerning the thin film preparation, the microstructure of the films strongly depends on the experimental parameters used during the deposition [61-64]. In conventional Physical Vapor Deposition (PVD) techniques, the normal incidence of the particles flux restricts the films growth, Figure 1.6 a), which is typically columnar and normal to the substrate. Offering countable benefits comparatively to the conventional sputtering techniques, the GLancing Angle Deposition technique (GLAD), first reported in 1959 by Knorr and Hoffman [65], is an original way to modify many physico-chemical properties of thin films, Figure 1.6 b).

a) Conventional growth



b) Zigzag growth

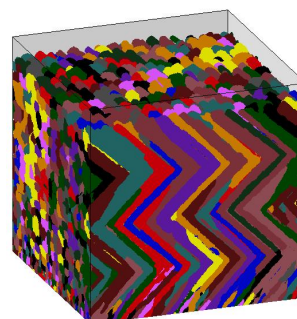


Figure 1.6: Schematic representation of the thin film microstructural features.

Indeed a wide range of morphologies can be tailored combining oblique incidence of the depositing species and substrate motion. Beyond the specific nature and characteristics of

the chosen polymer sensing material, the metallic film selected to coat the polymeric sensor, as well as the production method, should be carefully thought out. Based on previous works [66, 67] and given the large potential of this device in the biomedical field, the Ti-Ag system was chosen to coat the polymers. The Ti-Ag thin film system combines the excellent titanium biocompatibility with the silver antimicrobial properties, offering good thermal, electrical, chemical and mechanical properties, together with good wear and corrosion resistance [68-70].

1.2.4.2. Readout system for the sensor array

For integration as a part of the electromechanical sensor system applied to the lower limb prostheses, and in order to allow measurement of the deformation and the movement of the gait, it is necessary to use a readout system appropriate for this specific application. The data acquisition system was based on National Instruments hardware and LabVIEW software.

The sensor interface should be highly configurable to allow the control system to adjust the condition circuit to the sensor to read. This is important as, although all electromechanical sensors show variation of their resistance when subjected to a deformation, the initial resistance of the various sensors is not the same and therefore the resistance variation is not identical either.

The readout system for the sensor array is shown in Figure 1.7. This microsystem uses a total open architecture and a key feature of this circuit is to use a single read circuit for all sensors which enables a substantial reduction in implementation area.

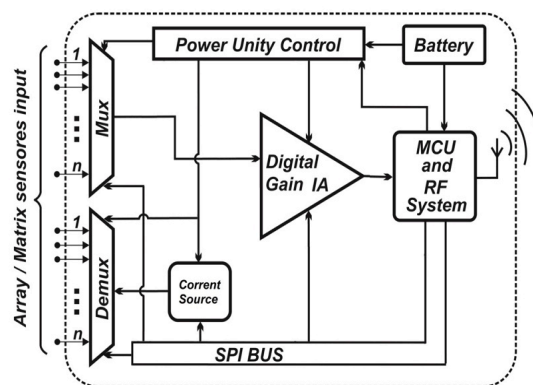


Figure 1.7: Block diagram of the piezoresistive multi-sensor interface circuit.

In this system (Figure 1.7), the various sensors are connected to a multiplexer circuit that allows to read each sensor independently, ensuring that the rest are in open circuit and

that, therefore, do not affect the measurement and there is no power consumption. A multiplexing circuit for eight channels was implemented, which is easily expanded to a large number of channels as the readout circuit is completely independent of the number of input channels. In this configuration, one end of the sensor is connected to a controlled current source and the other end connected to programmable gain application circuit. In this way, the source injects a constant current through the sensor, which by varying the sensor resistance causes a voltage change at the entrance of the amplifier. After signal amplification, this is measured through an analog-to-digital converter (ADC), incorporated internally in the microcontroller (MC). This MC is also responsible for the activation of the measuring sensors as well as for the control of current and amplification gain for each enabled channel. The MCU communication with the various blocks of the readout circuit is performed using a serial peripheral interface (SPI) bus which allows to control all circuit devices quickly and with a minimum of connections.

The measured data are sent via radio frequency (RF) to a remote platform responsible for data recording, allowing deformation measuring by the various sensors in real time and without requiring a physical connection. For this purpose, a monitoring platform was implemented (Figure 1.8) to run on a computer, which is connected to the RF receiver module with a universal serial bus (USB) connection with a frequency of acquisition of 20 Hz.

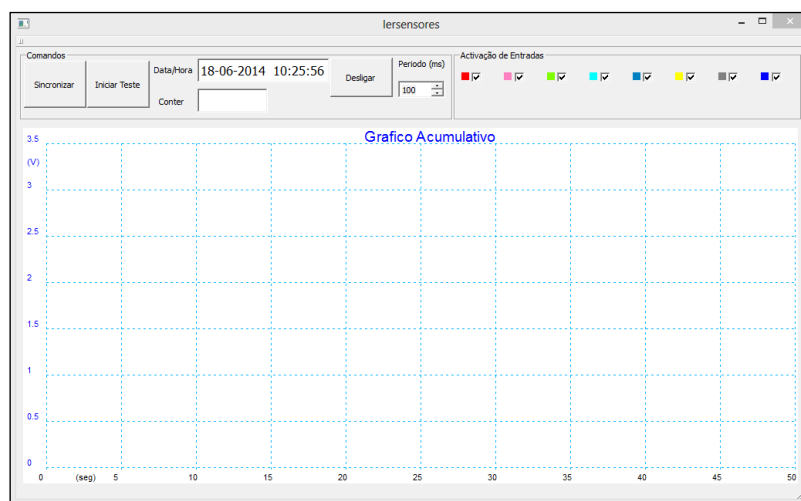


Figure 1.8: Implemented a monitoring platform, for real time sensor monitoring.

The development platform allows visualizing the response of the various sensors instantaneously and performs the recording of the entire measurement period in a file for a

later detailed analysis. It is important to note that the developed architecture was implemented using commercial electronic components, which enable a quick transition from the architecture to the functional prototype, and thus able to evaluate how the developed system meets the requirements.

1.3.Thesis structure

This thesis is divided into 9 chapters to provide a logical sequence of the developed work during this research. 4 of the 9 chapters are based on published scientific papers focused on the development of materials for sensors applications.

The chapter 1 describes a general contextualization of the work is provided in accordance to current needs. The general and specific objectives of the study are defined together with the main structure of the document. The objectives of the study are also presented as well as the structure of the thesis report.

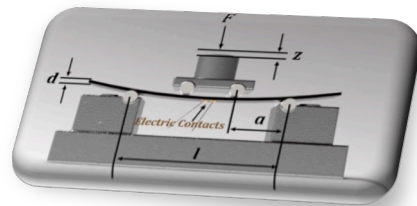
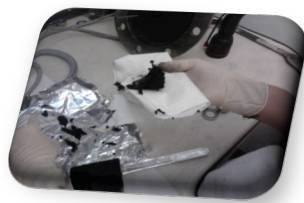
The chapter 2 provides a description of the experimental procedures, including used materials and preparation methods of the samples, the experimental techniques carried out to characterize morphological, thermal, mechanical and electrochemical properties of the samples, as well as the procedures used to test the performance of the materials for the intended applications.

The chapters 3, 4 and 5 report the study of the influence of SWCNT and MWCNT fillers, respectively, in the morphological, thermal, mechanical and electrochemical properties of the PVDF composite for sensors applications. All these chapters are based on published scientific papers.

The chapter 6 report the main characteristics of the nanostructured functional of Ti-Ag electrodes produced in GLAD system in order to be applied to the polymer composites. This chapter are based on published scientific paper.

The chapter 7 report the fabrication of the sensor array prototype and its tests at the CRPG - Centro de Reabilitação Profissional de Vila Nova de Gaia (Vocational Rehabilitation Center).

The chapter 8 and 9 provides some final remarks by, the general conclusions of the study as well as the future work perspectives.



2. Materials and methods

This chapter provides a description of the materials used in this investigation, as well as the experimental details on sample preparation. The experimental conditions for the characterization of the morphological, thermal, electric and electromechanical properties of the prepared samples are also presented.

2.1. Experimental

2.1.1. Processing of the materials and composite samples preparation

Conductive fillers are typically incorporated into various polymers to fabricate conductive polymers composites. With increasing conductive filler content, a strong increase in the electrical conductivity can be observed when a critical filler content is reached in the polymer matrix. The preparation of these polymer composites involves the selection of a conductive filler and the preparation method. Processing of fillers and composites are described in this chapter.

2.1.1.1. SWCNT preparation by arc discharge

SWCNT soot was prepared by the arc discharge method, using graphite electrodes and Ni/Y catalysts (4/1 atomic %), table 2.1, Figure 2.1a). In the used electric arc-discharge apparatus, the arc is generated between two electrodes in a reactor under a helium atmosphere Figure 2.1b, c). The cathode was a graphite rod (16 mm diameter, 40 mm long) and the anode was also a graphite rod (6 mm diameter, ~ 8 mm long) in which a hole (3.5 mm diameter, ~ 40 mm deep) had been drilled and filled with a mixture of a metallic catalyst and graphite powder. The arc discharge was created by a current of 100 A; a voltage drop of 30V between the electrodes was maintained by continuously translating the anode to keep a constant distance (~ 3 mm) between it and the cathode. As-grown SWCNT soot, Figure 2.1d), was previously characterized [71, 72] and was used without further purification. Metal content in the as-grown SWCNT sample was ~ 20 wt.%, as determined by plasma spectroscopy [71].

Table 2-1: Preparation of anode with graphite electrodes and Ni/Y catalysts (4/1 atomic %).

Graphite rod	Initial weight (g) (± 0.005)	Length (mm) (± 0.05)	Drill depth (mm) (± 0.05)	Final weight (g) (± 0.005)
1	4.11	74.0	42.2	3.43
2	4.35	78.4	38.0	3.73
3	4.38	79.0	38.3	3.75
4	4.41	79.4	39.1	3.77
5	4.21	75.4	39.1	3.56
6	4.48	80.6	39.2	3.83
7	4.66	84.2	39.1	4.02

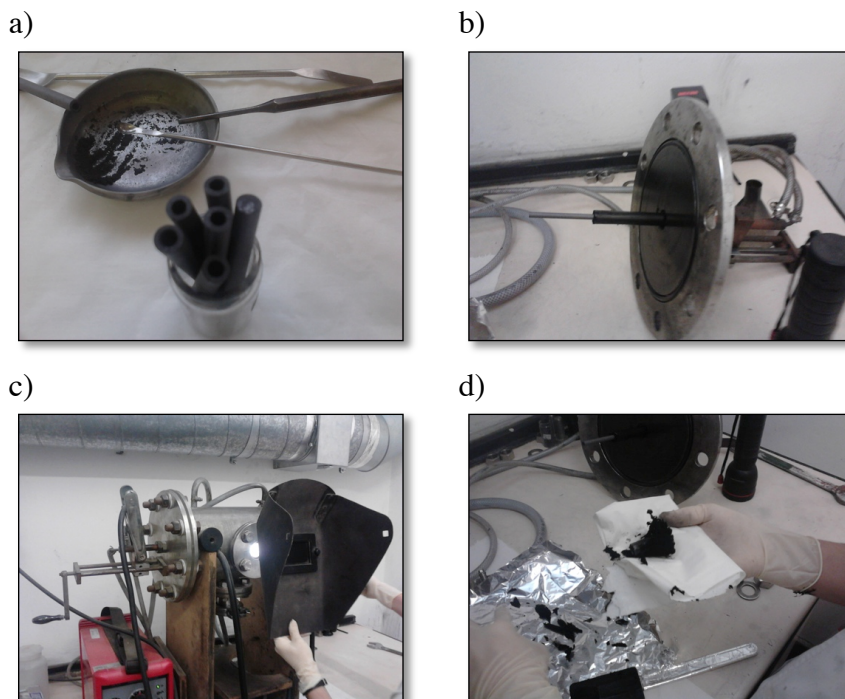


Figure 2.1: SWCNT soot prepared by the arc discharge method, a) preparation of the graphite electrodes, b) electrodes mounted in the arc discharge apparatus, c) reactor under a helium atmosphere and d) SWCNT soot.

2.1.1.2. Functionalization of the SWCNT

The SWCNT (AP-SWNT grade) were purchased from Carbon Solutions Inc., Riverside, California. This SWCNT powder material is synthesized by the electric arc reactor method using Ni/Y catalyst and contains ~ 30 wt.% metal residue. The average diameter and length of the SWCNT is 1.89 nm and 509 nm, according to atomic force microscopy measurements [73]. Multi-walled carbon nanotubes (MWCNT, NC 7000) were provided by Nanocyl, Sambreville, Belgium. The Nanocyl 7000 series is produced by chemical vapour deposition process and contains < 10 wt.% metal oxides. The average diameter and length of the NC 7000 MWCNT is 9.5 nm and 1.5 μm (transmission electron microscopy data supplied by Nanocyl).

CNT functionalization with heptafluorooctyl phenyl groups was accomplished by reaction with the corresponding in situ generated diazonium compound. The reaction route is indicated in Figure 2.2.

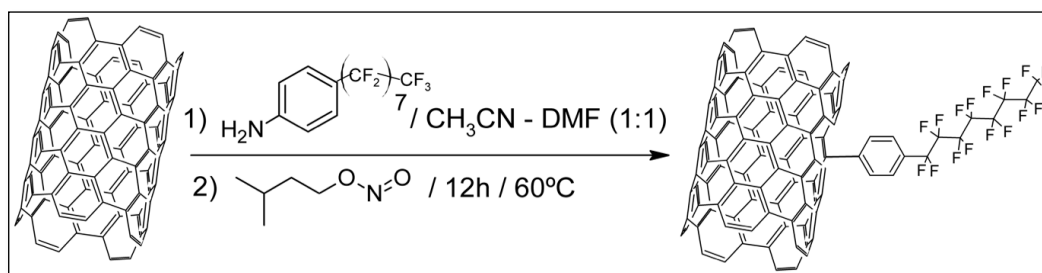


Figure 2.2: Reaction route applied for the functionalization of single- and multi-walled carbon nanotubes.

250 mg of CNT were tip sonicated in 50 mL of N,N-dimethylformamide (DMF, Merck 99.5%) for 60 min. Separately, 460 mg of heptadecafluorooctyl aniline were dissolved in 50 mL of acetonitrile and added to the CNT dispersion. The mixture was heated to 60°C under constant magnetic stirring, and then 2 mL of isoamyl nitrite was added. The reaction mixture was left overnight at 60 °C, and then vacuum filtered through a 0.1 μm Teflon membrane and washed with DMF and methanol. A thorough characterization of fluoroalkyl-functionalized SWCNT and MWCNT has been previously reported [72, 74]. Thermogravimetric studies revealed that the degree of functionalization was of 1 functional group per every 520 and 648 carbon atoms in the SWCNT and MWCNT, respectively.

2.1.1.3. Processing of the carbon nanotubes/polymer composites

2.1.1.3.1. CNT/epoxy composites preparation

The epoxy system is composed by a trifunctional epoxy precursor, triglycidyl-p-aminophenol (TGAP) and 4,4'-diaminodiphenil sulfone (DDS) as the curing agent. The nanotubes were subjected to a purification treatment consisting of a thermal treatment in air atmosphere at 350 °C for 2h. Then, the as-oxidized nanotubes were dispersed in an aqueous solution of Pluronic F68 block copolymer (0.5 wt.% in deionized water) by tip sonication (Hielscher DRH-P400S; 400 W maximum power; 24 kHz maximum frequency) for a period between 30 and 60 min at 60% amplitude and 0.5 cycle ratio. In a typical experiment, around 200 mg of oxidized nanotubes were dispersed in 50 mL of Pluronic solution. The resulting suspension was centrifuged at 13000 rpm in a Hermle LaborTechnik, Z383 device and the supernatant liquid was decanted off. This supernatant was filtered through a 3 μm pore size polycarbonate filter using a vacuum-filtration equipment, Figure 2.3a). The obtained solid

material after filtration consists of a heterogeneous mixture of purified single-walled carbon nanotubes wrapped by Pluronic block copolymer [75], Figure 2.3b).

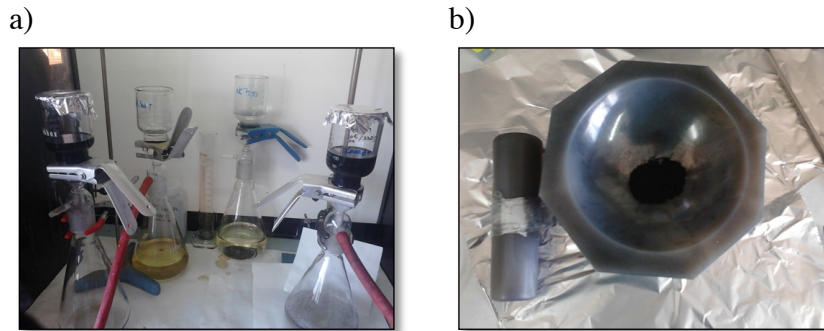


Figure 2.3: a) Purification treatment of the nanotubes filtered with a Teflon membrane and washed with DMF and methanol, b) single-walled carbon nanotubes wrapped by Pluronic block copolymer.

CNT purity was controlled by absorption spectroscopy measurements in the near infra-red (NIR) region on the decanted supernatant. The absorption spectrum in this region was used to calculate the so-called purity index, as proposed by Itkis et al. [76]. The purity index was as high as 0.195, in contrast to 0.037 calculated for the as-grown nanotubes measured after suspension in 1wt.% SDBS surfactant solution. These data show the effectiveness of the purification treatment in terms of the removal of carbonaceous impurities. The purification treatment employed here serves also to remove graphitic and metallic impurities [75, 77].

The neat epoxy matrix was prepared by directly mixing TGAP and DDS in stoichiometric ratio and stirring magnetically at 60 °C for a period of time no longer than 30 minutes to avoid pre-curing reaction. The epoxy/CNT nanocomposites were prepared by a previous stage of premixing. This was carried out by solvent-free mixing of CNT powder in TGAP (60 °C, magnetic stirring for 45 minutes, followed by 15 minutes of tip sonication) and then DDS was incorporated into the TGAP/CNT blends and mixed as mentioned earlier. Epoxy and nanocomposite samples were cured in a Perkin Elmer hydraulic press coupled to a Greaseby Specac heating plates. The curing conditions were set as 30 min at 200 °C under 3 tones of pressure. Samples were hot-pressed in steel dish moulds covered with Teflon lids. Then the cured samples were transferred to an oven and post-cured at atmospheric pressure for 4 hours at 200 °C. Test samples, shaped as cuboid specimen bars with dimensions 70×12×2 mm³, were manufactured by this method.

2.1.1.3.2. SWCNT/PVDF composite preparation by hot-pressing

Poly(vinylidene fluoride), PVDF, was purchased from Aldrich ($M_w \sim 534000$, as obtained by gas phase chromatography). The appropriate amount of the CNT sample was mixed with 15-20 mL of acetone and immersed in the ultrasounds bath. Acetone is not a good solvent for PVDF, but is finely disaggregated in stirred acetone dispersions [78]. Additionally, SWCNT samples can be relatively well dispersed in acetone and therefore a good dispersion of the SWCNT in the polymer matrix is achieved by preparing the SWCNT/PVDF mixtures by sonication/stirring in acetone. In a typical experiment, an appropriate amount of the SWCNT sample was mixed with 15-20 mL of acetone and immersed in the ultrasounds bath. The total mass of PVDF and CNT sample was approximately 11 g. Separately, PVDF was manually dispersed in acetone and then added to the SWCNT/acetone dispersion in an ultrasound bath. A mechanical stirrer was inserted into the acetone dispersion. Sonication and mechanical stirring were applied until the acetone was completely evaporated. The resulting material was cut into small pellets and pressed at 2 Tons and 200 °C for 1 h, Figure 2.4. The material was allowed to cool down inside a mould. The nonpolar α -phase was obtained by crystallization from the melt. Homogeneous discs, with diameters of 130 mm, thicknesses of 1 mm and CNT filler contents between 0-10 wt.% were then obtained for SWCNT and MWCNT, functionalized and non-functionalized composites, which will be referred as followed in the rest of the manuscript: SWCNT and SWCNT - Func and MWCNT and MWCNT – Func, respectively.

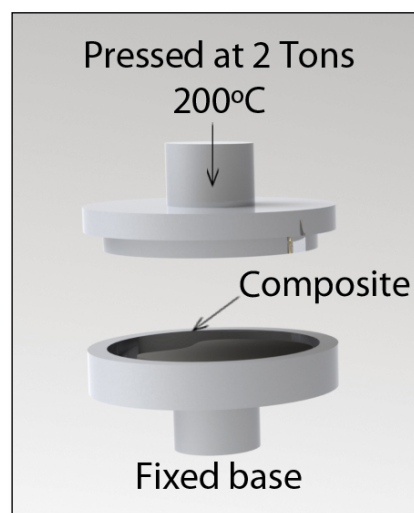


Figure 2.4: Hot-pressing system.

2.1.1.3.3. CNT/PVDF composites preparation by spray-coating

Single-walled carbon nanotubes (SWCNT, AP-SWNT grade) and Poly(vinylidene fluoride), PVDF, with thicknesses between 15 and 20 μm were produced by mixing different amounts of CNT (0-5 wt.%) with 20 mL of N,N-dimethylformamide (DMF, Merck 99.5%). The solutions were placed in an ultrasound bath for 6 h in order to optimize CNT dispersion. After this step, 2 g of PVDF were added to the initial solution and placed in a magnetic stirrer for complete dissolution of the polymer and to avoid CNT aggregates. Flexible films were obtained by spray-coating, Figure 2.5, using a commercial airbrush (Airbrush Kit - Ventus), at a distance of 10 cm using an airbrush pressure of 3 psi. Solvent evaporation and consequent crystallization was performed inside an oven at controlled temperature of 30°C.

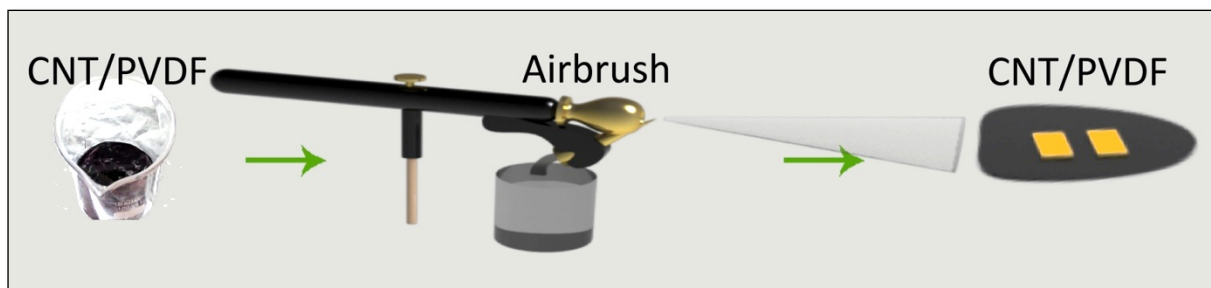


Figure 2.5: Spray-coating system.

2.1.2. Sample characterization

2.1.2.1. Morphology and CNT dispersion

Scanning electron microscopy (SEM) experiments were performed in a Hitachi S3400N set-up working in the secondary electrons mode at a voltage of 15 kV and a distance of 5 mm. Cured samples were fractured and the edge was sputtered with a 10 nm gold layer prior to their observation.

Transmission electron microscopy (TEM) images were taken with a JEOL-2000 FXII microscope working at 200 kV and with 0.28 nm point-to-point resolution. Cured samples were cut using a microtome and deposited on a copper grid for their further use.

Atomic Force Microscopy (AFM) measurements were performed with a Multimode SPM from Veeco Instruments (Santa Barbara, US) equipped with Nanoscope V controller and JV-scanner (10 μm scan size in XY, and 2.5 μm Z-range). Electrical mapping was carried out using cantilevers SCM-PIC made of Sb-doped W with 0.01-0.025 $\Omega\cdot\text{cm}$

resistivity coated with 20 nm of Pt/Ir and 3 nm Cr. Cured composites were cut with an ultramicrotome, thoroughly polished and attached to a steel sample holder with silver painting prior to the AFM measurements.

2.1.2.2. Thermal properties and degree of crystallinity

Differential scanning calorimetry (DSC) was performed in a Mettler DSC-823e calorimeter, calibrated with an indium standard (heat flow calibration) and an indium-lead-zinc standard (temperature calibration). Dynamic heating and cooling at 10 °C/min was performed to approximately 10 mg of sample in standard 40 µL aluminium crucibles, under a 100 mL/min flow of N₂. X-ray diffraction (XRD) measurements were performed at room temperature in a Bruker AXS D8 Advance diffractometer using CuKα radiation.

2.1.2.3. Electrical and electromechanical properties

The electrical resistivity of the samples was measured by the 2-wire method, where the voltage was applied and the current measured by a Keithley 487 picoammeter/voltage source. All measurements were performed in direct current (DC) mode, at room temperature. On each sample, two parallel rectangular gold electrodes were deposited by magnetron sputtering on one side of the sample. Copper wires were attached to the electrodes with silver paint to ensure good electrical contact. The sheet resistivity $\rho(\Omega.sq)$ was calculated by:

$$\rho = R \frac{D}{L} \quad (2.1)$$

where R is the surface resistance, D is the length of the electrode (6 mm) and L is the distance between the electrodes (1 mm). The electrical conductivity is given by the inverse of the electrical resistivity $1/\rho$.

The piezoresistive experiments were performed in a 4-point-bending configuration (Figure 2.6) using a Shimadzu-AG-IS universal testing machine. Consisted in 4 loading and unloading cycles at a velocity of deformation of 2 mm min⁻¹ and 1 mm in z-displacement.

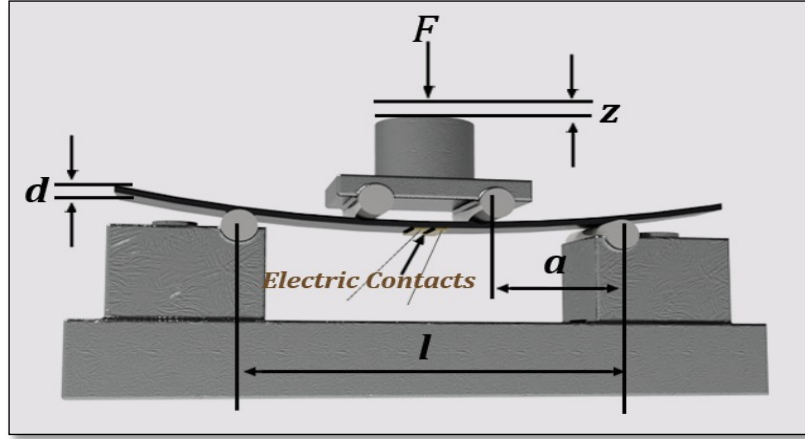


Figure 2.6: Schematic representation of the 4-point bending tests: z is the vertical displacement of the piston, d is the thickness of the sample (~ 1 mm) and a is the distance between the first and the second bending points (15 mm) and l the distance between the lower supports (45 mm).

The main parameter to be taken into account in strain sensing applications is the sensitivity to strain, expressed quantitatively as the gauge factor (GF). The GF is defined as the ratio of fractional change in electrical resistance to the fractional change in length (strain) [79]:

$$GF = \frac{dR/R}{dl/l}, \quad (2.2)$$

in equation 2.2, R is the steady-state material electrical resistance before deformation and dR is the resistance change caused by the variation in length dl [79]. The quantity l represents the length of the sample. The resistance change under strain results from the contribution of the dimensional change – geometrical effect DR_D – and from the intrinsic piezoresistive effect DR_I . For the surface mode measurements the GF can be written as [79]:

$$GF = \frac{dR/R}{\varepsilon_l} = \Delta R_D + \Delta R_I = (1 + \nu) + \frac{d\rho/\rho}{\varepsilon_l} \quad (2.3)$$

where, $\varepsilon_l = dl/l$, ν is the Poisson ratio and ρ is the electrical resistivity.

The strain on the sample was calculated from the theory of a pure bending of a plate to a cylindrical surface, which is valid between the inner loading points. In this region, the radius of curvature, r , is constant and given by [17]:

$$r = \frac{3al - 4a^2}{6z}, \quad (2.4)$$

and the strain of the composite along the longitudinal direction is:

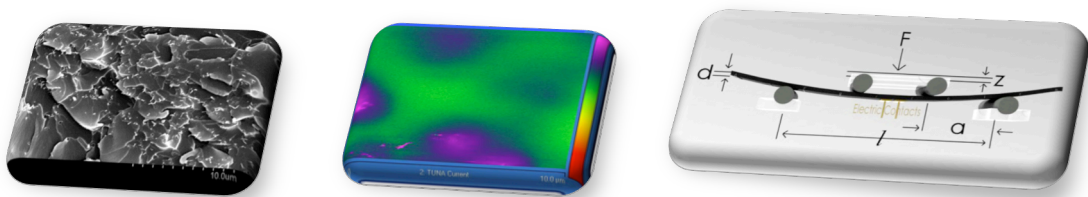
$$\varepsilon = \frac{3dz}{3al - 4a^2}, \quad (2.5)$$

where d is the substrate thickness, z is the displacement of the inner loading bar, a the distance between first and second points of the 4-point bending system, and l is the length of the sample (distance between the lower supports). For the measurement of the GF of the material, $a = 15$ mm and $l = 3a$ and thus equation (2.5) yields:

$$\varepsilon = \frac{3dz}{5a^2}. \quad (2.6)$$

Electromechanical tests with samples of the different composites around the percolation threshold concentration were performed. Each test consisted in up/down cycles of z -displacement. The GF was calculated for each cycle using equation (2.2) from the z -displacement and the simultaneous electrical resistance variations by taking the best fit by linear regression. Finally, the GF average value was calculated from four different measurements for each sample. The calculated values of the GF for the up and down mechanical cycles was the same, unless otherwise stated.

The measurement of the surface resistance change ($\Delta R/R$) in each mechanical experiment was obtained from the measurement of the electrical resistance, with an Agilent 34401A digital multimeter. For this purpose, two parallel rectangular gold electrodes of 6 mm width and 1 mm distance between them were vacuum evaporated onto one of the sides the samples, and a copper wire was attached to the electrodes with silver paste.



3. Transducers based on CNT/EPOXY composites

This chapter reports on the physical characteristics and piezoresistive behaviour of polymer based nanocomposites, composed of EPOXY and carbon nanotubes (CNT). This chapter is based on the following publication:

Gonzalez-Dominguez JM, Anson-Casaos A, Martinez MT, Ferreira A, Vaz F, Lanceros-Mendez S. Piezoresistive response of Pluronic-wrapped single-wall carbon nanotube-epoxy composites. *Journal of Intelligent Material Systems and Structures*. 2012.

This chapter focus on the physical characteristics and piezoresistive behaviour of polymer-based nanocomposites, composed of epoxy resins and Pluronic-wrapped carbon nanotubes (CNT). The samples were prepared with CNT concentrations up to 1 wt.%. Good CNT dispersion was achieved due to the Pluronic wrapping of the CNT, as confirmed by electron and atomic force microscopies. The correlation between the electrical resistivity and mechanical solicitations was obtained for varying mechanical solicitations. The electrical response is linear over a wide strain range and the values of the gauge factor are ~ 2.6 . The stability of the signal over 32 cycles, the time response to deformations from 0.1 to 50 mm min^{-1} and the stable temperature behaviour up to 60 °C shows the viability of these materials to be used as piezoresistive sensors.

3.1. Results and discussion

3.1.1. Composites structural characterization

The nanotube dispersion within the epoxy nanocomposites was studied by electron microscopy techniques, including SEM and TEM (Figure 3.1).

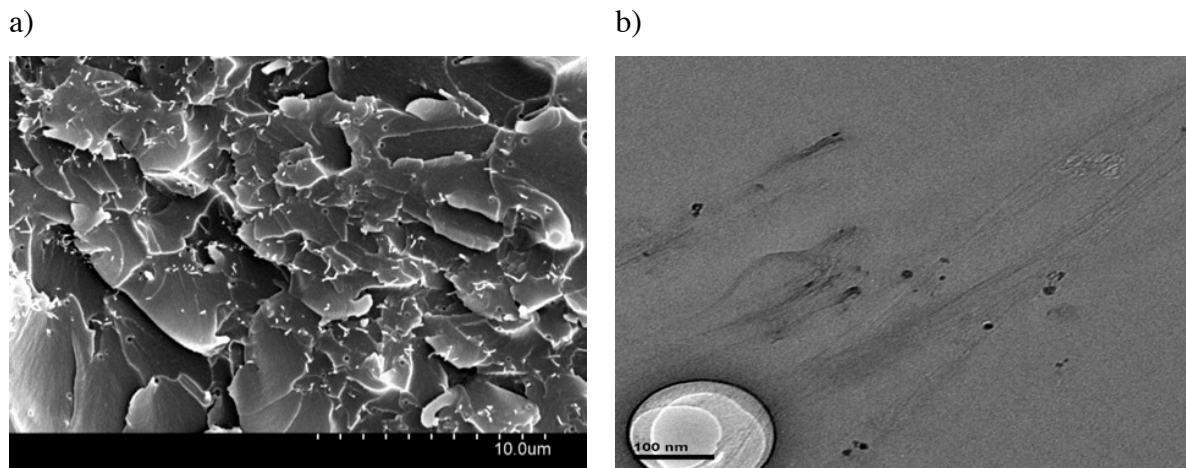


Figure 3.1: Electron microscopy images of epoxy/CNT nanocomposites; a) fracture edge SEM image of nanocomposite containing 0.5 wt.% CNTs, and b) TEM image of nanocomposite at 0.1 wt.% CNT.

The fracture surface of the nanocomposites, as visualized by SEM (Figure 3.1a)) show CNT bundles randomly dispersed across the epoxy matrix. The distribution is highly homogeneous due to the effect of the Pluronic block copolymer wrapping, which is suitable for improving the dispersion of the nanotubes, especially those undergoing oxidative

treatments, which are hard to disperse in epoxy polymers [80]. From SEM observations, the thickness of bundles is largely reduced by the Pluronic wrapping and the nanotubes present better adhesion to the matrix, since bundles look highly damaged rather than pulled out, as previously stated [80]. Good dispersion and adhesion to the matrix is further confirmed by TEM (Figure 3.1b)) where thin CNT bundles can be observed. The presence of Pluronic causes the appearance of vesicular structures upon self-assembling, which are visible in both electron microscopies.

Figure 3.2 shows comparative AFM images ($10 \times 10 \mu\text{m}^2$) of the epoxy nanocomposite with 0.1 wt.% Pluronic wrapped CNT. Figures 3.2a) and 3.2b) show the topography image and its associated current map. In the current map it is possible to observe areas of higher conductivity corresponding to bundles of CNT surrounded by areas of lower conductivity but higher than the rest of the composite, which seem to indicate the presence of non-disaggregated CNT bundles. In general, these areas are hard to find in the composite containing 0.1 wt.% of CNT since at so low concentration, the bundles are mainly disaggregated. There are some areas (pink colour) in which the bundles are on the surface and present the maximum current and other areas (dark blue) in which the CNT are sunk and are not visible, presenting higher current than the bare matrix (in green). The aforementioned results are in agreement and confirm the conclusion obtained from the SEM and TEM images (Figure 3.1).

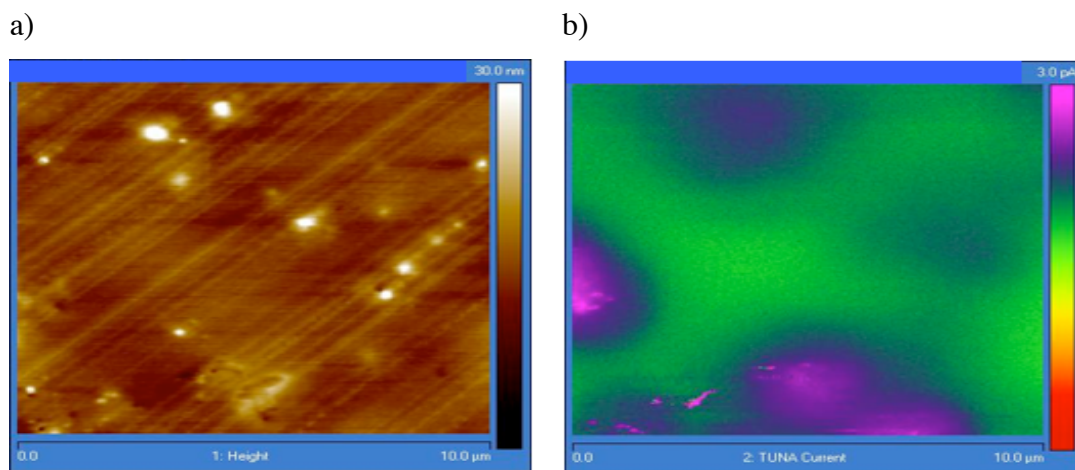


Figure 3.2: AFM images of epoxy/CNT nanocomposites specimen at 0.1 wt% CNT loading, a) topography image, b) current mapping.

In the topography image it is also possible to observe some dots prominent and at the background. Some stripes are also visible, which correspond to the cutting marks and polishing of the microtome.

3.1.2. Electrical Conductivity

Representative I - V curves for epoxy composites with different CNT loadings are shown in Figure 3.3 a). The electrical volume resistivity of the neat epoxy and CNT/epoxy composites is also represented in Figure 3.3 b) as a function of CNT concentration. For the neat epoxy, the resistivity is below to 10^{11} Ω .cm, the values of resistivity increasing with the CNT loading. In this way, the 0.1, 0.5 and 1 wt.% CNT composites exhibit values of $\sim 3.7 \times 10^7$, 5.2×10^5 and 1.3×10^4 Ω .cm, respectively. These values are similar to those reported in CNF/epoxy composites for 0.5 and 1 wt.%, showing on the other hand, a lower value of volume resistivity for the case of 0.1 wt.% (6.1×10^{11} Ω .cm) [81].

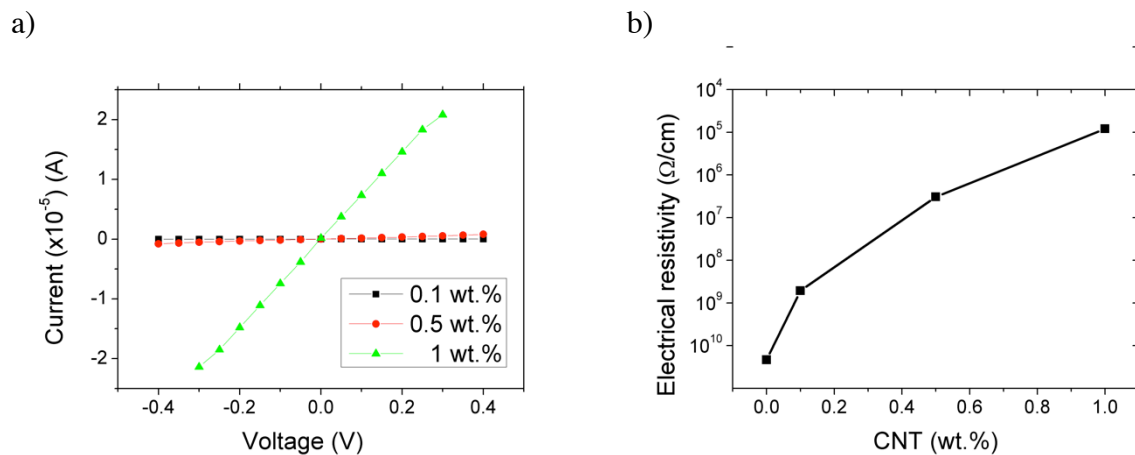


Figure 3.3: Resistance measures from slope of I - V curves (a). Electrical volume resistivity values vs volume fraction of CNT (b).

Though the variation of the electrical properties with concentration for carbon nanoparticle/polymer composites is usually understood in the framework of percolation theory [41], recent studies in epoxy composite systems point out that the main conduction mechanism is related with emergence of a weak disorder regime [81] related to a tunnelling mechanism. Further, the percolation at low filler concentrations is even better understood in the scope of the complex network theory by the formation of a capacitor network [38].

It should be noted that the current-voltage I - V curves of the investigated nanocomposites show a good linear relationship, Figure 3.3, which confirms an Ohmic behaviour for all loadings. Although previous studies showed that current-voltage behaviour gives an indication of the mechanisms of conductivity, i.e. linear I - V relationships as indicators of direct contact between fillers and power law I - V curves indicating tunnelling mechanisms [82-84], there is not a definitive conclusion about these two behaviours. In the

present case, the low concentrations at which the percolation is found, the linear behaviour of the I-V curves and the fact that the CNT are wrapped with Pluronic, support the theory of the formation of the capacitor network [38] to explain the electrical behaviour of the composites.

3.1.3. Electromechanical response

The GF for the conductive samples was calculated from 4 total cycles in 4-point bending tests at 2 mm min^{-1} and up to 1 mm in z -displacement. An example of the experimental curves, which are the result of the four upward parts for the four cycles of 4-point bending tests, are shown in Figure 3.4 for composite at $0.5 \text{ wt.}\%$.

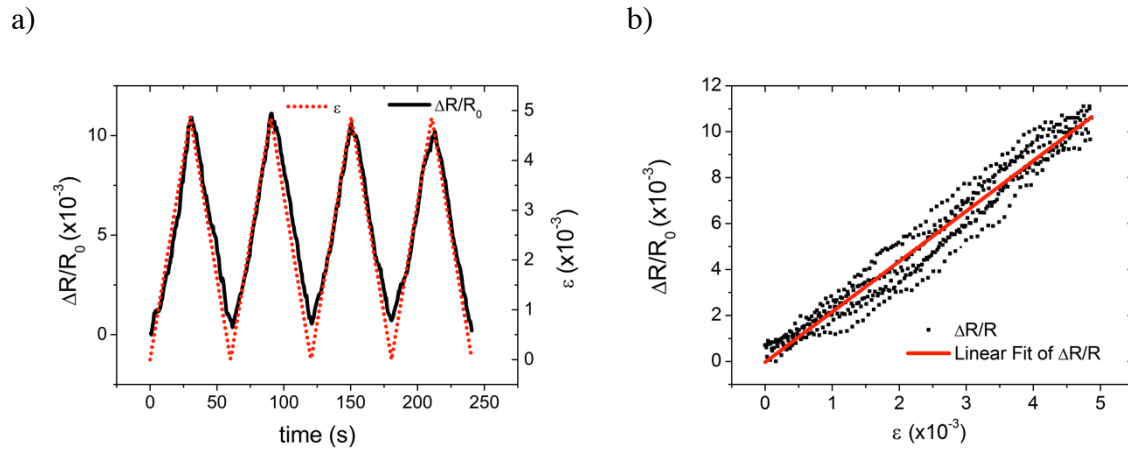


Figure 3.4: Strain applied to a sample and the corresponding resistance variation with time (a), and relative change in electrical resistance due to mechanical deformation, for four up-down cycles applied to a sample with $0.5 \text{ wt.}\%$ CNTs, z -deformation of 1 mm , deformation velocity of 2 mm/min at room temperature. The R-square of the fit is 0.96 (b).

With the aim of ensuring that the composite deformations are in the elastic mechanical region, the resistance was measured at displacements between 0 and 1 mm . In spite of the fact that the piezoresistivity of conducting particle-reinforced insulating matrix has been previously studied, there are not still definitive conclusions about this subject. In general, it is assumed an exponential dependence of the resistance change vs strain as a consequence of interparticle tunneling model [85]. This exponential behaviour converts to linear for small strains, such as the case shown in this study, so the GF can be calculated with a linear function (Figure 3.4 b)) for which R^2 values of about 0.96 in the linear regression were obtained.

In our experiments, the obtained GF was ~ 2.6 for the $0.1 \text{ wt.}\%$ CNT loaded sample, similar to the values obtained for the composites with 0.5 and $1 \text{ wt.}\%$ CNT content. It is

important to notice that in the present study the electromechanical sensitivity, as indicated by the GF , is practically the same for the three loadings, in contrast to previous reports showing that the sensitivity is higher in the surroundings of percolation thresholds [39, 46, 48]. The good dispersion achieved by the Pluronic wrapping and the variations in the conduction mechanism within the CNT network by the wrapping itself lead to a constant variation of the resistivity for a given load, independently of the initial resistance. As the matrix epoxy exhibits a Poisson's ratio of 0.38 [86], the geometric term in Equation (2.3) becomes $1+2\nu=1.76$. Consequently, the higher GF values observed for the piezoresistance effect can be attributed to the intrinsic change in resistance, caused by variations in the CNT network.

3.1.3.1. Dependence of the GF with the number of cycles

A cyclic loading experiment subjected to a 32 cyclic 4-point-bending tests and the corresponding electrical response for the composite at 0.1 wt.% is shown in Figure 3.5. Overall, it is possible to observe a trend to increase the $R_{z=0}$ (resistance response for $z = 0$ mm) and $R_{z=1}$ (resistance response for $z = 1$ mm) with increasing number of cycles.

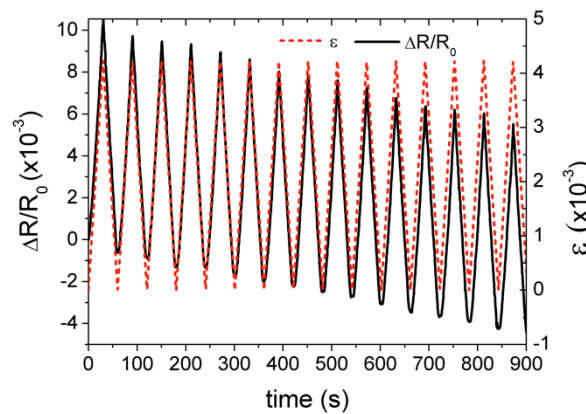


Figure 3.5: Sensing resistance of the sample at 0.1 wt.% as a function of time, during a four-point bending experiment consisting of 32 cycles at 1 mm in z -displacement. Only the first 15 cycles are shown.

The increase of the resistance for increasing number of cycles points out to fatigue effects indicative of irreversible variations in the filler network responsible for the conductivity of the composites. This fact is confirmed by the decreases of the GF with increasing the number of cycles (Figure 3.7a) for the first cycles, showing a trend to stabilization after that.

3.1.3.2. Dependence of the GF with increasing transversal deformation

Figure 3.7b) shows the strain sensing performance of the composite at 0.1 wt.% filler loading as a function of z -displacement in mm. Here, the GF was calculated when the films were subject to cyclic 4-point-bending tests with deformations in the interval 0.1 to 1 mm in z -displacement. The plot shows a maximum GF of 2.6 for 1 mm bending deformation followed by a linear decrease for increasing bending deformations. This behaviour implies that the sensitivity is not constant, but depends on the applied strain, as reported in [48] and also in agreement with studies focused in carbon-black polymer systems [87-89].

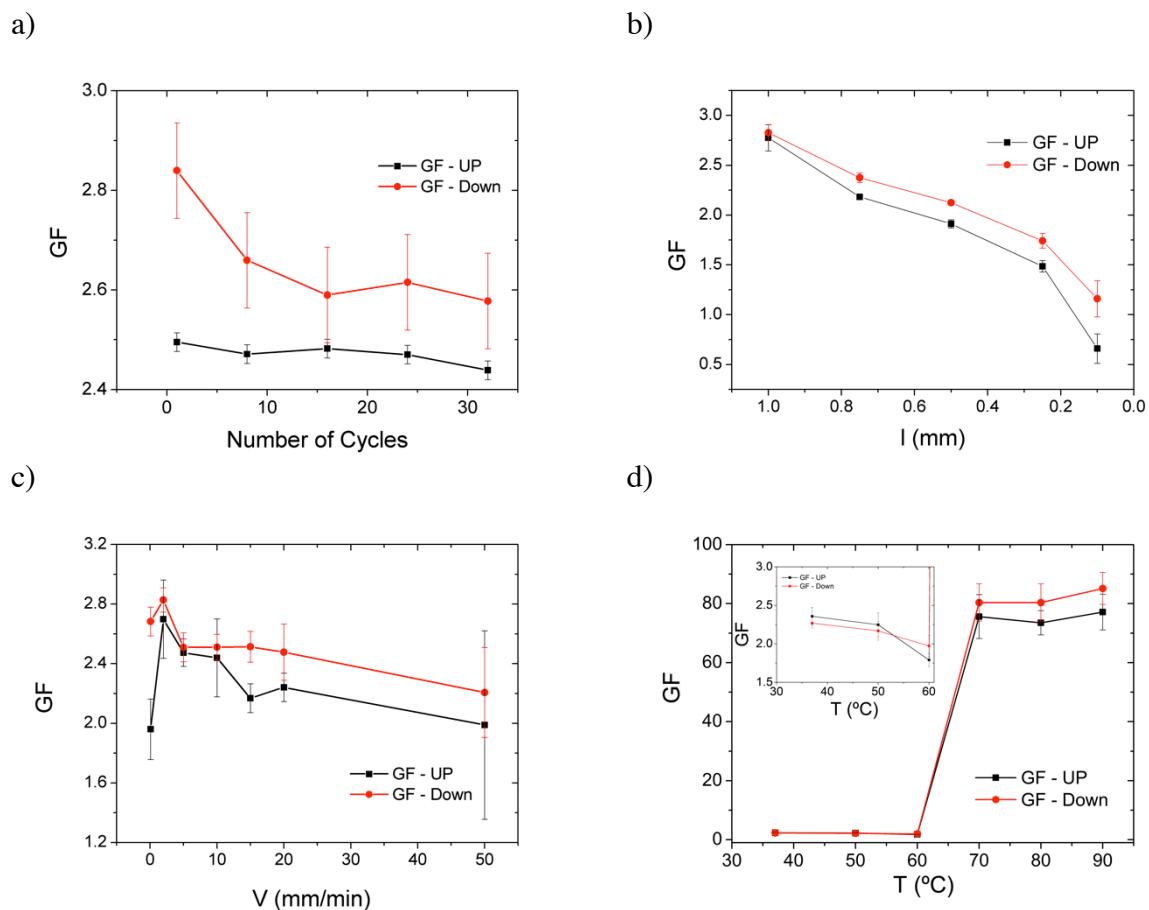


Figure 3.6: GF as a function of the number of cycles (a), z -displacement (b), deformation velocity (c) and temperature (d).

3.1.3.3. Dependence of the GF with increasing deformation rate

The response for the composite at 0.1 wt.% was also tested by applying the same deformation (1 mm z -displacement) at different velocities. Figure 3.7c) shows that the GF is

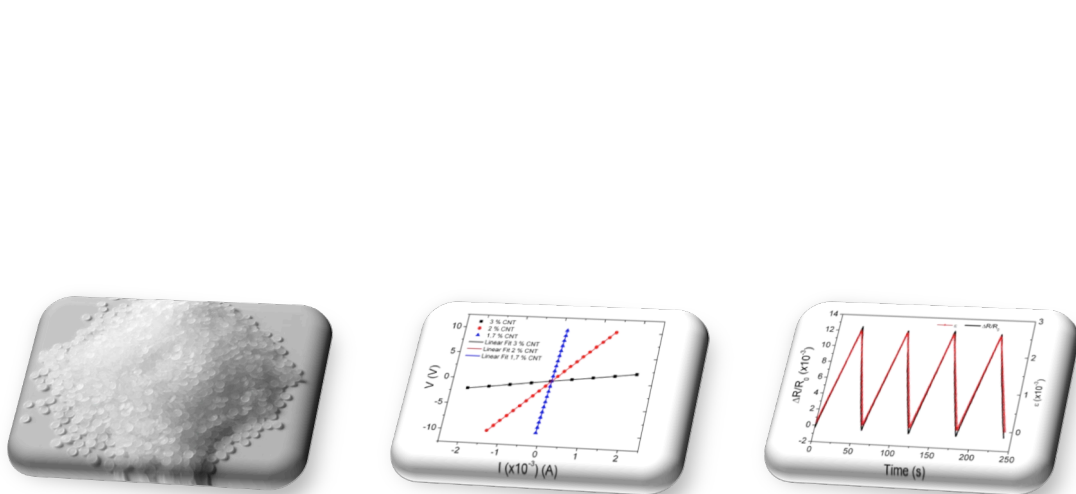
practically the same for the velocities of 5 to 20 mm min⁻¹. For the deformation speeds under consideration, the response time of the composite is both mechanically and electrically stable.

3.1.3.4. Dependence of the GF with increasing temperature

Finally, the temperature response of the material was evaluated by applying a given deformation of 1 mm in z direction at a rate of 2 mm min⁻¹. It was observed that the *GF* is practically constant up to 60 °C, increasing strongly for temperatures above. This strong increase of the *GF* is related to the glass transition temperature, *T_g*, of the polymer [90-92]. At *T_g* the polymer undergoes a transition from a glassy state to a rubbery state, becoming mechanically softer and therefore allowing larger reconfigurations of the CNT network for a given deformation. This therefore leads to larger values of the *GF* (Figure 3.7d), which are 9 to 10 times larger than the ones at temperatures below the *T_g*.

3.1.4. Conclusion

Pluronic wrapping of the CNT allows a good dispersion of the filler, avoiding large aggregates that could hinder electrical and mechanical performance. The electrical response is characterized by linear I-V curves and a percolation threshold around 0.1 wt.% loading. The piezoresistive response, quantitatively analyzed by the gauge factor, is independent of the concentration, once the threshold is achieved meaning that mechanical deformation of the composites induces similar strong and reversible variations in the CNT network and therefore in the electrical response. The maximum value of the gauge factor is ~2.6, the linearity of the response over a wide strain range, the small variations of the *GF* with the number of cycles and the temperature stability up to 60 °C shows the viability of these materials to be used as piezoresistive sensors.



4. Transducers based on CNT/PVDF composites

This chapter reports on the physical characteristics and piezoresistive response of polymer based nanocomposites, composed of poly(vinylidene fluoride) – PVDF and carbon nanotubes (CNTs). This chapter is based on the following publications:

Ferreira A, Rocha JG, Ansón-Casaos A, Martínez MT, Vaz F, Lanceros-Mendez S. Electromechanical performance of poly(vinylidene fluoride)/carbon nanotube composites for strain sensor applications. *Sensors and Actuators A: Physical*. 2012.

Ferreira A, Martínez MT, Ansón-Casaos A, Gómez-Pineda LE, Vaz F, Lanceros-Mendez S. Relationship between electromechanical response and percolation threshold in carbon nanotube/poly(vinylidene fluoride) composites. *Carbon*. 2013.

This chapter focuses on the physical properties and piezoresistive response of polymer based nanocomposites, composed of poly(vinylidene fluoride) – PVDF and carbon nanotubes (CNT). The samples were prepared by hot pressing with CNT fillers without and with functionalization, via in situ-generated diazonium compounds, and concentrations up to 10 wt.% filler content. The phase present in the polymer was the α -phase. The correlation between the electrical resistivity and mechanical solicitations is presented in this work for the different composites and for varying mechanical solicitations.

The results show that for a CNT concentration close to the percolation threshold, tunneling is the main mechanism responsible for the electrical response, leading also to a significant increase of the electromechanical response of the composites. Interestingly, this fact is independent of the CNT type or functionalization, as well as of the percolation threshold concentration. The values of the gauge factor, ranging up to 6.2, and the linearity of the response over a wide strain range shows the viability of these materials to be used as piezoresistive sensors. The stability of the signal, the time response and the temperature behaviour were also evaluated. The observed electrical and electromechanical behaviour are explained in the framework of the percolation theory.

4.1. Results and discussion

4.1.1. Composites structural characterization

Figure 4.1 shows the XRD patterns of the PVDF without SWCNTs and SWCNT (1.7wt.)/PVDF samples. Both diffractograms have almost identical features, including the characteristic patterns of α -PVDF at $2\theta \sim 17.7^\circ$, 18.4° and 19.9° [93].

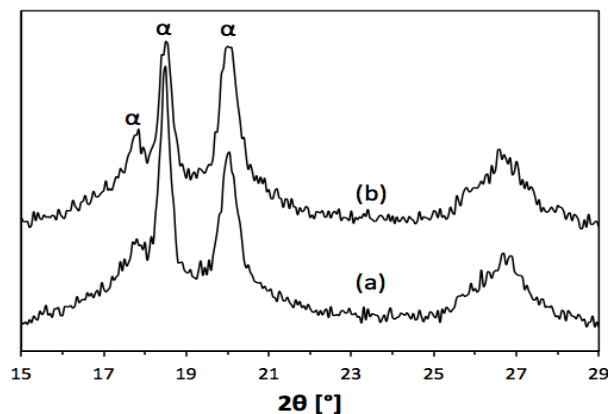


Figure 4.1: XRD patterns of a) PVDF (without SWCNTs) and b) the SWCNT(1.7%)/PVDF sample.

The presence of SWCNT does not seem to affect the crystalline structure of PVDF. The small differences observed in the intensity of the peaks at 2θ of 17.7° and 18.4° are to be attributed just to textural variations of the polymer due to the SWCNT inclusion.

The degree of crystallinity (ΔX_C) can be estimated from DSC data as:

$$\Delta X_C = \frac{\Delta H_m}{\Delta H_{100}} \quad (4.1)$$

where ΔH_m is the melting enthalpy of the composite, and ΔH_{100} is the melting enthalpy of a 100% crystalline sample of pure PVDF, which is 93.07 J/g for the α -phase PVDF [94].

ΔH_m , as well as the melting temperature, did not substantially change for the SWCNT/PVDF samples. An average value of $\Delta H_m = 13.66 \pm 0.78$ J/g was obtained, corresponding to a degree of crystallinity of 14.7%. The melting temperature was 158.9 ± 0.8 °C. From the cooling DSC scan, an average value of 12.96 ± 0.82 J/g was calculated for the crystallization enthalpy, which is almost identical to ΔH_m calculated from the heating scan. The crystallization temperature from the cooling scan of SWCNT/PVDF composites was 131.7 ± 0.8 °C, which was higher to that obtained for the pure PVDF specimen (119.7 °C). Thus, the SWCNT sample filler provides crystallization centers that increase the crystallization temperature by ~ 12 °C, although does not cause any change in the final crystallization degree.

4.1.2. Electrical Conductivity

Representative I-V plots and for the dependence of the electrical conductivity with CNT concentration for the different CNT/PVDF composites is show in Figure 4.2. In all cases, the electrical conductivity of the composites increases with increasing CNT content (Figure 4.2b). In particular, the composites at ≈ 2 wt.% loading show a sharp increase in conductivity of two orders of magnitude. Existing, however, significant differences between the different samples. SWCNT and MWCNT composites show an overall similar trend with small differences in the percolation threshold and of the maximum conductivity. SWCNT are synthesized using Ni/Y catalyst and contains ~ 30 wt.% metal residue, the presence of metal impurities can contribute to higher resistivity and higher resistance–strain sensitivity at higher deformations [95] but, as observed in Figure 4.2, the presence of metal does not influence the electrical conductivity of the composites as compared to MWCNT filled composites. On the

other hand, chemical covalent functionalization affects the nanotube electronic structure, and thus, the electrical response of the composites in a strongly different way in both types of CNT. In particular, SWCNT are strongly affected by the functionalization and the percolation threshold is shifted from $\sim 2\%$ to $4\text{ wt.}\%$ MWCNT, on the other hand, are almost unaffected by the functionalization, leading to lower variations of the percolation threshold. The formation of real organic layers through the chemical functionalization with heptadecafluorooctyl phenyl groups is not expected. A carbon nanotube surface will be never totally covered through covalent functionalization and large regions of the nanotube surface are available to contact other nanotubes. Further, the effective nanotube diameter is not substantially modified by the chemical functionalization [74]. Previous facts lead to the conclusion that the main effects of functionalization at the level of the CNT is that inner layers of MWCNT are not affected, keeping their original electronic properties, whereas SWCNT electronic properties are strongly modified, confirming results observed in [74].

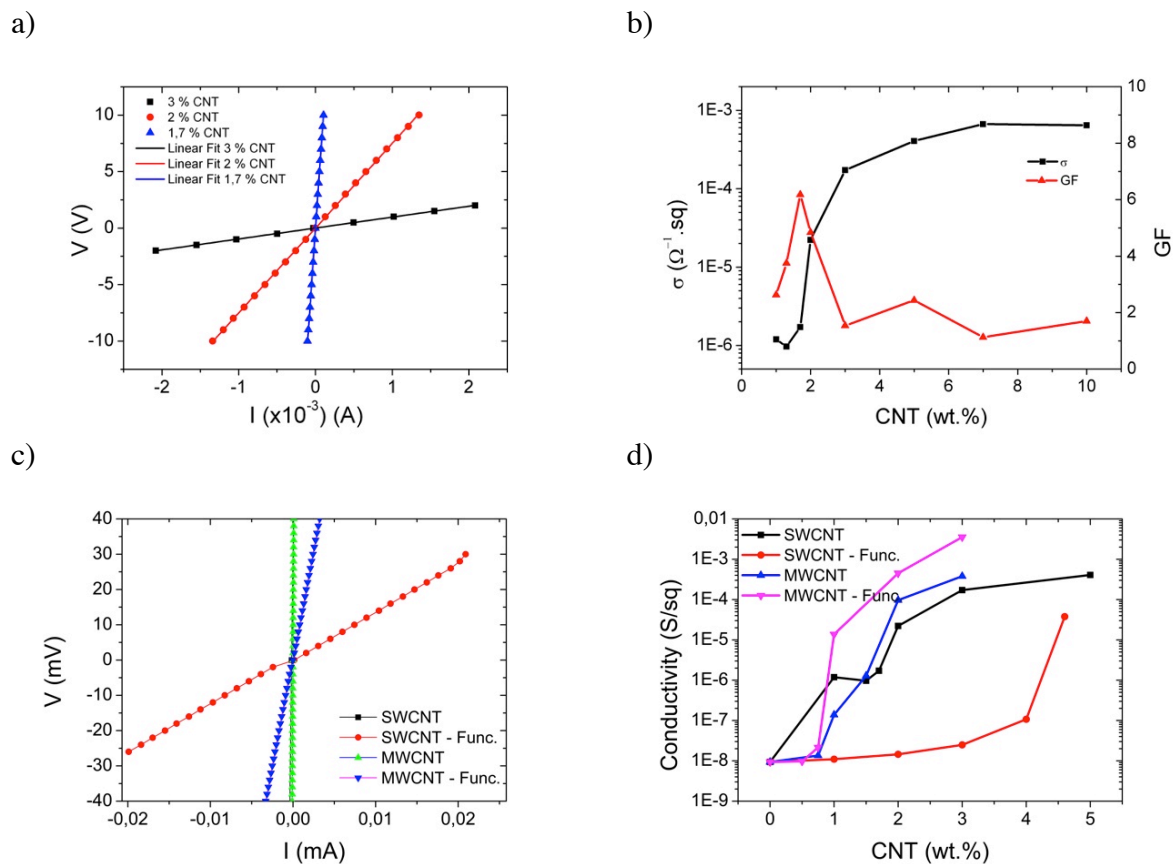


Figure 4.2: a) Typical I-V curves for the different concentrations of PVDF/CNT samples; b) Electrical conductivity and Gauge factor values as a function of the weight fraction of CNT in samples; c) Typical I-V curves for the different concentrations of PVDF/CNT samples SWCNT – 1,5 wt.%, MWCNTs – 0,75 wt.%, SWCNT – Func. – 4,6 wt.%, MWCNT – Func. – 1 wt.%. d) Concentration dependence of the electrical conductivity for the different composites.

The electrical results in these type of composites have been generally discussed in the scope of the percolation theory [82], but mechanism is still far from being understood. Percolation theory shows that at a particular CNT critical volume fraction, the electrical conductivity of the polymer composite strongly increases. It has been pointed out to inter-particle tunneling and the formation of a percolation network as the main mechanism responsible for the observed electrical behaviors as opposed to contact type conductivity [81]. For the composites shown in Figure 4.2 it has been previously discussed based on the network theory [96] that the presence of well-distributed small clusters is more important than a good filler dispersion to achieve higher electrical conductivity. On the other hand, large CNT agglomerations strongly decrease the electrical conductivity for a given CNT concentration. After SEM observation (Figure 4.3), the functionalization affects strongly the dispersion of the CNT within the polymer matrix, and therefore the electrical response, showing larger CNT agglomerates for the functionalized samples, in particular for the SWCNT, where the effect of functionalization is the largest.

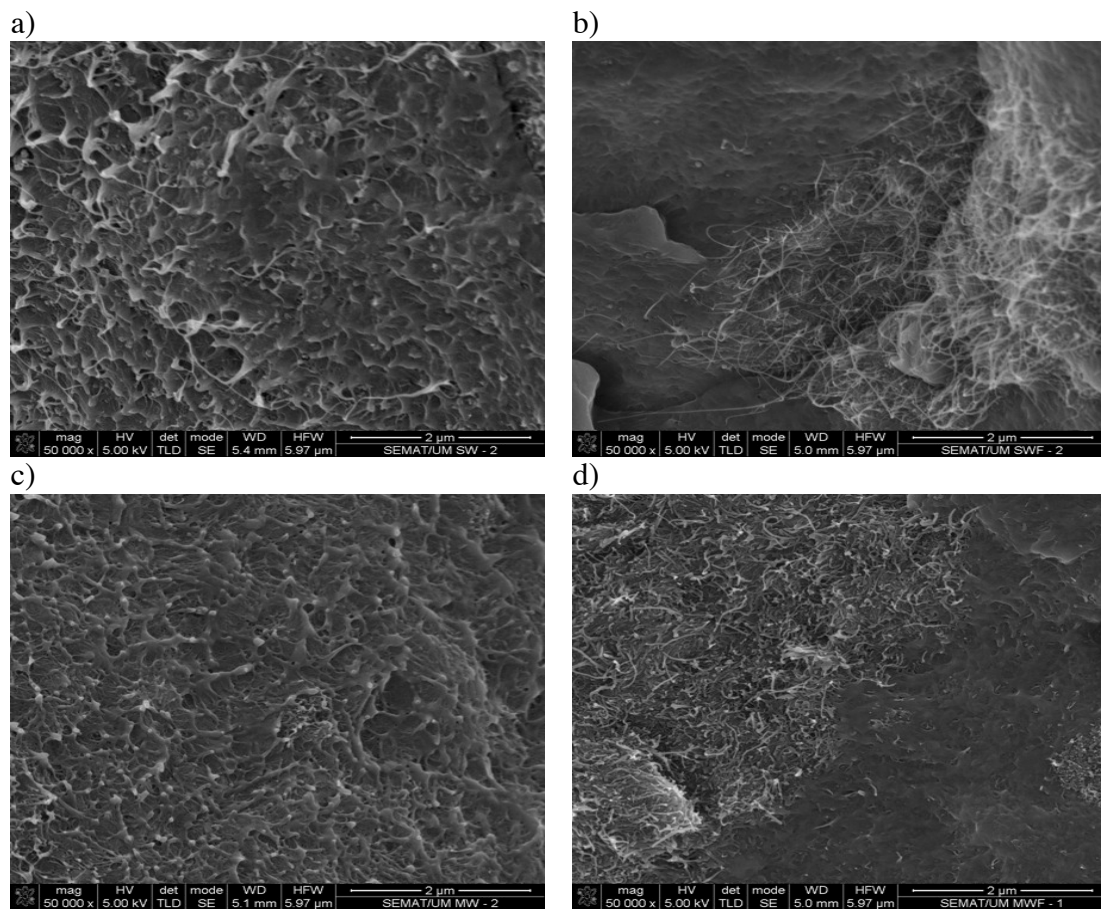


Figure 4.3: SEM images of CNT/PVDF composites at 2 wt.%. a) SWCNT, b) SWCNT - Func, c) MWCNT, d) MWCNT – Func.

Further, the conductivity of the well-distributed clusters cannot be described by the percolation theory, instead, tunneling between nearest fillers explains the observed deviation from the percolation theory. At the percolation threshold concentration, in contrast with the percolation theory that predicts the formation of a contact network [40], conducting inclusions such as the CNT are sufficiently close to each other to be within the tunneling distance to create a conducting network [41-43].

Numerical calculations on the electrical conductivity of CNT/polymer composites, with and without including the tunneling effect show that the inclusion of the tunneling allows increased conductivity of the composite [97]. Also an eventual non-linearity of the I-V curves has been proposed as a way for investigating the origin of the conduction mechanism in CNT/polymer composites [98], but this approach is also inconclusive as composites with tunneling-type conductivity also obey Ohm's law and, therefore, show linear I-V relationships as contact-type conductivity. Finally, different model, such as the ones based on the formation of capacitor networks have been developed to explain low percolation thresholds [38]. In this respect and due to the difficulty of understanding the conductivity mechanism from the conductivity curves, it is interesting to explore the nature of the electromechanical response both, to evaluate the performance of the materials as piezoresistive sensors and to further study the origin of the electrical conductivity as this mechanism will be affected by the mechanical solicitation. Further, overall the results show the possibility of tailoring electrical conductivity of these type of composites as a function of the desired applications. The bulk conductivity is well within the desired range for electrostatic applications [$<10^{-6}$ S cm⁻¹] for all samples in the proximity of thresholds [99].

4.1.3. Electromechanical response

Electromechanical tests were performed in samples with different percentages of CNTs, for different number of bending cycles and different deformation velocities. The linearity of the response with strain and the effect of increasing temperature were also studied.

4.1.3.1. Effect of CNT concentration

Figure 4.4 shows a typical example of the strain tests performed to all samples: several up-down cycles in z -displacement were applied to the sample, and the electrical resistance was measured.

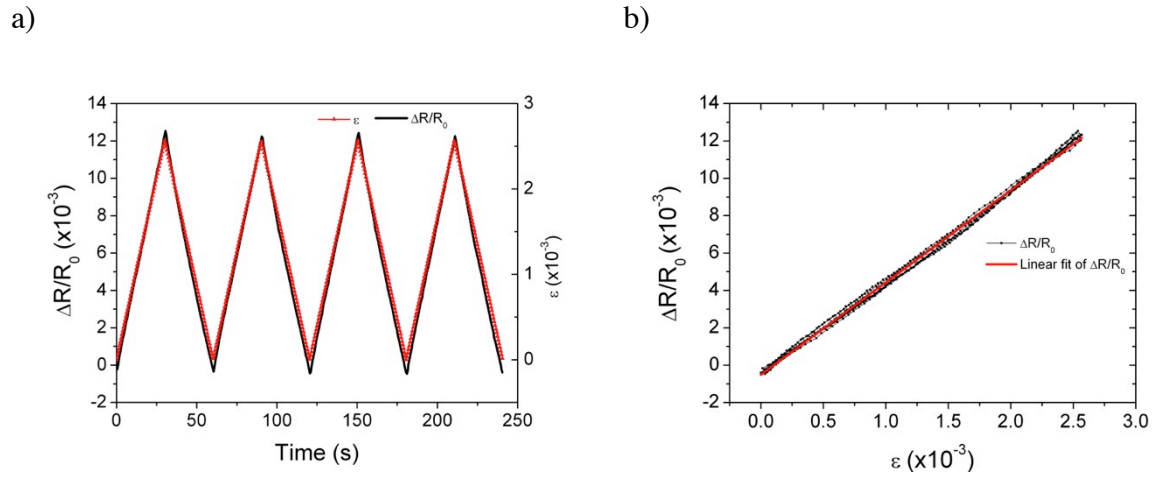


Figure 4.4: a) Strain applied to a sample with 2 wt.% CNT's and the corresponding resistance variation with time, and b) relative change in electrical resistance due to mechanical deformation, for four up-down cycles applied to a sample with 2 wt.% CNTs, z-deformation of 1 mm, deformation velocity of 2 mm/min at room temperature. The R-square of the fit is 0.99.

The GF was then calculated by applying equation 2.2 to the obtained data as presented in Figure 4.4 a), which shows the change in surface resistance during repeated bending cycles, for a sample with 2 wt.% CNT, at room temperature.

The curves were fitted by linear regression. The slope of the linear fit, which corresponds to the GF of the sample, is 4.93, with a R-square of 0.99 (Figure 4.4, b). This result shows that the electrical resistance changes almost linearly with strain and that the linearity is maintained for the different cycles. The same procedure was applied to samples with different CNT wt.% and the GF was obtained for deformations of 1 mm in z direction, at a velocity of 2 mm min^{-1} , at room temperature.

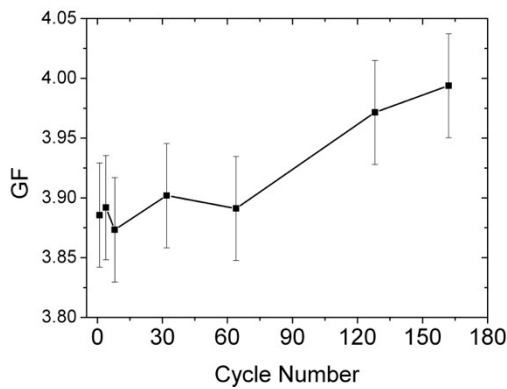
According to the theory of pure bending of a plate to a cylindrical surface, there are two different effects that contribute to the gauge factor: the intrinsic piezoresistive effect and the geometric effect (equation 2.3). For this kind of materials, the Poisson ratio is usually close to 0.38, which means that the geometric effect contribution to GF is around 1.38 [39]. In this way, Figure 4.3 shows that for CNT concentrations above 3 wt.%, the geometric factor is the dominant one, but just below 2 wt.% CNT, the intrinsic contribution to the GF is dominant and the overall GF reaches a value of 6.2. Moreover, it is observed that the region near 2 wt.% CNT at which the conductivity strongly increases, the percolation threshold is the region with the largest GF . This is due to the fact that close to the percolation threshold an applied deformation is able to induce strong and reversible variations in the nanotubes network configuration (e.g. variations of the nanofibre relative distance) [39], which have

strong expression in the variation of the electrical conductivity. Far from the percolation threshold network variations are smaller and therefore their effect in the electrical response. These results are in agreement with the theoretical consideration of the effect of SWCNT concentration on the sensitivity of SWCNT/thermoplastic composites regarding the geometrical and intrinsic effects [100].

4.1.3.2. Stability of the signal and time response

The stability of the piezoresistive response was also analysed for the variation of the gauge factor with the number of bending cycles. The study was carried out for a sample with 2 wt.% CNT, (Figure 4.5).

a)



b)

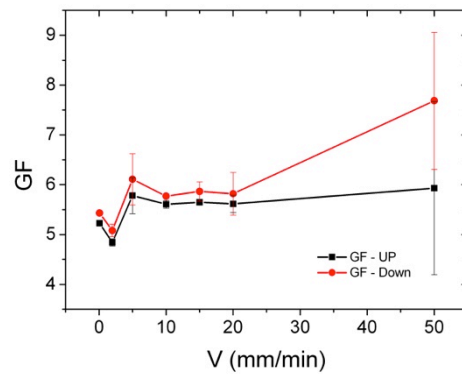


Figure 4.5: Change in GF as a function of the number of bending cycles a) and test velocity b), for a sample with 2 % CNT.

The stability of the signal is demonstrated with small variations, below 3.5% within the measured number of cycles. By testing at different deformation velocities, a stability of the signal for deformation velocities between 0.1 mm min^{-1} and 50 mm min^{-1} , particularly in the up displacement is observed. For lower and higher velocity, some variations are observed related to the mechanical time response of the semicrystalline polymer [101], which, in particular, cannot undergo fast enough recovery at high deformation speeds (e.g. behaviour of *GF*-up in figure 4.5).

4.1.3.3. Temperature behaviour

Applying deformation cycles tested the change of the electromechanical response of the material with temperature. Figure 4.6 shows the behaviour of the electromechanical response of the material at a) room temperature, b) 100 °C and c) 150 °C.

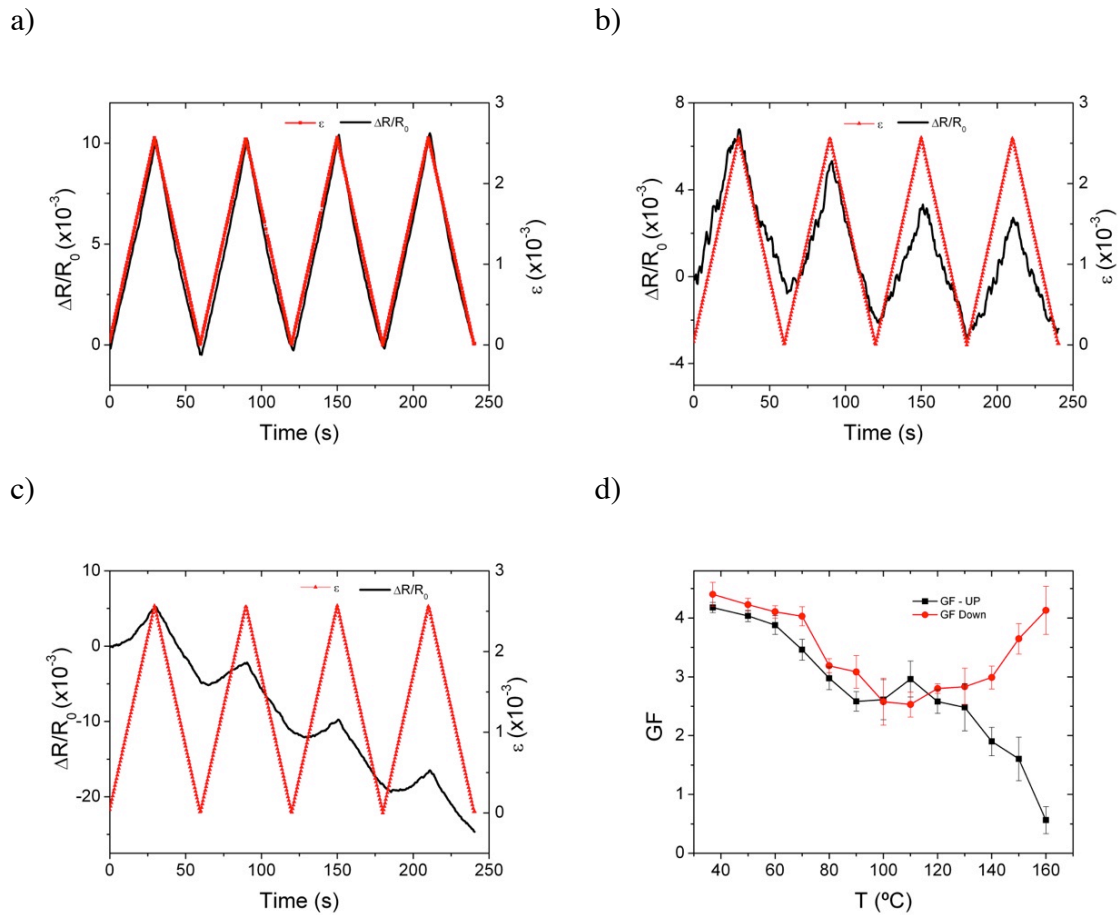


Figure 4.6: Four deformation cycles of 1 mm in z direction; a) room temperature, b) 100 °C, c) 150 °C. d) Gauge factor dependence as a function of temperature for cycles taken at a testing velocity of 2 mm min⁻¹ for a sample with 2% CNTs.

By increasing the temperature, the electromechanical response is steadily reduced up to the temperature around 100 °C. Above this temperature there is a divergence between the loading and unloading cycles, due to strong changes in the mechanical behaviour of the polymer: above the α -relaxation of PVDF, that occurs at $\sim 90^\circ\text{C}$ [101], during the down cycles the material is deformed by the application of the mechanical force but, due to the effect of the mechanical relaxation, by releasing the force, the material does not return to the original position due to plastic deformation, resulting in an imprecise determination of the

GF [88]. In this sense, the temperature of the α -relaxation of PVDF determines the maximum temperature for the material to be used as a reversible and stable sensor.

The decrease of the *GF* with increasing temperature up to ~ 100 °C is consistent with the decrease of the electromechanical coupling. Close to the percolation threshold, increasing deformations results in stronger variations of the fibre network topology, as well as to the effective local concentration, resulting in stronger variations in resistance and therefore of *GF*. By increasing temperature, complex processes occur both related to the conductivity of the polymer matrix, which increases, as well as variations in the mechanical properties of the material, which reduced the local strains to be applied to the CNT network, and therefore the electromechanical coupling. All these factors contribute to a decrease of the *GF*. The theories explaining piezoresistivity in conducting particle-reinforced insulating matrix composites is far from being fully developed. Nevertheless, the main achievements in this field allow explaining the observed behaviour. Theories for the *GF* based on elastic heterogeneity where the conducting phase is stiffer than the insulating one, indicate that the local strains within the latter are enhanced with respect to the averaged macroscopic strains, inducing higher *GF* values [102]. As already expressed, the increase of the temperature decreases local strains and therefore reduces the *GF*. On the other hand, by discussing carbon-black-polymer composites in the framework of percolation networks, based on interparticle tunnelling conduction, it was shown that a logarithmic divergent piezoresistive response exists close to the threshold, as observed in the present study [103].

4.1.3.4. Physical interpretation of the piezoresistive response

It has been shown that the percolation threshold corresponds to the region with the largest *GF* in CNT/polymer composites [52] due to the fact that close to the percolation threshold an applied deformation is able to induce strong and reversible variations (Figure 4.7) in the nanotube network configuration (e.g. variations of the nanotubes relative distance) [39], which has a strong influence in the variation of the electrical conductivity. Far from the percolation threshold, network variations are smaller and therefore their effect in the electrical response is also small [101].

Figure 4.7 shows a typical example of the electromechanical experiments performed with the different samples, where it can be observed the electrical resistance variation to repeated loading-unloading cycles.

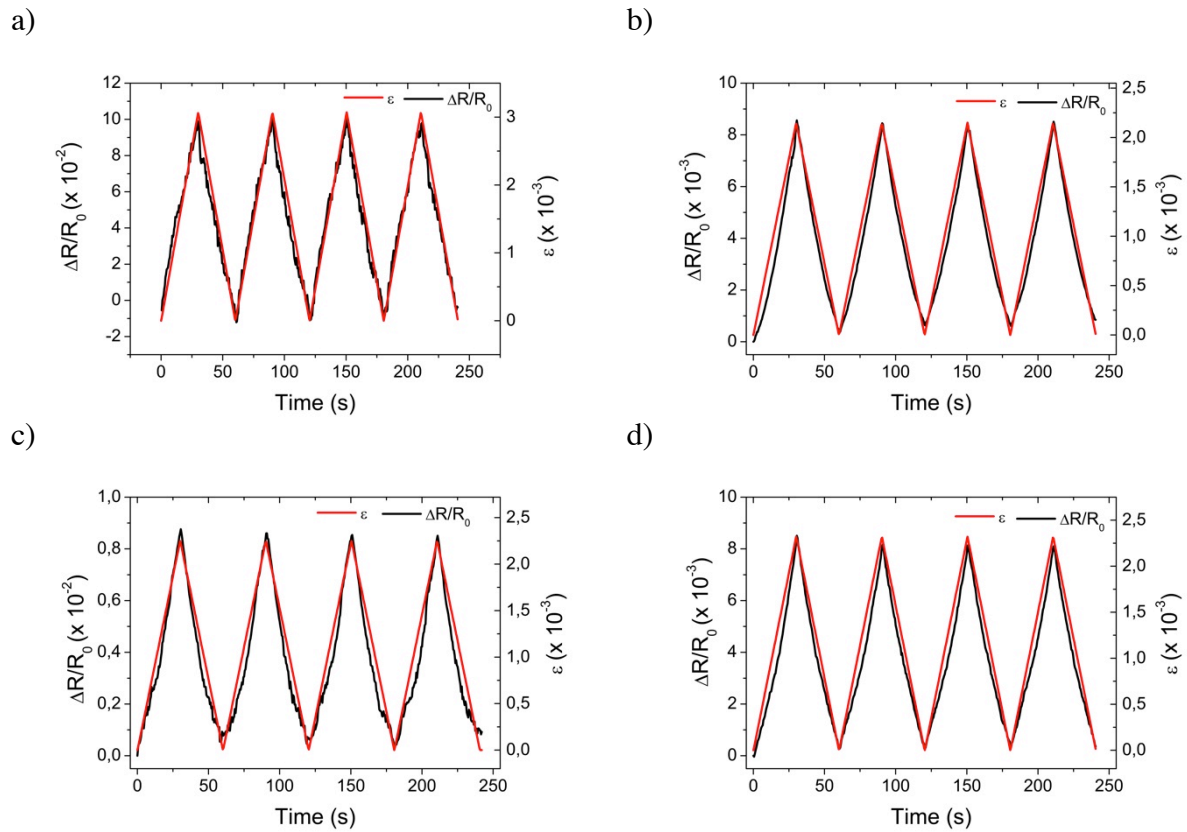


Figure 4.7: Cyclic piezoresistive response as a function of time for a) SWCNT – 1,5 wt.%, b) MWCNT – 0,75 wt.%, c) SWCNT - Func – 4,6 wt.%, d) MWCNT - Func – 1 wt.% for the following conditions: bending of 1 mm, deformation velocity of 2 mm min⁻¹ at room temperature.

Figure 4.7 shows that the electrical resistance changes fairly linearly with the applied strain and that the linearity is maintained for the different cycles and for the different samples. The curves were thus fitted by linear regression as shown in Figure 4.8. The slope of the linear fit with equation 2.3 (obtained with a R-square of 0.99) corresponds to the *GF* of the sample and is presented in Table 4.1. From Solef®PVDF datasheet, the Poisson ratio of PVDF is 0.35 at room temperature, which means that the geometric effect contribution to *GF* is around 1.35. Therefore, the obtained values of the *GF* which are above 3.5 (Table 4.1), show a strong intrinsic contribution of the composite to the *GF*, (equation 2.3).

Table 4-1: GF values resulting of the linear fit of $\Delta R/R_0$ as function of stress.

Samples	wt.%	GF	Standard Error
SWCNT	1,50	3,24	0,04
SWCNT - Func	4,60	3,76	0,07
MWCNT	0,75	3,91	0,06
MWCNT - Func	1,00	3,49	0,06

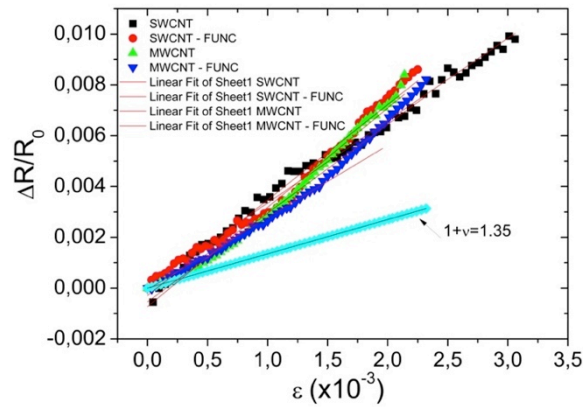


Figure 4.8: Relative resistance variation vs. strain curves and the corresponding fit with equation 2.3 for the determination of the Gauge Factor.

It is to notice in Table 4.1 that, in general, the GF is similar for all samples –being slightly larger for the SWCNT–, independently of the CNT type or functionalization, as well as on the percolation threshold. The piezoresistive response can be discussed in terms of tunnelling, as it is the most consolidated mechanism for the interpretation of the piezoresistive response in this type of materials [85], and it is supported, in our case, by the slight non-linear dependence of the resistance change vs strain [85].

In this scope and according to a heterogeneous fibril model, the general resistance (R) of carbon nanotube composites is determined by the following relationship of tunnelling resistance (R_T) and the CNT gap change-dependent resistance (R_B) [104]:

$$R = \frac{L_T}{A_T} R_T + \frac{L_B}{A_B} R_B \quad (4.2)$$

$$R_T = R_m \left(1 + \exp\left(\frac{E_g}{k_B T}\right) \right) \quad (4.3)$$

$$R_B = R_t \exp\left(\frac{E_a}{k_B T}\right) \quad (4.4)$$

where L_T and A_T are the effective length and effective cross-sectional area of the CNT. R_T represents the intrinsic resistance, R_B the junction resistance, R_m and R_t are proportional constants, E_a is the tunnel activation and E_g is the band gap of CNT, k_B is the Boltzmann constant, and T is temperature [104, 105]. Equation (4.2) can be rewritten as

$$R(T) = R_m \left(1 + \exp\left(\frac{E_g}{k_B T}\right) \right) + R_t \exp\left(\frac{E_a}{k_B T}\right) \quad (4.5)$$

In this approach, the conducting pathways are assumed to be connected in parallel and the resistance of pathways perpendicular to the current are neglected. If conduction is dominated by tunnelling through the polymer gaps separating the CNT and the resistance of the polymer matrix is much higher than the resistance of the particles, R_B , the resistance of the fillers can be neglected, ($R_B \sim 0$) [104]. Thus, assuming that R_m is constant, the resistance change under stress can be expressed by

$$\frac{R(\varepsilon)}{R_0} = \exp(2\alpha d_0 \varepsilon) \quad (4.6)$$

$$\alpha = \frac{2\pi}{h} \sqrt{2m\varphi} \quad (4.7)$$

where $R(\varepsilon)$ and R_0 are the composite resistance under tensile strain (ε) and the original resistance at $\varepsilon = 0$, respectively; d_0 is the tunneling distance between CNT, h is Planck's constant, m is the mass of the charge carriers, and φ is the tunneling barrier height [106]. In this model, if the tunneling distance is responsible for the resistance change under stress, the plot of Eq. 4.6 versus tensile strain (ε) should be linear with a slope of $2\alpha d_0$ (Figure 4.9).

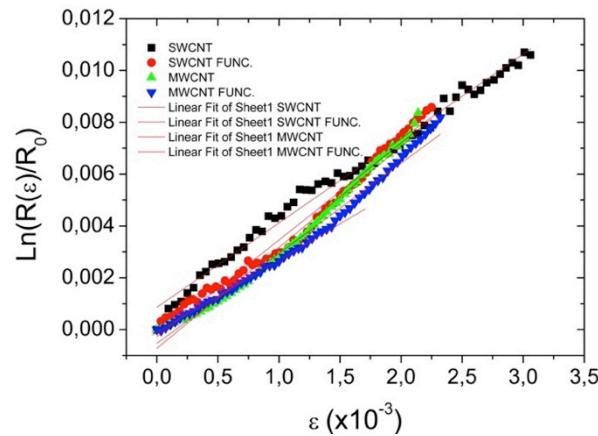


Figure 4.9: Surface sensing resistance change $\text{Ln}(R(\varepsilon)/R_0)$ as function of stress and corresponding fittings with Equation 4.6.

Table 4.2 show the calculated distances between two fillers particles for the different samples using the parameters derived from the fit with Equation 4.6 (Figure 4.9) assuming different barrier heights.

Table 4-2: Distance between two CNT, results of Equation 4.6 as function of stress.

					Tunneling barrier height - ϕ (eV)				
					0,5	0,75	1	2	4
Samples	wt.%	Slope	Standard Error	αd_0	d_0 (nm)	d_0 (nm)	d_0 (nm)	d_0 (nm)	d_0 (nm)
SWCNT	1,5	3,26	0,04	1,63	0,45	0,37	0,32	0,22	0,16
SWCNT - Func	4,6	3,74	0,07	1,87	0,52	0,42	0,37	0,26	0,18
MWCNT	0,75	3,90	0,06	1,95	0,54	0,44	0,38	0,27	0,19
MWCNT - Func	1	3,48	0,06	1,74	0,48	0,39	0,34	0,24	0,17

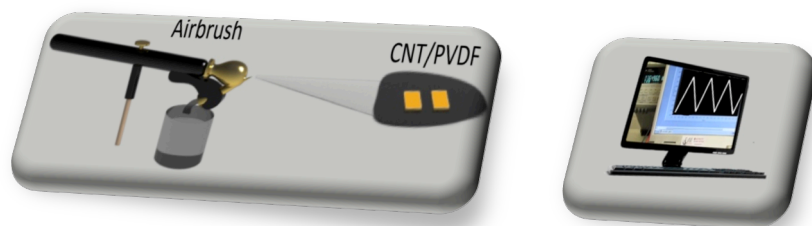
The obtained values are reasonable for the estimated distances in these types of composites, in particular for barrier heights around 1 eV, which is the expected value for these composites [97]. It is to notice that all samples satisfy the tunneling premise for which it must be $\alpha d_0 > 1$ [106]. It is to notice that both in SWCNT and MWCNT, functionalization shifts percolation threshold to higher filler concentration, which in turns decreases the inter-tube gap. This reduction is more apparent in the SWCNT as the threshold concentration is shifted in more than 2.5 wt.% filler content. It is important to show, that independently of the type of CNT and the functionalization, the GF remains similar and so does the piezoresistive mechanism. It is to notice at this point that fact relies on the fact that surface coverage by functionalization is actually quite low ($\sim 1/520$ and $\sim 1/650$ carbon atoms for the SWCNT and MWCNT respectively) and most of the nanotube surface area is bare [74], functionalization modifying therefore the electrical properties of the nanotubes but not the intertube interactions. The piezoresistive mechanism is dominated by the inter-particle distance variations, since the film resistance is mostly dominated by the tunneling resistance. The change in tunneling resistance is in its turn ruled by the inter-tube distance variation with applied strain. The tunneling resistance variation ratio can be used in this way as a powerful indicator of the strain sensitivity of a CNT/polymer composite thin film, controlling both the electrical and electromechanical response of the composites.

Tunneling occurs only between nearest neighbor CNT, the minimum distance between any arbitrary pair of tubes determining the tunneling probability. The minimal tunneling distance depends on the CNT concentration and the values of the tunneling barrier height. In our case, the distance is in the range with the numerical results findings in [97].

4.1.4. Conclusion

The electrical and piezoresistive response of poly(vinylidene fluoride)/carbon nanotube composites has been reported. The observed electrical and electromechanical responses are in accordance with the framework of the percolation theory. The samples were prepared by hot pressing with CNT sample concentrations up to 10 wt.% loadings, with the polymer phase in the non-polar α -phase. The electrical response is characterized by linear I-V curves and a percolation threshold around 2 wt.% loading. The piezoresistive response, quantitatively analysed by the gauge factor, is maximized at concentrations around the percolation threshold. In this region, deformation of the composites induces strong and reversible variations in the CNT network and therefore in the electrical response. The piezoresistive response of CNT/PVDF, composites prepared with both SWCNT and MWCNT with and without functionalization with heptadecafluorooctyl phenyl surface groups is driven by variation of the distance between CNT. The GF is nearly independent of the filler type and concentration, once it is measured close to the percolation threshold, tunneling being in this way the mechanism responsible for the electrical and electromechanical response of the composites. The GF reaches values around 6.2 and the linearity of the response over a wide strain range shows the viability of these materials to be used as piezoresistive sensors. In the same way, the piezoresistive response is stable with the number of cycles and reversible up to temperatures below 100 °C.

Finally, the results show that for a CNT concentration close to the percolation threshold, independently of the type of the matrix used (Epoxy or PVDF), the gauge factor is maximized. Interestingly, this fact is independent of the CNT type or functionalization, as well as of the percolation threshold concentration. The linearity of the response over a wide strain range shows the viability of these materials to be used as piezoresistive sensors.



5. Spray printed CNT/PVDF transducers

This chapter reports on the performance of piezoresistive materials based of carbon nanotube/poly(vinylidene fluoride), CNT/PVDF, composites prepared by spray printing. This chapter is based on the following publication:

Ferreira A., Lanceros-Mendez S. Development of spray-coated carbon nanotube/poly(vinylidene fluoride) piezoresistive materials for large scale applications. Submitted to *Advanced Materials and Interfaces*. 2014.

Surface coatings are important in science and technology with applications that span domains as diverse as biomaterials, optical coatings, photovoltaic cells or corrosion protection. Intense efforts are being directed toward the development of solution-based methods such as ink-jet printing, screen-printing, doctor blading, and spray coating that can meet the manufacturing requirements for cost-effective and large area processing [107, 108].

The present chapter reports on the piezoresistive response of CNT/PVDF composites prepared by spray-printing in order to provide easy fabrication of large area and, patterned – through suitable masks, force and deformation sensors. Further, the sprayed materials are analyzed in comparison to similar composites prepared by solvent casting and hot pressing in order to study the origin of the conduction mechanism of the composites.

5.1. Results and discussion

5.1.1. Morphology and dispersion

The observation of the samples morphology by SEM with different amplifications (Figure 5.1) shows a fibrillar-porous microstructure with good CNT dispersion (Figure 5.1a). This means that the preparation method strongly affects the morphology of the samples and the dispersion of the CNT within the polymer matrix as CNT agglomerates in a polymer compact structure is observed for the samples prepared by hot-pressing (Figure 5.1b) as shown in chapter 4, Figure 4.3.

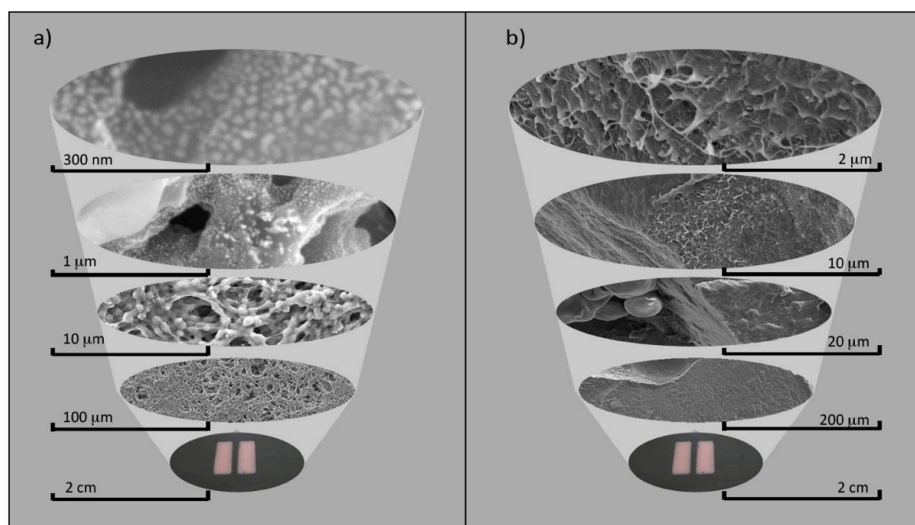


Figure 5.1: SEM images of CNT/PVDF composites with 2 wt.% CNT filler content and prepared by a) spray-coating and b) hot-pressing.

5.1.2. Electrical Conductivity

Representative I-V curves for the PVDF composites with 2 wt.% CNT loadings are shown in Figure 5.2a). The electrical sheet conductivities as a function of CNT concentration are shown in Figure 5.2b). It is observed that the electrical conductivity increases with increasing CNT loading. In particular, the percolation threshold for the composite samples is around 1.5 wt.% filler content, as indicated by the sharp increase in conductivity. The maximum value of the electrical conductivity is of the order of 10^{-3} and is achieved for concentrations around 4-5 wt.%. It is to notice that there are no significant differences in the electrical behaviour of the samples prepared by spray coating and hot-pressing (data from chapter 4) despite the strong differences in the morphology and dispersion of the CNT (Figure 5.1).

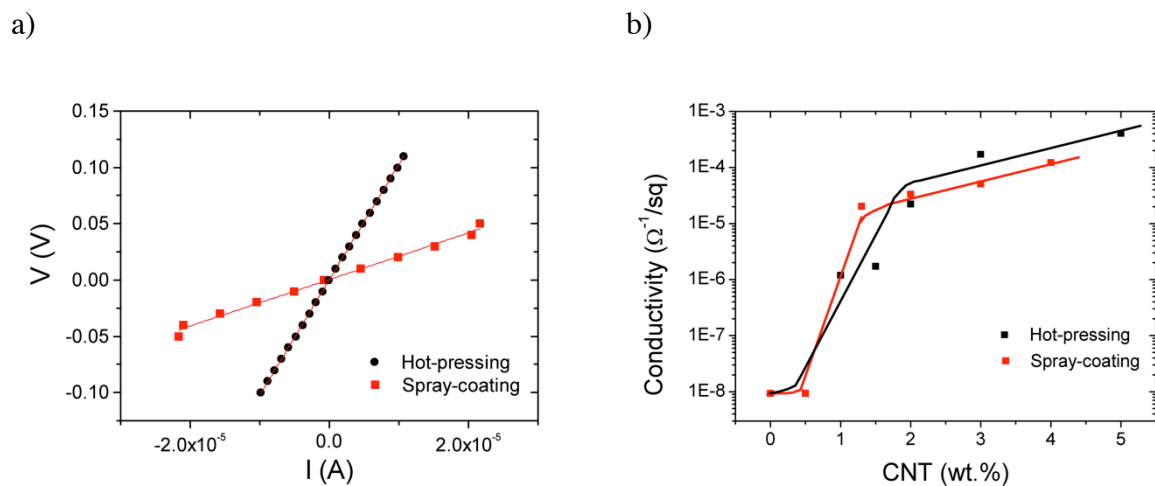


Figure 5.2: a) Typical I-V plots for the composite samples prepared with CNT at a concentration of 2 wt.% over the percolation threshold; b) Concentration dependence of the electrical conductivity for the different composites.

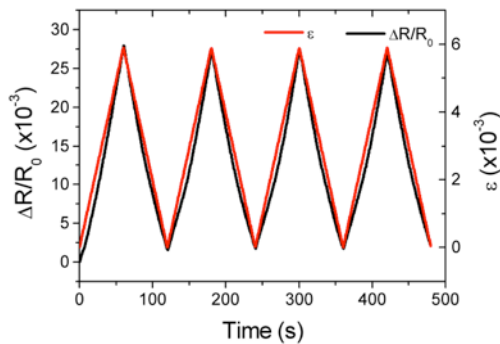
As shown in Figure 5.2a), the current-voltage I-V curves of the nanocomposites show a good linear relationship. Linear I-V relationships close to the percolation threshold has been pointed out as a proof of direct contact between fillers as the main conduction mechanism [41, 43, 109], but it has been shown [110, 111] that composites with tunnelling type conductivity can also show linear I-V relationships, tunnelling resulting in increased conductivity of the composite [97] with respect with composites in which this effect is not present. Further, models involving the formation of capacitor networks have been proposed to be more suitable to explain low percolations threshold [38]. In this respect and due to the

difficulty of understanding the conductivity mechanism from the conductivity curves, it is also interesting to explore the nature of the electromechanical response both, to evaluate the performance of the materials as piezoresistive sensors and to understand the origin of the electrical conductivity.

5.1.3. Electromechanical response

Electromechanical tests were performed in samples with the same percentage of CNT (2 wt.%), close to the percolation threshold, where it has been demonstrated that the GF is the largest [52, 56, 112], as close to the percolation threshold an applied deformation is able to induce strong and reversible variations (Figure 5.3a) in the nanotube network configuration [39], which has a strong influence in the variation of the electrical conductivity. Far from the percolation threshold, network variations are smaller and therefore their effect in the electrical response is also small [101].

a)



b)

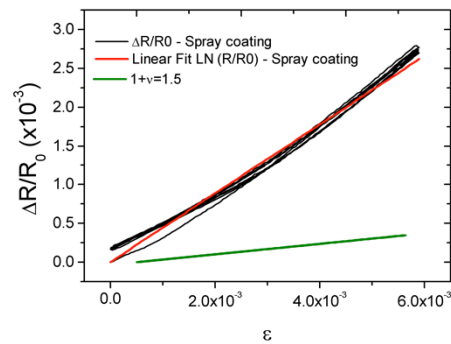


Figure 5.3: a) Cyclic piezoresistive response as a function of time for 2 wt.% CNT content in composites prepared by spray-coating and b) relative resistance variation vs. strain curves and the corresponding fit with for the determination of the Gauge Factor.

Figure 5.3a) shows a typical example of the electro-mechanical experiments as well as the relative resistance variation versus strain used for the calculation of the GF (Figure 5.3b). Further, Figure 5.4 shows the cyclic piezoresistive response over 100 loading-unloading cycles.

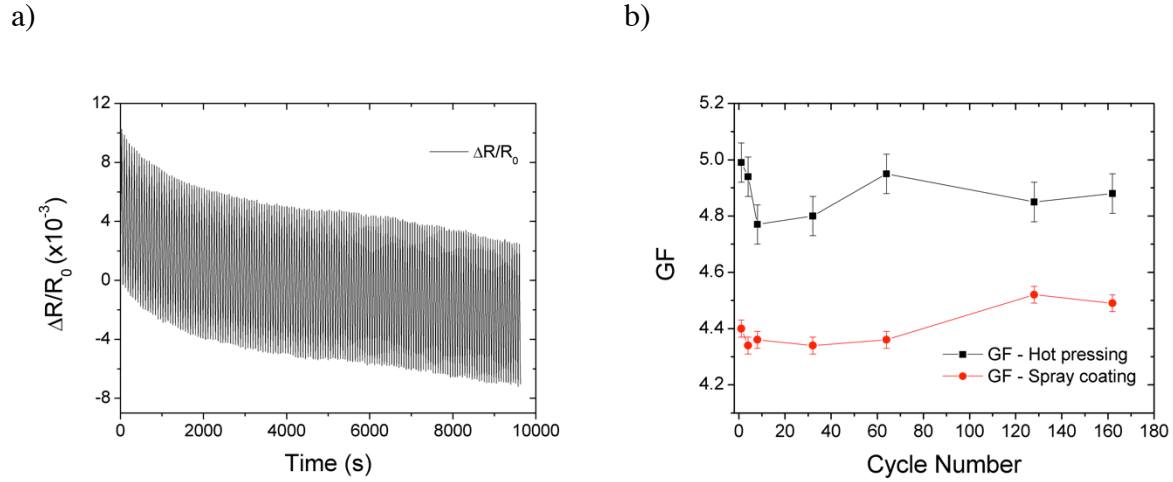


Figure 5.4: Cyclic piezoresistive response over 100 cycles as a function of time for 2 wt.% CNT content samples prepared by spray-coating and b) change in GF as a function of the number of bending cycles. Experimental conditions: bending of 1 mm, deformation velocity of 2 mm min⁻¹, room temperature. The data for the samples prepared after hot pressing are obtained from [52].

The initial decrease of the resistance for increasing number or cycles points out to fatigue effects indicative of irreversible variations in the filler network responsible for the conductivity of the composites. This fact is confirmed by the decreases of the GF with increasing the number of cycles (Figure 5.4b) for the first cycles, showing a trend to stabilization after that.

Figure 5.3a) and 5.4a) shows that the electrical resistance changes fairly linearly with the applied strain and that the linearity is maintained for the different cycles. The curves were thus fitted by linear regression as shown in Figure 5.3b). The slope of the linear fit with equation 2.3 (obtained with a R-square of 0.99) corresponds to the GF of the sample and is presented in Table 5.1.

From Solef®PVDF datasheet, the Poisson ratio of PVDF is 0.35 at room temperature, which means that the geometric effect contribution to GF is around 1.35. Therefore, the obtained values of the GF , which are above 4 (Table 5.1), show a strong intrinsic contribution of the composite to the GF (equation 3).

Table 5-1: GF values obtained from the linear fit of $\Delta R/R_0$ as function of stress.

	GF	Standard Error
Spray-coating	4.43	0.02
Hot-pressed [52]	4.93	0.01

It is to notice in Table 5.1 that, in general, the electro-mechanical properties, as quantified by the GF , are similar for the samples, independently of the type of preparation, as previously observed for the electrical behaviour. The piezoresistive response can be discussed in terms of tunnelling, as it is the most consolidated mechanism for the interpretation of the piezoresistive response in this type of materials [85], and it is supported, in our case, by the slight non-linear dependence of the resistance change vs strain [85].

In this scope and according to a heterogeneous fibril model, the resistance (R) of carbon nanotube composites is determined by the following relationship of tunnelling resistance (R_T) and the CNT gap change-dependent resistance (R_B) [104, 105]:

$$R = \frac{L_T}{A_T} R_T + \frac{L_B}{A_B} R_B, \quad (5.1)$$

that can be rewritten as described previously in [104],

$$R(T) = R_m \left(1 + \exp \left[\frac{E_a}{k_B T} \right] \right) + R_t \exp \left[\frac{E_a}{k_B T} \right] \quad (5.2)$$

In this approach, R_m and R_t are proportional constants, E_a is the tunnel activation and E_g is the band gap of CNT, k_B is the Boltzmann constant, and T is temperature [104, 105]. Here, the conducting pathways are assumed to be connected in parallel and the resistance of pathways perpendicular to the current are neglected. If conduction is dominated by tunnelling through the polymer gaps separating the CNT and the resistance of the polymer matrix is much higher than the resistance of the particles, R_B , the resistance of the fillers can be neglected, ($R_B \sim 0$) [104]. Thus, assuming that R_m is constant, the resistance change under stress can be expressed by:

$$\frac{R(\varepsilon)}{R_0} = \exp(2\alpha d_0 \varepsilon), \quad (5.3)$$

$$\alpha = \frac{2\pi}{h} \sqrt{2m\phi}, \quad (5.4)$$

where $R(\varepsilon)$ and R_0 are the composite resistance under tensile strain (ε) and the original resistance at $\varepsilon = 0$, respectively; d_0 is the tunneling distance between CNT, h is Planck's constant, m is the mass of the charge carriers, and ϕ is the tunneling barrier height [106]. In this model, if the tunneling distance is responsible for the resistance change under stress, the

plot of Equation 5.3 versus tensile strain (ϵ) should be linear with a slope of $2\alpha d_0$ (Figure 5.5).

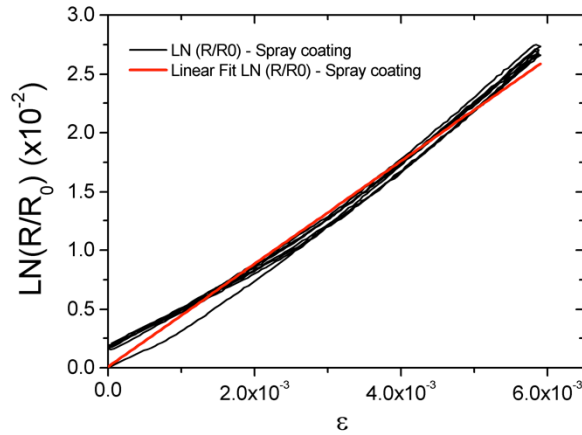


Figure 5.5: Surface sensing resistance change $Ln(R(\epsilon)/R_0)$ as function of stress and corresponding fittings with equation 5.3.

Table 5.2 show the calculated distances between two filler particles for the different samples using the parameters derived from the fit with Equation 5.3 (Figure 5.5) assuming different barrier heights. Further, the data are compared with the ones obtained for the samples prepared after hot-pressing reported in [52].

Table 5-2: Distance between two CNT, results of Equation 5.3 as function of stress.

Samples	wt. %	Slope	Standard Error	αd_0	Tunneling barrier height - ϕ (eV)				
					0,5	0,75	1	2	4
					d_0 (nm)	d_0 (nm)	d_0 (nm)	d_0 (nm)	d_0 (nm)
Spray coating	2	4.37	0.02	2.19	0.60	0.49	0.43	0.30	0.21
Hot-pressed [52]	2	4.91	0.01	2.45	0.68	0.55	0.48	0.34	0.24

The obtained values are reasonable for the estimated distances in these type of composites, in particular for barrier heights around 1 eV, which is the expected value for these composites [97]. It is to notice that all samples satisfy the tunneling premise of $\alpha d_0 > 1$ [106]. It is important to notice, that independently of the type of method of preparation, the GF remains similar and so does the piezoresistive mechanism. Therefore, the observed changes in the microstructure do not lead to changes in the electrical properties of the

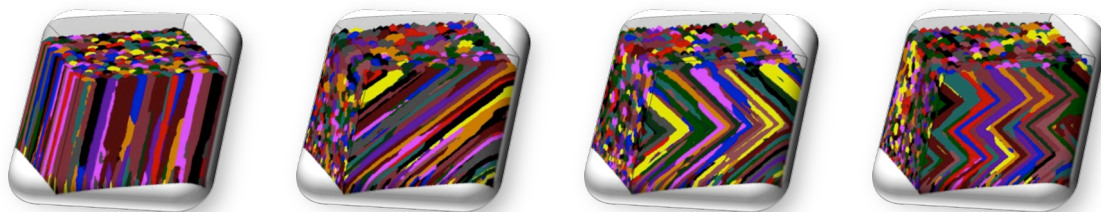
composites. The piezoresistive mechanism is dominated by filler distance variations, since the film resistance is mostly dominated by the tunneling resistance. The change in tunneling resistance is in its turn ruled by the inter-tube distance variation with applied strain. The tunneling resistance variation ratio can be used in this way as a powerful indicator of the strain sensitivity of a CNT/polymer composite thin film, controlling both the electrical and electromechanical response of the composites.

Tunneling occurs only between nearest neighbor CNT, the minimum distance between any arbitrary pair of tubes determining the tunneling probability. The minimal tunneling distance depends on the CNT concentration and the values of the tunneling barrier height. In our case, the distance is in the range with the numerical results findings in [97].

It is important to notice that the obtained values of electrical conductivity and piezoresistive response do not depend on the preparation method, conferring to the spay-coating method strong advantages for large area and patterned (through the use of suitable masks) sensor applications.

5.1.4. Conclusion

A method for the preparation of large-scale piezoresistive sensors based on spray coating is presented. It is shown that the electrical properties and the electromechanical response of the material are independent of the preparation method: spray-coating or hot-pressing. The piezoresistive response of the CNT/PVDF composites, as quantified by the GF, is ruled by tunneling and reaches values above 4.4, which indicates a main contribution from intrinsic piezoresistive effect and demonstrating the suitability of these materials for sensor applications.



6. Development of stretchable interconnections

This chapter reports on the main characteristics of the nanostructured functional of Ti-Ag electrodes produced in GLAD system in order to be applied to the polymer composites. This chapter is based on the following publication:

A. Ferreira, C. Lopes, N. Martin, S. Lanceros-Méndez, F. Vaz. Nanostructured functional Ti-Ag electrodes for large deformation sensor applications. Submitted to *Sensors and Actuators A*. 2014.

Due to the different nature of this chapter, in comparison with the previous ones, it has a different structure more suitable for the presentation of the processing of the materials and the presentation and discussion of the experimental results.

As previously mentioned, composite materials can be developed with the ability to significantly change the electrical response when subjected to strains. However, one of the critical problems of large strain sensors is the dependability on the elastic interconnections between the polymer composite and the signal acquisition circuit. So, the main purpose of this chapter is the development of thin film-based stretchable electrodes suitable for the different types of produced sensors. Columnar Ti-Ag thin films with Ag inclusions were prepared by D.C. magnetron sputtering on carbon nanotube/poly(vinylidene fluoride) - CNT/PVDF- piezoresistive composites. *GLancing Angle Deposition*, GLAD, technique was used to change the typical columnar growth microstructure obtained by conventional sputtering, into different growing architectures, such as inclined columns and zigzag profiles, in order to tune mechanical and electrical responses of the materials.

6.1. Experimental details

6.1.1. Titanium – Silver thin films

Ti-Ag thin films were deposited by D.C. reactive magnetron sputtering inside a stainless-steel custom-made vacuum reactor with a volume of 40 L, Figure 6.1.

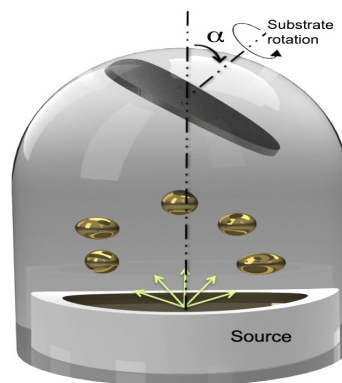


Figure 6.1: Schematic representation of the GLAD system, where α is the orientation of the substrate relative to the impinging vapor flux.

The reactor, equipped with a circular planar and water cooled magnetron sputtering source, was evacuated with a turbomolecular pump, backed by a mechanical pump, in order to obtain an ultimate pressure of 10^{-5} Pa. A titanium target (purity 99.6 at.%, 51 mm diameter) was used and 11 inserts of silver (purity 99.9 at.%, 2 mm diameter) were placed

equidistant from each other, within the preferential erosion zone of the target. The composite target was sputtered under a pure argon atmosphere, with a constant flow rate of 2.4 sccm, corresponding to a total pressure of 0.3 Pa. The pumping speed was set constant at $S = 10 \text{ L s}^{-1}$. Before each deposition, the CNT/PVDF samples were cleaned with ethanol and introduced through a 1 L airlock. In order to remove the target surface contamination layer, a pre-sputtering of the composite target was performed for 5 min. Finally the samples were positioned at 50 mm from the target and grounded. The depositions were carried out at room temperature and the Ti-Ag composite target powered with a constant current density of 24.5 A.m^{-2} . The deposition time was adjusted in order to obtain a thickness range between 400 nm and 900 nm. All the sputtering parameters were optimized taking into account the strong changes in the mechanical behaviour of the polymer that occurs at $\sim 90^\circ\text{C}$ [101].

In order to study the change in the electromechanical response of the thin films, a set of different architectures were tailored by varying the direction of the incident particles flux. Four different types of films were grown in order to correlate the growth conditions (conventional and zigzag approaches) and the specific features of the GLAD-like prepared films with the response of the thin films and piezoresistive composites. Figure 6.2 shows a schematic illustration of the different prepared films and their main microstructural features.

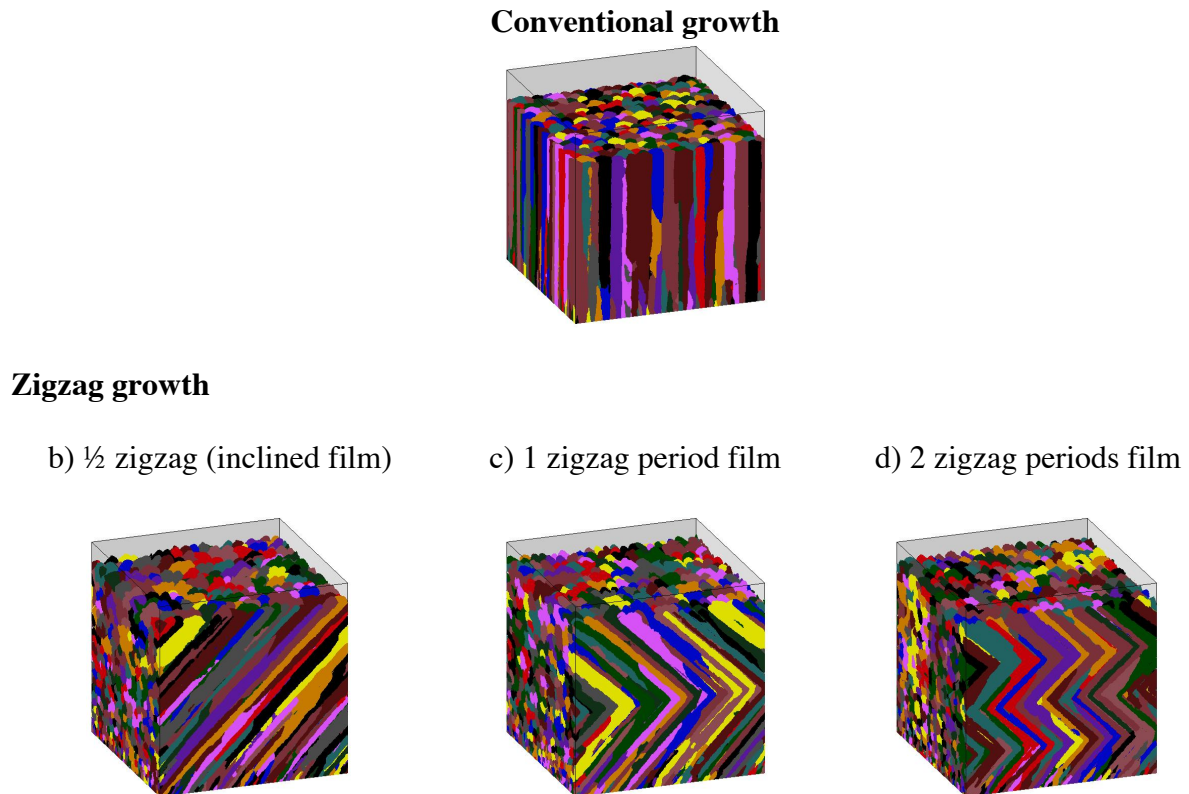


Figure 6.2: Schematic representation of the thin film microstructural features.

PVD techniques use normal incidence to obtain the typical columnar growth normal to the deposition substrate, Figure 6.2a). With adequate operating conditions, GLAD technique allows obtaining columnar microstructures with specific architectures by controlling the orientation of the substrate relative to the impinging vapor flux, as illustrated in Figures 6.2b), 6.2c) and 6.2d). In the observed columns, when the incident angles of the particles flux α increase with respect to the sample surface, the angle β of the column with respect to the sample surface, increases the same way.

6.1.2. Electrical resistance measurements

Two different electrical conductivity measurements were performed in the samples. Electrical resistance of the CNT/PVDF composites was calculated from the slope of I–V curves, measured at room temperature with an automated Keithley 487 picoammeter/voltage source. I–V data points were collected between Au contacts, deposited on both sides of the samples with a Polaron SC502 sputter coater. Volume resistivity was measured with circular contacts of 5 mm diameter with an applied voltage ranging between ± 10 V and measuring the current. The resistivity ρ (Ωm) was calculated by [113]:

$$\rho = \frac{R.A}{d} \quad (6.1)$$

where R is the resistance of the composite (Ω), d the thickness (m) and A the area of the electrodes (m^2).

Second, the electrical conductivity of Ti-Ag thin films was measured at room temperature, using the four-probe van der Pauw method [114, 115]. The measurements were carried out in a custom-made dark chamber. The error associated to the electrical measurements is below 1%.

6.1.3. Electromechanical characterization

Electromechanical tests were performed considering the whole system: CNT/PVDF polymer coated with the Ti-Ag thin films. The electrical resistance of the samples (approximate dimensions: 60×10 mm² and ~ 1 mm of thickness) was measured through the Ti-Ag electrodes with an Agilent 34401A multimeter during the mechanical deformation of the sample, applied with an universal testing machine from Shimadzu (model AG-IS, with a load cell of 1 kN). Two different mechanical solicitations were applied to the samples. During the so-called method 1, mechanical experiments were

performed in the tensile mode (Figure 6.3a); in the method 2, 4-point-bending deformation was applied to the samples (Figure 6.3b).

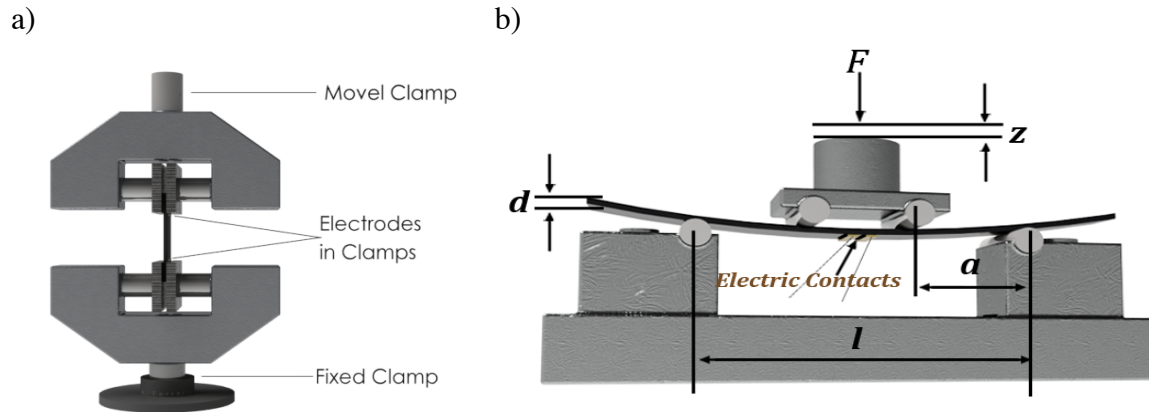


Figure 6.3: Schematic representation of the experimental configuration of the, a) clamps for the stress-strain experiments with simultaneous electrical measurements for electrical response evaluation of the samples by applying uniaxial stress, b) Representation of the 4-point bending tests (method 2) apparatus where z is the vertical displacement, d is the thickness of the sample and a is the distance between the first and the second bending points (15 mm). The electrodes are in the center of the sample.

The evaluation of the electrical resistance response during the uniaxial stress tests (Figure 6.3a) was performed at speed rate of 0.5 mm/min and at a maximum strain level of 10%. For the 4-point-bending measurements (Figure 6.3b), the Ti-Ag electrodes with an area of $10 \times 1 \text{ mm}^2$, were placed at the bottom of the sample. For all experiments, 4 loading-unloading cycles were performed and the average electromechanical response was evaluated. All these experiments were carried out at room temperature.

6.2. Morphological analysis

The morphological features of the Ti-Ag thin films was probed by scanning electron microscopy (SEM). Cross-section micrographs were obtained at room temperature in a FEI Quanta 400FEG ESEM apparatus operating at 15 keV.

Additional information about surface properties (roughness and surface morphology) was obtained by atomic force microscopy (AFM), using a MultiMode STM microscope controlled by the Nanoscope III (tapping mode) system. The measurements were performed over surface scan areas of $5 \times 5 \text{ }\mu\text{m}^2$.

6.3. Results and discussion

6.3.1. Electrical properties of Ti-Ag electrodes

In order to study the electrical properties of the Ti-Ag electrodes sputtered by GLAD, electrical resistivity measurements at room temperature were carried out. The electrical behaviour of the Ti-Ag thin films is presented in Figure 6.4, where the influence of the different processing parameters -number of zigzag periods and sputter angles- was analysed. The results plotted in Figure 6.4 show that the films are characterized by suitable electrical conductivity for sensor electrode applications, with varying properties depending on the number of periods and, mainly, deposition angle. The Ti-Ag thin films exhibit conductivity values in the order of $10^{-3} \mu\text{Sm}^{-1}$ several orders of magnitude higher than the polymer composite ($10^9 \mu\text{Sm}^{-1}$) and thus adequate to be used as electrodes. Further, a slight enhancement of the electrical conductivity is observed for the lowest incident angles ($\alpha < 40^\circ$) and for the highest number of periods (Figure 6.4), which is correlated with changes in the grain boundaries, in particular with the voids between the columnar structures. These voids are promoted as the incident angle increases and therefore the column angle β increases [116, 117].

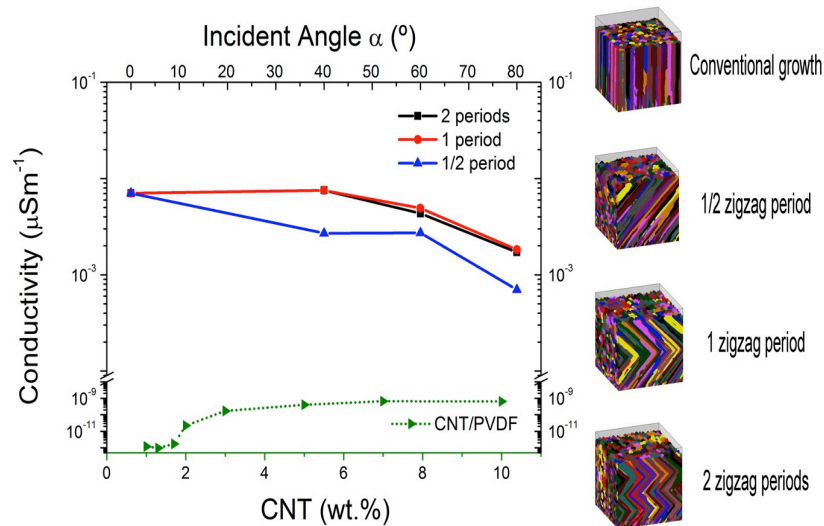


Figure 6.4 - Electrical conductivity of Ti-Ag films as a function of the incident angle (a) and the number of periods, and electrical conductivity of polymer composite as a function of CNT (wt.%).

The effects of Ag additions to a stoichiometric TiN matrix has been studied [118] and it is reported that for intermediate Ag contents (between ~ 6 and ~ 20 at.%), highly conductive Ag particles are placed among the TiN columns, providing an increased number of conduction paths. Further, in the case of the inclined features, the increase of both α and β

angles give rise to increased porosity [119]. Thus, scattering at the column's interface is favoured, which reduces the electronic transport properties of the coatings [119]. Additional parameters such as temperature (T), film thickness (d), grain size (D) and the mean free path of the electrons in the film (λ_e) also affect the electrical conductivity (σ) of the metallic thin films [116]. These parameters are also correlated with changes in the grain boundaries, mainly in the column frontiers, which behave as a potential barrier, which decreases the probability of the electron transmission [116]. Thus, the variations in the electrical conductivity are mainly due to the modifications on the film's architecture and growing conditions. As demonstrated in [120], the major contribution to the total resistivity comes from electron scattering at grain boundaries and therefore to the significant modifications of the film's morphology.

6.3.2. Electrical behaviour of Ti-Ag films under uniaxial stretching

To minimize the overall stiffness of the sensors, materials for both the matrix and the electrically active components should have low Young modulus and an ability to accommodate large strain deformations with a linear, elastic response. Thus, mechanical response and electrical transport properties are important.

Regarding the thin films prepared within the frame of this work, the electrical resistance for deformations up to 10% along the axial direction of the incident angle are shown in Figure 6.5.

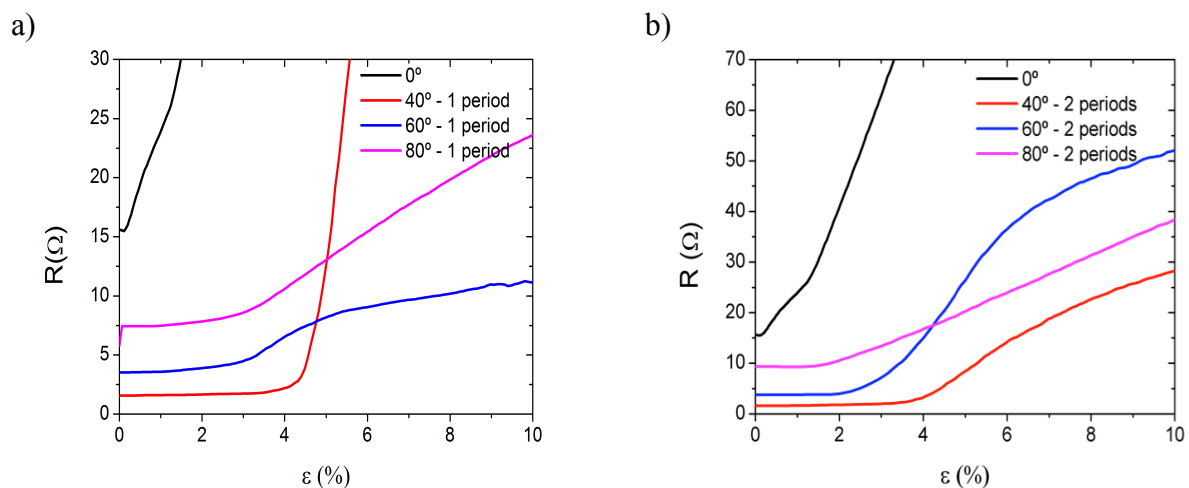


Figure 6.5: Electrical resistance of the band R as a function of the tensile strain ϵ of the sputtered Ti-Ag samples for the different incident angles $\alpha = 0, 40, 60$ and 80° and geometries: a) 1 zigzag period; b) 2 zigzags periods.

The results shown in Figure 6.5 reveal two very distinct behaviors. On the one hand, the thin films deposited in the conventional way ($\alpha = 0^\circ$) show a very poor resistance to stretching, with the electrical resistance increases sharply after the application of the deformation. As shown in Figure 6.5, upon uniaxial stretching, the samples deposited in conventional approach ($\alpha = 0^\circ$) reveal that the resistance starts increasing immediately after the stretching started, which demonstrates its inadequacy for the targeted sensor applications. This undesirable behaviour is actually expected as demonstrated in [23, 60], where electrodes produced with conventional sputtering deposition resulted in the smallest strain range before loss of conductivity, which was limited to $\varepsilon = 3\%$. At 1% strain, cracks started to appear perpendicularly to the stretch direction, and the cracks became wide enough to completely interrupt the conducting path for strains of 3%. On the other hand, to solve this limitation, patterning metal traces can be used [23, 24, 121]. When carefully designed, the patterned electrode still allows for the polymer to move and expand in the desired direction without damaging the metallic thin-film.

For the prepared zigzag structures, the resistance starts increasing only for strain ranging from 2 to 3% (Figure 6.5). Furthermore, and even for the higher strain, the surface resistance increases smoothly, mainly due to a geometrical effect, demonstrating the large difference with respect to the conventional deposited films. A sharp increase of the electrical resistance occurs only above 10% strain, indicating electrical conductivity failure due to film damage (Figure 6.5).

The structures with 2 periods (4 zigzags) presented in Figure 6.5b show no relevant variations of the electrical resistance for strains of $\sim 4\%$ for an incident angle of 40° . On the other hand, the resistance of the samples prepared with $\alpha = 60^\circ$ show variations of the electrical resistance for stretching around 3%. However, it is worth to note that these samples also showed a better strain distribution, with just a small increase of resistance up to 10% strain, allowing their use for high strain sensor applications. Failure is expected in regions where the highest plastic strain concentration is located [23, 60]. In a general way, an increase of the incident angle and the number of zigzags promotes a reduction in the accumulated strain (Figure 6.5).

6.3.3. Morphological analyses of Ti-Ag films

In order to reduce even more the strain in the metal conductor, without sacrificing the electrical performance and/or changing the amplitude or period of the design, the obtained results show that the number of zigzags can be further optimized (increased), increasing their number with several periods of smaller thickness or even with periods of varying thicknesses. This “multi trace” films may improve the stretchability and reduce the induced stresses [119].

Figure 6.6 shows the cross-section images of the sputtered GLAD samples, where all the films seem to exhibit a typical columnar microstructure. The tilting of columns increases with the incident angle α . Nonetheless, the incident angle α and the column angle β are not equal due to shadowing effects [116, 117]. As the total film thickness was kept approximately constant, with increasing number of zigzag periods, the single period thickness decreases. For an incident angle $\alpha = 40^\circ$, the obtained inclined (1/2 period zigzag) and zigzag architectures (1 and 2 periods) exhibit a weakly distinguishable columnar structure. The column angle β cannot be accurately determined for any zigzag period. It is in agreement with the quite dense structure typically observed in GLAD thin films prepared with incident angles lower than 60° . The shadowing effect is not relevant enough for incident angles lower than 60° . The oriented growth is favoured but insufficiently to produce a clear defined cross section morphology [116-118]. For incident angles α higher than 60° , inclined as well as zigzag columns are better viewed. The column angle is $\beta = 40^\circ$ and 45° (for any zigzag period) for a corresponding incident angle $\alpha = 60^\circ$ and 80° , respectively. These close β values are expected within the GLAD sputtering process due to the dispersion of sputtered particles (the latter do not have a ballistic trajectory because of the sputtering pressure required to maintain the plasma). As a result, the β angle tends to saturate in spite of an increase of the incident angle and the films do not exhibit significant changes of their cross section morphology. In addition, with increasing the incident angle from 0° to a maximum of 80° , the structures become less dense and compact and an enhancement of the inter-columnar spacing is perceivable, independently of the number of periods. Moreover a closer look also reveals well defined columnar features for incident angles of 60° and 80° , particularly evident for $\alpha = 80^\circ$.

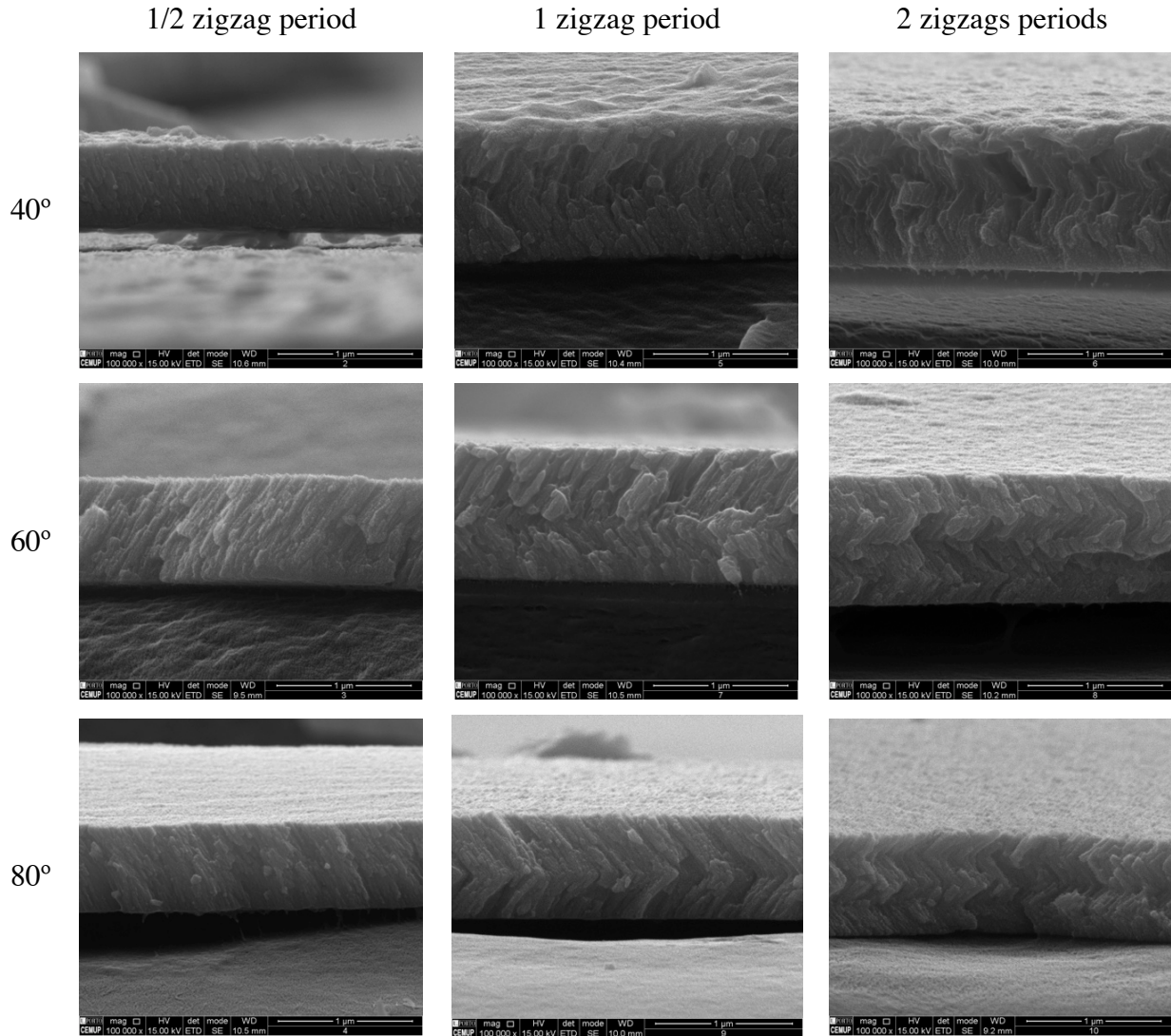


Figure 6.6 - SEM cross-section micrographs of the sputtered Ti-Ag samples for incident angles $\alpha = 0, 40, 60$ and 80° and $\frac{1}{2}, 1$ and 2 zigzags periods.

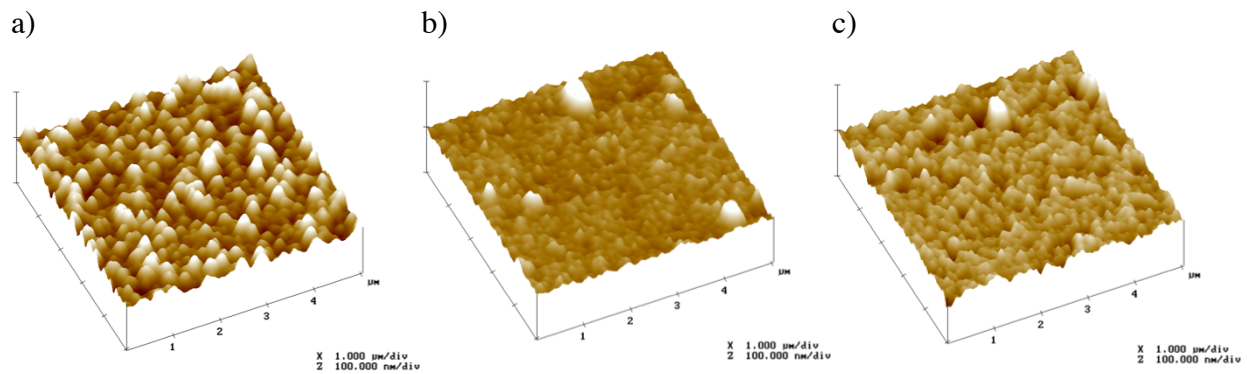
These results show the variations in the grain boundaries, mainly in the column frontiers which decreases the probability of the electron conduction [116] and consequently decreases the electrical conductivity.

AFM was used to characterize the morphology and surface roughness of the Ti-Ag samples with a scan area $5 \times 5 \mu\text{m}$. The influence of this α angle on the surface roughness is represented in Table 6.1.

Table 6-1: Surface roughness of the Ti-Ag films with different incident angles of deposition and 2 zigzag periods.

Sample	Mean square roughness (Rq) <i>nm</i>	Mean roughness (Ra) <i>nm</i>	Max height (Rmax) <i>nm</i>
$\alpha=40^\circ$	8.4	6.7	61.7
$\alpha=60^\circ$	5.8	3.5	73.1
$\alpha=80^\circ$	6.8	5.1	86.6

Figure 6.7 and table 6.1 show that the surface of the samples prepared with an angle of deposition $\alpha = 60^\circ$ are the smoother ones with a rms roughness of 5.8 nm. The statistical mean roughness of the surface is about 3.5 nm, while the maximum height is about 73.1 nm. The results show maximum roughness for the samples prepared with $\alpha=40^\circ$ and $\alpha=80^\circ$ and therefore there is no relation between surface roughness and electromechanical response (Figure 6.5b) but the latter is fully determined by the column angle.

**Figure 6.7: AFM topographic images of sputtered Ti-Ag samples with 2 zigzag periods and for different incident angles: a) $\alpha = 40^\circ$; b) $\alpha = 60^\circ$; c) $\alpha = 80^\circ$.**

6.3.4. Electromechanical response of the films

The electrical and piezoresistive response of carbon nanotube/poly(vinylidene fluoride) composites has been reported in [52]. The observed electrical and electromechanical responses are in accordance with the framework of the percolation theory. The piezoresistive response, quantitatively analysed by the gauge factor, is maximized at concentrations around the percolation threshold. In this region, the deformation of the composites induces strong and reversible variations in the CNT network and therefore in the electrical response. The maximum value of the gauge factor is 6.2 and the linearity of the response over a wide strain range shows the viability of these materials to be used as piezoresistive sensors. In the same way, the piezoresistive response is stable with the number of cycles and reversible up to temperatures below 100 °C [52].

In this study, electromechanical tests on the Ti-Ag coated carbon nanotube/poly(vinylidene fluoride) composites were performed on composites with the same percentage of CNT (3 wt.%), i.e. around the percolation threshold, where the GF is the largest [52]. In this way, it was analysed whether the structure of the electrodes influences the signal response of the transducers.

The stability of the piezoresistive response was analysed for the different GLAD Ti-Ag electrodes prepared with varying incident angles α and number of zigzags. Figure 6.8a), b), c) shows the strain tests performed in the samples with electrodes with 2 zigzag periods prepared with an incident angle $\alpha = 40, 60$ and 80° . The 2 zigzag period samples were selected as they provide the most stable piezoresistive signal.

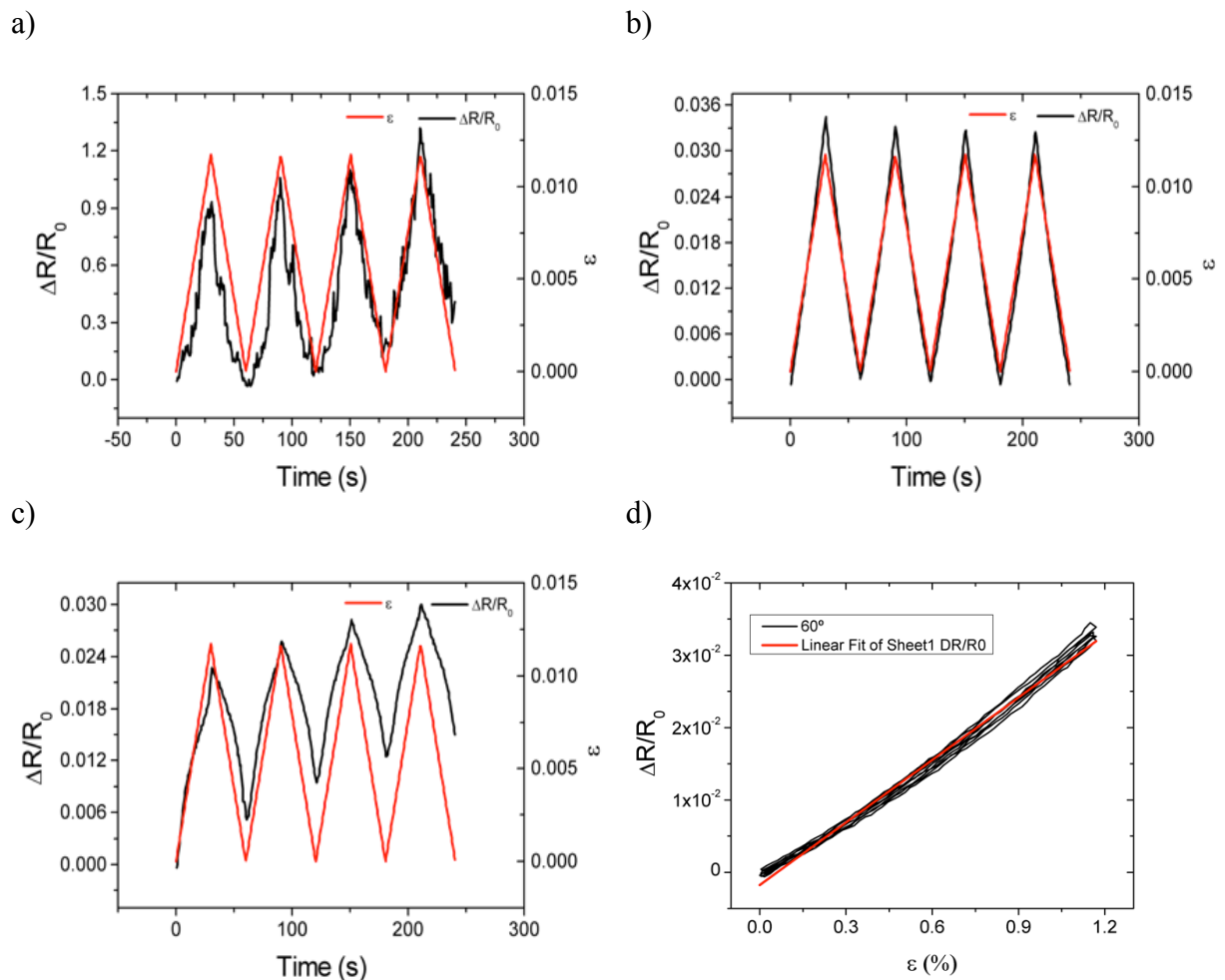


Figure 6.8: Strain applied to 2 zigzag periods Ti-Ag films deposited on PVDF substrates with 3 wt.% CNT's and the corresponding resistance variation vs. time for four up-down cycles. The z -deformation is 1 mm and the deformation velocity is 0.5 mm/min at room temperature. The incident angle is a) $\alpha = 40^\circ$; b) $\alpha = 60^\circ$ and c) $\alpha = 80^\circ$.

The increasing of the incident and column angles (α and β , respectively), from $\alpha=0^\circ$ to $\alpha=60^\circ$, as well as the number of zigzag periods enhances the electromechanical response. Above an incident angle of 60° there is a divergence between the loading and unloading cycles, due to strong changes in the mechanical behaviour of the Ti-Ag films, leading to a very poor resistance to stretching as shown in Figure 6.4. These results show that the electrode structure has a pronounced influence on the electrical conductivity response of the polymer composite (e.g. variations on the resistivity) and therefore in the performance of the sensor.

As shown in Figure 6.8d) the electrical resistance changes fairly linearly with the applied strain and that the linearity is maintained for the different cycles and for the different samples. The curves were thus fitted by linear regression.

The GF is defined as the ratio of fractional change in electrical resistance to the fractional change in length (strain), $GF=(\Delta R/R_0)/\epsilon$ [79]. The slope of the linear fit with equation is presented in table 6.2.

Table 6-2: GF values resulting of the linear fit of $\Delta R/R_0$ as function of stress ϵ .

α	GF	Standard Error
40°	85	2
60°	2.88	0.01
80°	1.44	0.05

From Solef®PVDF datasheet, the Poisson ratio of PVDF is 0.35 at room temperature, which means that the geometric effect contribution to GF is around 1.35. Therefore, the obtained values of the GF , that are above this value (Table 6.2), show a strong intrinsic contribution of the CNT/polymer composite to the GF for the films prepared with $\alpha = 40^\circ$ and $\alpha = 60^\circ$, but roughly negligible for $\alpha = 80^\circ$. In this way, as demonstrated in previous work, chapter 4, for CNT concentrations above 3 wt.%, the geometric factor is the dominant one, but just below 2 wt.% CNT loading, the intrinsic contribution to the GF is dominant. In this case, the change in conductivity of the Ti-Ag films induces strong variation of the response of the sensors due to their varying electrical response, which superimposes the variation of the piezoresistive composite [65, 122]. It can be further stated that whereas the electromechanical signal is mainly due to the polymer sensing element for electrodes prepared with $\alpha = 40^\circ$ and 80° , the strong variations in resistivity under mechanical

solicitation for the sample prepared with $\alpha = 40^\circ$ is ascribed to variation in the electrode itself. Upon stable response over varying cycles, the results show a promising way to use the films as piezoresistive sensors themselves. This is correlated with changes in the grain boundaries, mainly in the column frontiers which promote the tunneling resistance change [116]. The variation of the conductivity with angle α is mainly due to significant modifications of the film's morphology. The obtained values are reasonable for these types of composites; however, denser and compact structures with smoother surfaces showed a good strain distribution coupled with appropriate electrical conductivity, favoring the electromechanical response of the coated polymer. The best results were obtained when the polymer was coated with Ti-Ag films produced with intermediate incident angles.

6.4. Conclusion

Ti-Ag thin films were prepared with a systematic variation of the incident angle $\alpha = 40^\circ, 60^\circ$ and 80° and number of zigzag periods in order to be applied as electrodes in high strain piezoresistive polymer based composites based on CNT and PVDF. Upon uniaxial stretching, for the zigzag structures, the resistance starts increasing for strains up to 3 %, rising sharply for strains above 10 %, due to thin film mechanical and electrical failure. By increasing the number of zigzags, the change in conductivity of the Ti-Ag films induces strong variation of the response of the sensors due to their varying electrical response, which superimposes the variation of the response of the piezoresistive composite and the best results were obtained when the polymer was coated with intermediate incident angles ($\alpha = 60^\circ$). The results show that the electrodes structure has a pronounced influence on the overall sensor response leading to values of the GF up to 85 mainly due to the electromechanical contribution of the thin film, which stability has to be studied for potential use for sensor applications itself.



7. Prototype fabrication and testing

This chapter reports on the fabrication of the sensor array prototype and its tests at the CRPG - Centro de Reabilitação Profissional de Gaia (Vocational Rehabilitation Center).

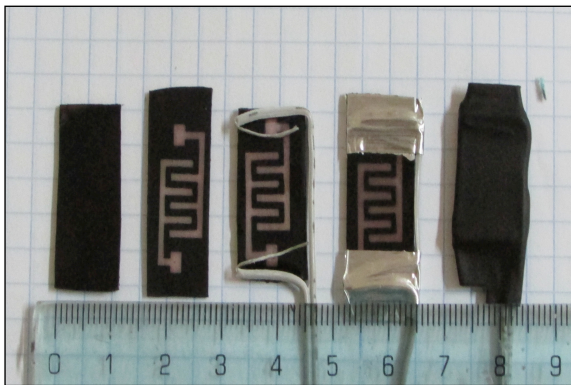
This section is centred on the fabrication and testing of a sensor array prototype and the corresponding study conducted at the CRPG - Centro de Reabilitação Profissional de Vila Nova de Gaia (Vocational Rehabilitation Center).

7.1. Results and discussion

7.1.1. Sensors construction process

For mapping the pressure fields at the external prosthesis socket/stump interface, in particular at lower limbs, a sensor array was developed from piezoresistive polymer based materials to measure quasi-static and dynamic deformations. A large set of sensors was prepared from CNT/PVDF, with 2 wt.% of CNT, with dimensions of $10 \times 25 \text{ mm}^2$ and $\sim 1 \text{ mm}$ thickness, as described in chapter 4 and 6. They are shown in (Figure 7.1 a) and tested one by one (Figure 7.1b).

a)



b)

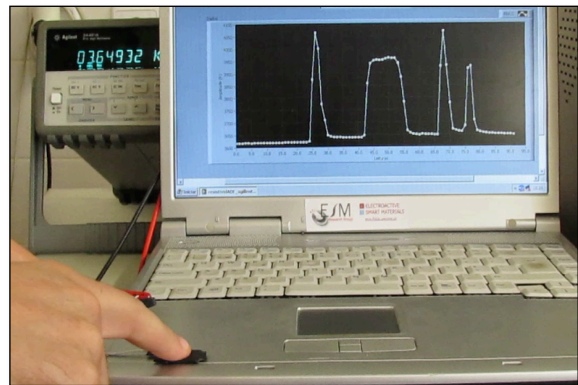


Figure 7.1: Sensors construction process, a) Set of sensors was prepared from CNT/ PVDF with 2 wt.% with dimensions of $10 \times 25 \text{ mm}^2$ and 1mm thickness, b) Sensors tested one by one.

Thus, a large set of sensors (Figure 7.2 a) was connected in an array (Figure 7.2b) to monitor the prosthesis. The block of sensor interface (Figure 7.2b) should be highly configurable to allow that the control system can adjust perfectly the condition circuit to the sensor to read, because although are all piezoresistive sensors prepared in the same way, the initial resistance of the various sensors is not the same and also the electromechanical response is not identical.

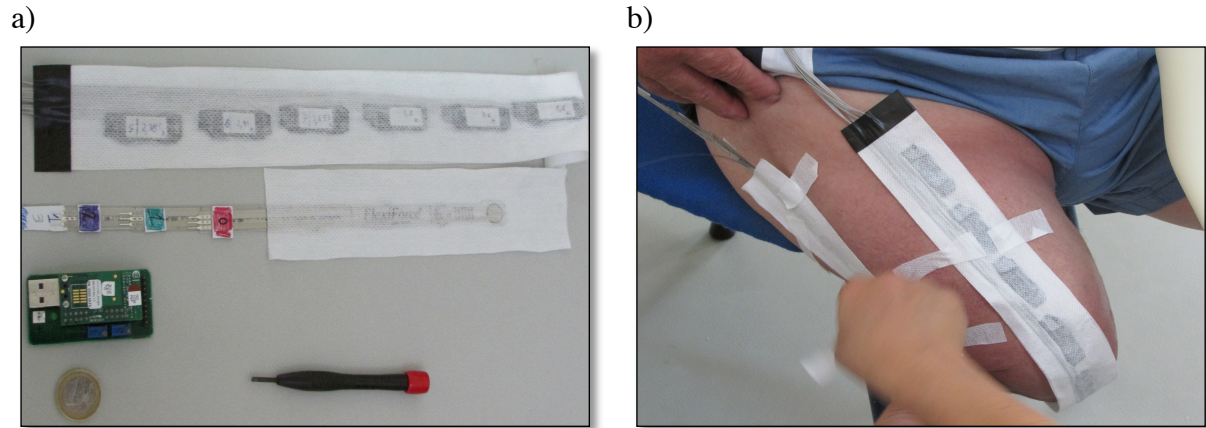


Figure 7.2: a) Set of sensors connected in an array, b) The block of sensors to monitor the prosthesis.

7.1.2. Prototyping test

The subjects, Table 7.1, transfemoral (TF) and transtibial (TT) amputees, walked for 2 minutes in a crosswalk at a comfortable speed (0.33 m/s), simulating a normal walk of approximately 40 m.

Table 7-1: Patients studies of internal pressures in a transfemoral and transtibial amputee of the residual limb.

Subject #	Level amp	Cause	Interface Type
1	TF	Traumatic	-
2	TT	Traumatic	Otto Bock
3	TT	Traumatic	-
4	TF	Accident	Össur ?Dermo

The transducers were placed in different planes of the body (Figure 7.3). The anterior–posterior plane (AP) was defined by the Saggital plane. The medial–lateral plane (ML) was defined by the Frontal plane perpendicular to the AP plane. The pressure measurement sites were selected based on the geometry of each subject’s stump, rather than at specific pre-defined locations. It should be noted that these locations are important, as a small shift would result in a different pressure reading.

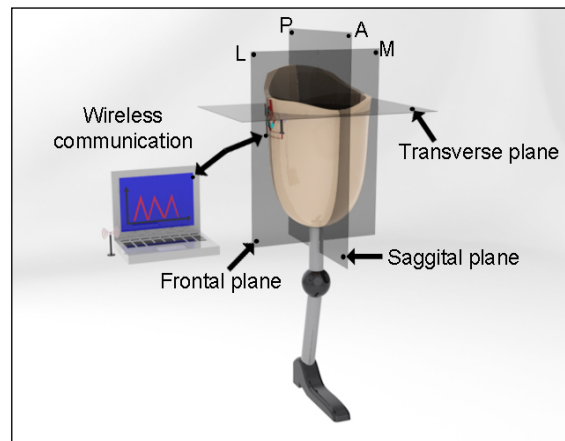


Figure 7.3: Identification of the planes of the body.

Without looking for in detail explanation or clinical relevance on these initial results, several comments and analysis can be carried out. This study was designed to evaluate the viability of the transducers and to the possible problems associated with mounting the transducers and the collection of data. Both anterior–posterior (AP) and medial–lateral (ML) planes would be regarded by the prosthetics as areas premeditated to take load. During the data acquisition session the signal was acquired via RF and the transducers measured skin–sock interface pressures on the socket surface Figure 7.4.

Subject #1

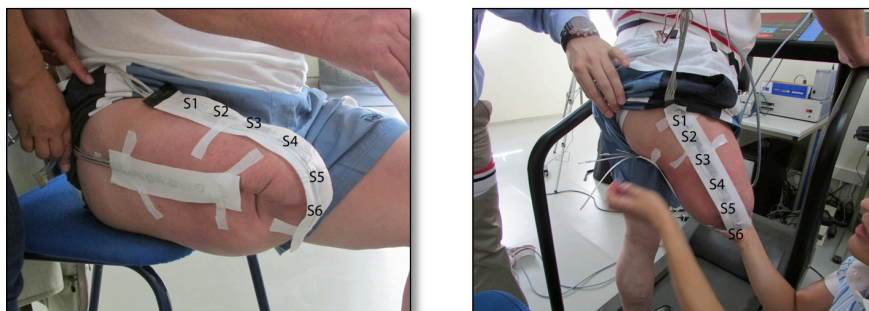


Figure 7.4: Transducers placed at different planes of the body, subject #1.

Figure 7.5 shows typical example of the tests in both anterior–posterior (AP) and medial–lateral (ML) planes for de subject #1.

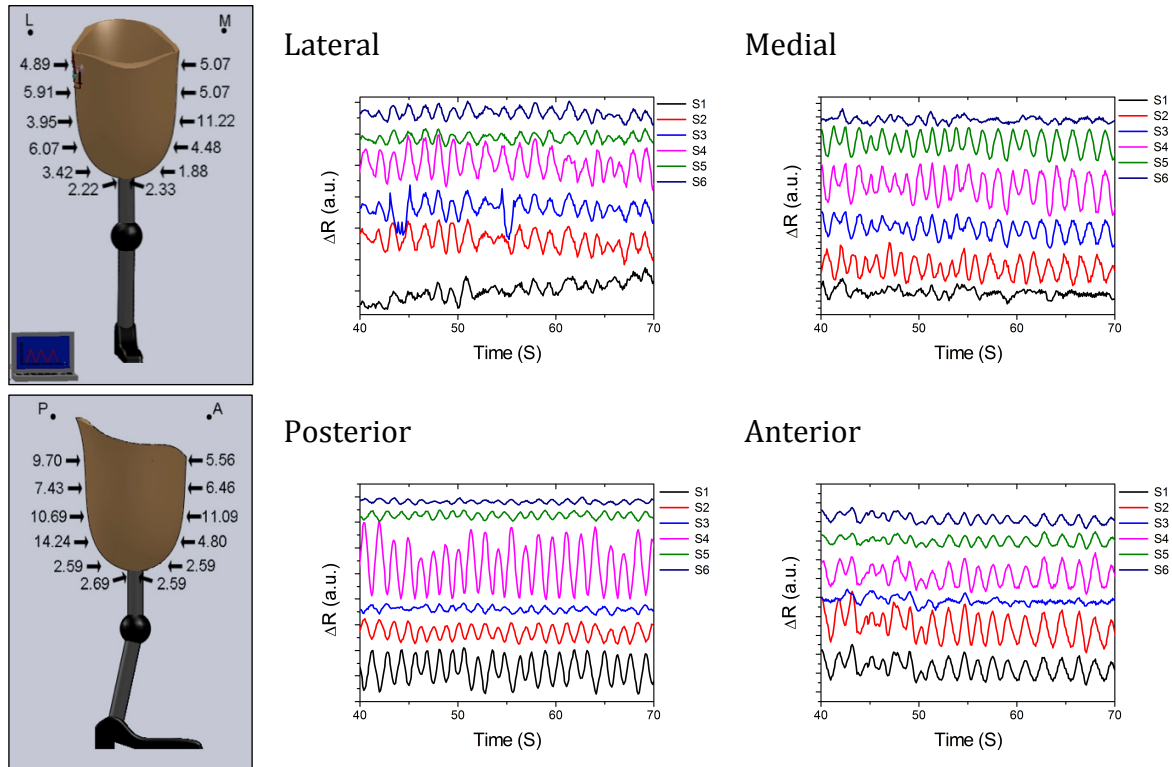
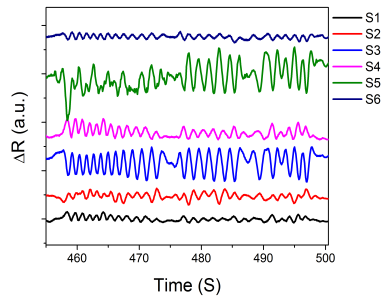
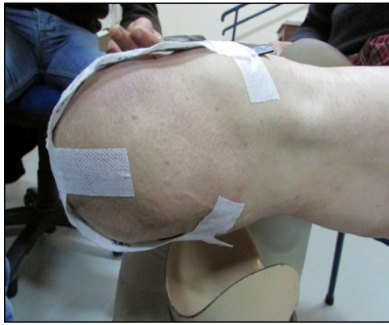


Figure 7.5: Pressure measured at the stump/sock/socket interface.

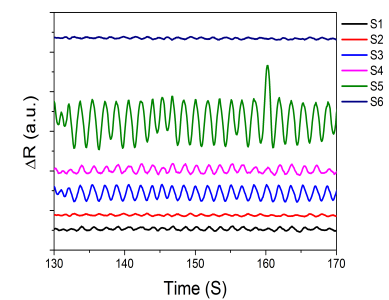
The initial peak occurring shortly after heel strike on the prosthetic side and the second later in stance, resemble typical reaction force traces caused by the rapid deceleration of the body as the foot lands, followed by an acceleration reaction during push-off. It can be seen the relative differences corresponding to the four patients were the distribution of pressure is more uniform for the subject #4, Figure 7.6, and less distributed to the subjects #1, Figure 7.5, and #2, Figure 7.6. In the case of the subject #3, due the short size of the stump, it is possible see the difference pressure distribution between the planes anterior, (S1, S2, S3) and posterior (S4, S5, S6), Figure 7.6.

Though a consistent pressure profile was not found in this study, it should be emphasized that many factors play an important role in determining each subject's pressure profile, such as stump shape, socket alignment and thigh muscle strength. However, it should still be noted that despite the different pressure profiles, the developed transducers were able to contribute to fabricate more comfortable sockets for these patients by the relative quantification of the forces within the different interface region.

Subject #2



Subject #3



Subject #4

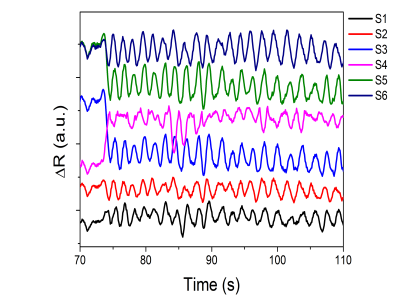


Figure 7.6: Measurements performed at the stump/sock/socket interface.

In the following images, Figure 7.7, it is possible to see the tests carried out at CRPG with a patient, with some details about the sensor system and its placement in the prosthesis.



Figure 7.7: Pressure sensor prototype placement at the stump/sock/socket interface.

7.2. Conclusion

With this work, it was demonstrated that real-time assessment of the stump/socket interface pressure in lower limb amputees (both transtibial and transfemoral) is viable technologically with the use of polymer based piezoresistive transducers. We expect that the present method will become helpful for comprehensively evaluating biomechanical interactions between the residual limb and prosthesis in the clinical setting. The observed results provided good indications that it will be possible to identify areas of critical pressure.

The system developed in this project may allow monitoring of the process of rehabilitation when a new prosthesis is used and will support clinical decisions in relation to the potential effects of modifications on the socket, when adjustments are required. Further developments of the system are possible and recommended in order to fine-tune its use for clinical purposes.



8. General conclusions

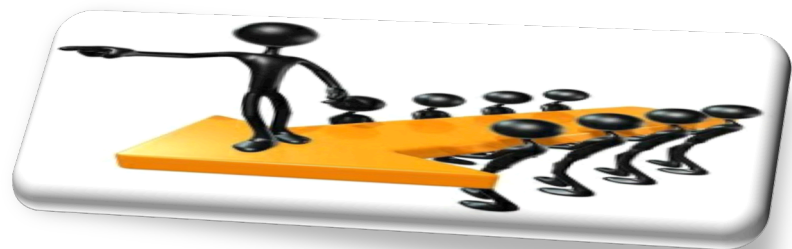
The production and control of lower limb prostheses is mainly performed by qualitative methods. There is a need to improve the quality in selecting, producing, adapting and utilizing the product, using quantitative methods of control. So, the main objective of this work was to develop polymer based piezoresistive materials able to measure force distribution within the socket to help the practitioner to assess the fit of the socket helping to reduce the time and material used on this step and improve substantially the comfort and quality of life of the end user.

For that, transducers based on epoxies and thermoplastics composites filled with carbon nanotubes and nanofibres, were prepared and characterized. These composites were subjected to experimental sets of cyclic loading and unloading simulating normal walking conditions. The electrical and piezoresistive response of epoxies and poly(vinylidene fluoride)/carbon nanotube composites has been reported. The observed electrical and electromechanical responses are in accordance with the framework of the percolation theory. The samples were prepared by hot pressing with CNT sample concentrations up to 10 wt.% loadings. The GF reaches values around 6.2 and the linearity of the response over a wide strain range shows the viability of these materials to be used as piezoresistive sensors.

In the same way, a method for the preparation of large-scale piezoresistive sensors based on spray coating is presented. It is shown that the electrical properties and the electromechanical response of the material are independent of the preparation method: spray-printing or hot-pressing.

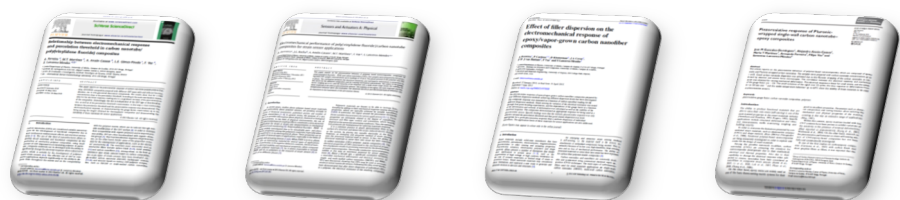
The electrodes for the polymer composites were developed by changing the traditional sputtering deposition of Ti-Ag by GLAD system. Ti-Ag thin films with inclined and zigzag period microstructures were fabricated. Upon uniaxial stretching, for the zigzag structures, the resistance starts increasing for strain up to 3 %. Above 10 % strain it rises sharply up to electrical failure. By increasing the number of zigzags, the electromechanical response is steadily restored and the best results were obtained when the polymer was coated with Ti-Ag films produced with intermediate incident angles ($\alpha = 60^\circ$).

With this project, it was demonstrated that real-time assessment of the stump/socket interface pressure in lower limb amputees (both transtibial and transfemoral) is viable technologically with the use of polymer based piezoresistive transducers.



9. Future work

The obtained results of this work allow to open new lines of study and mechanisms for the future. The inclusion of specific fillers, in proper amounts, into polymer matrices has shown to be advantageous in creating an array of sensors. Further investigation needs an optimization and calibration in this array of sensors. The implementation a functional prototype with integrated sensor calibrated, as well with various patients and conditions. On the other hand, as demonstrated in chapter 7, Ti-Ag thin films can be a next further investigation due the results shows a promising way to use the films as piezoresistive sensors themselves. The obtained results also raise the possibility of up scaling these materials for use into a production scale.



10. Bibliography

1. Centro De Reabilitação Profissional De Gaia, C. and I. Instituto Superior De Ciências Do Trabalho E Da Empresa, *Mais Qualidade de Vida para as Pessoas com Deficiências e Incapacidades*. CRPG – Cen ed. 2007.
2. Gonçalves, C. *Revista de Estudos Demográficos - 1.º Semestre de 2003*. Available from: http://censos.ine.pt/xportal/xmain?xpid=CENSOS&xpgid=ine_censos_estudo_det&menuBOUI=13707294&contexto=es&ESTUDOSest_boui=106259&ESTUDOSmodo=2&selTab=tab1.
3. Beil, T.L., G.M. Street, and S.J. Covey, *Interface pressures during ambulation using suction and vacuum-assisted prosthetic sockets*. Journal Of Rehabilitation Research And Development, 2002. **39**: p. 693-700.
4. Kang, I., et al., *Introduction to carbon nanotube and nanofiber smart materials*. Composites Part B: Engineering, 2006. **37**: p. 382-394.
5. Knite, M., et al., *Reversible Tensile-Resistance and Piezo-Resistance Effects in Conductive Polymer-Carbon Nanocomposites*. Advanced Engineering Materials, 2004. **6**: p. 742-746.
6. Adhikari, B. and S. Majumdar, *Polymers in sensor applications*. Progress in Polymer Science, 2004. **29**: p. 699-766.
7. <http://www.foot-orthotics-prosthetics.co.za/C-leg-certification/C-leg-certification.html>.
8. Novel. 2013 [cited 2013 11-12]; Available from: <http://novel.de/novelcontent/sensors>.
9. Tekscan. Available from: <http://www.tekscan.com/products>.
10. PAM. *Sensors PAM*. 2013 [cited 2013 11-12]; Available from: <http://www.pam.com/index.php?pid=3>.
11. Mak, A.F.T., M. Zhang, and D.A. Boone, *State-of-the-art research in lower-limb prosthetic biomechanics-socket interface*. Journal Of Rehabilitation Research And Development, 2001. **38**.
12. Polliack, A.A., et al., *Scientific validation of two commercial pressure sensor systems for prosthetic socket fit*. Prosthetics and Orthotics International, 2000. **24**: p. 63-73.
13. Urry, S.R. and S.C. Wearing, *A Comparison of Footprint Indexes Calculated from Ink and Electronic Footprints*. Journal of the American Podiatric Medical Association, 2001. **91**: p. 203-209.
14. Luo, S. and T. Liu, *Structure-property-processing relationships of single-wall carbon nanotube thin film piezoresistive sensors*. Carbon, 2013. **59**(0): p. 315-324.
15. Lefort, M., et al., *Spray-On Organic/Inorganic Films: A General Method for the Formation of Functional Nano- to Microscale Coatings*. Angewandte Chemie International Edition, 2010. **49**(52): p. 10110-10113.
16. Chan, C.K., et al., *High performance airbrushed organic thin film transistors*. Applied Physics Letters, 2010. **96**(13): p. -.
17. Timoshenko, S.P., *Strength of Materials*. 1958, New York: McGraw-Hill, Inc. 93-218.
18. Reilly, C.J. and J. John E. Sanchez, *The piezoresistance of aluminum alloy interconnect structures*. Journal of Applied Physics, 1999. **85**(3): p. 1943-1948.
19. Rowe, A.C.H., et al., *Giant Room-Temperature Piezoresistance in a Metal-Silicon Hybrid Structure*. Physical Review Letters, 2008. **100**(14): p. 145501.
20. Wagner, S., et al., *Electronic skin: architecture and components*. Physica E: Low-dimensional Systems and Nanostructures, 2004. **25**(2-3): p. 326-334.

21. Lacour, S.P., et al., *Stiff subcircuit islands of diamondlike carbon for stretchable electronics*. Journal of Applied Physics, 2006. **100**(1): p. 014913.
22. Gray, D.S., J. Tien, and C.S. Chen, *High-Conductivity Elastomeric Electronics*. Advanced Materials, 2004. **16**(5): p. 393-397.
23. Pelrine, R., et al., *High-field deformation of elastomeric dielectrics for actuators*. Materials Science and Engineering: C, 2000. **11**(2): p. 89-100.
24. Gonzalez, M., et al., *Design of metal interconnects for stretchable electronic circuits*. Medical Biology (Helsinki), 2008. **48**: p. 825-832.
25. Ripka, P. and A. Tipek, *Modern sensors handbook*. 2007: ISTE Ltd.
26. Correia, V., et al., *Development of inkjet printed strain sensors*. Smart Materials and Structures, 2013. **22**(10): p. 105028.
27. Bauhofer, W. and J.Z. Kovacs, *A review and analysis of electrical percolation in carbon nanotube polymer composites*. Composites Science and Technology, 2009. **69**(10): p. 1486-1498.
28. Choi, S. and Z. Jiang, *A novel wearable sensor device with conductive fabric and PVDF film for monitoring cardiorespiratory signals*. Sensors and Actuators A: Physical, 2006. **128**: p. 317-326.
29. De Rosa, I.M. and F. Sarasini, *Use of PVDF as acoustic emission sensor for in situ monitoring of mechanical behaviour of glass/epoxy laminates*. Polymer Testing, 2010. **29**: p. 749-758.
30. Peng, P., et al., *Novel MEMS stiffness sensor for force and elasticity measurements*. Sensors and Actuators A: Physical, 2010. **158**: p. 10-17.
31. Dargahi, J., *A piezoelectric tactile sensor with three sensing elements for robotic, endoscopic and prosthetic applications*. Sensors and Actuators A: Physical, 2000. **80**: p. 23-30.
32. Zavickis, J., et al., *Development of percolative electroconductive structure in piezoresistive polyisoprene-nanostructured carbon composite during vulcanization*. Materials Science and Engineering: C, 2011. **31**: p. 472-476.
33. Sau, K.P., T.K. Chaki, and D. Khastgir, *The change in conductivity of a rubber-carbon black composite subjected to different modes of pre-strain*. Composites Part A: Applied Science and Manufacturing, 1998. **29**(4): p. 363-370.
34. Wang, L., T. Ding, and P. Wang, *Effects of compression cycles and precompression pressure on the repeatability of piezoresistivity for carbon black-filled silicone rubber composite*. Journal of Polymer Science Part B: Polymer Physics, 2008. **46**(11): p. 1050-1061.
35. Zhang, X.-W., et al., *Time dependence of piezoresistance for the conductor-filled polymer composites*. Journal of Polymer Science Part B: Polymer Physics, 2000. **38**(21): p. 2739-2749.
36. Ferreira, A., et al., *Effect of filler dispersion on the electromechanical response of epoxy/vapor-grown carbon nanofiber composites*. Smart Materials and Structures, 2012. **21**(7).
37. Kang, I., et al., *Introduction to carbon nanotube and nanofiber smart materials*. Composites Part B: Engineering, 2006. **37**(6): p. 382-394.
38. Simoes, R., et al., *Low percolation transitions in carbon nanotube networks dispersed in a polymer matrix: dielectric properties, simulations and experiments*. Nanotechnology, 2009. **20**: p. 035703.

39. Paleo, a.J., et al., *The piezoresistive effect in polypropylene—carbon nanofibre composites obtained by shear extrusion*. Smart Materials and Structures, 2010. **19**: p. 065013.
40. Cardoso, P., et al., *The role of disorder on the AC and DC electrical conductivity of vapour grown carbon nanofibre/epoxy composites*. Composites Science and Technology, 2012. **72**(2): p. 243-247.
41. Stauffer, D. and A. Aharony, *Introduction to Percolation Theory*. 2 ed. 1992, London: Taylor and Francis.
42. Stroud, D. and D.J. Bergman, *Frequency dependence of the polarization catastrophe at a metal-insulator transition and related problems*. 1982. **25**: p. 2061-2064.
43. Nan, C.-W., *Physics of inhomogeneous inorganic materials*. Progress in Materials Science, 1993. **37**: p. 1-116.
44. Park, M., H. Kim, and J.P. Youngblood, *Strain-dependent electrical resistance of multi-walled carbon nanotube/polymer composite films*. Nanotechnology, 2008. **19**(5): p. 055705.
45. Pham, G.T., et al., *Processing and modeling of conductive thermoplastic/carbon nanotube films for strain sensing*. Composites Part B: Engineering, 2008. **39**(1): p. 209-216.
46. Hu, N., et al., *Tunneling effect in a polymer/carbon nanotube nanocomposite strain sensor*. Acta Materialia, 2008. **56**: p. 2929-2936.
47. Wichmann, M.H.G., et al., *Piezoresistive response of epoxy composites with carbon nanoparticles under tensile load*. Physical Review B, 2009. **80**: p. 1-8.
48. Yasuoka, T., Y. Shimamura, and A. Todoroki, *Electrical Resistance Change under Strain of CNF/Flexible-Epoxy Composite*. Advanced Composite Materials, 2010. **19**: p. 123-129.
49. Dharap, P., et al., *Nanotube film based on single-wall carbon nanotubes for strain sensing*. Nanotechnology, 2004. **15**(3): p. 379.
50. Kang, I., et al., *A carbon nanotube strain sensor for structural health monitoring*. Smart Materials and Structures, 2006. **15**(3): p. 737.
51. Zhang, W., J. Suhr, and N. Koratkar, *Carbon nanotube/polycarbonate composites as multifunctional strain sensors*. Journal of Nanoscience and Nanotechnology, 2006. **6**: p. 960-964.
52. Ferreira, A., et al., *Electromechanical performance of poly(vinylidene fluoride)/carbon nanotube composites for strain sensor applications*. Sensors and Actuators A: Physical, 2012. **178**(0): p. 10-16.
53. Kang, I., et al., *The bulk piezoresistive characteristics of carbon nanotube composites for strain sensing of structures*. Journal of Nanoscience and Nanotechnology, 2007. **7**: p. 3736-3739.
54. Rein, M.D., O. Breuer, and H.D. Wagner, *Sensors and sensitivity: Carbon nanotube buckypaper films as strain sensing devices*. Composites Science and Technology, 2011. **71**: p. 373-381.
55. Pham, G.T., et al., *Processing and modeling of conductive thermoplastic/carbon nanotube films for strain sensing*. Polymer, 2008. **39**: p. 209-216.
56. Li, C., E. Thostenson, and T. Chou, *Sensors and actuators based on carbon nanotubes and their composites: A review*. Composites Science and Technology, 2008. **68**: p. 1227-1249.
57. Ferreira, A., et al., *Relationship between electromechanical response and percolation threshold in carbon nanotube/poly(vinylidene fluoride) composites*. Carbon, 2013. **61**(0): p. 568-576.

58. Deshpande, S.D., K. Jaehwan, and Y. Sung-Ryul, *Studies on conducting polymer electroactive paper actuators: effect of humidity and electrode thickness*. Smart Materials and Structures, 2005. **14**(4): p. 876.
59. Richardson-Burns, S.M., et al., *Polymerization of the conducting polymer poly(3,4-ethylenedioxythiophene) (PEDOT) around living neural cells*. Biomaterials, 2007. **28**(8): p. 1539-1552.
60. Rosset, S. and H. Shea, *Flexible and stretchable electrodes for dielectric elastomer actuators*. Applied Physics A, 2013. **110**(2): p. 281-307.
61. Thornton, J.A., *The microstructure of sputter-deposited coatings*. Journal of Vacuum Science & Technology A: Vacuum, Surfaces, and Films, 1986. **4**(6): p. 3059.
62. Messier, R., *Revised structure zone model for thin film physical structure*. Journal of Vacuum Science & Technology A: Vacuum, Surfaces, and Films, 1984. **2**(2): p. 500.
63. Petrov, I., et al., *Microstructural evolution during film growth*. Journal of Vacuum Science & Technology A: Vacuum, Surfaces, and Films, 2003. **21**(5): p. S117.
64. Mahieu, S., et al., *Biaxial alignment in sputter deposited thin films*. Thin Solid Films, 2006. **515**(4): p. 1229-1249.
65. Knorr, T.G. and R.W. Hoffman, *Dependence of Geometric Magnetic Anisotropy in Thin Iron films*. Physical Review, 1959. **113**(4): p. 1039-1046.
66. Lopes, C., et al., *TiAgx thin films for lower limb prosthesis pressure sensors: Effect of composition and structural changes on the electrical and thermal response of the films*. Appl. Surf. Sci., 2013. **285**, Part A: p. 10-18.
67. Gonçalves, C., et al., *Structural and morphological evolution in TiAgx thin films as a function of in-vacuum thermal annealing* Journal of Nano Research, 2013. **25**: p. 67-76.
68. Ewald, A., et al., *Antimicrobial titanium/silver PVD coatings on titanium*. Biomed Eng Online, 2006. **5**: p. 1-10.
69. Takahashi, M., et al., *Grindability and mechanical properties of experimental Ti-Au, Ti-Ag and Ti-Cu alloys*. International Congress Series, 2005. **1284**: p. 326-327.
70. Kikuchi, M., M. Takahashi, and O. Okuno, *Machinability of Experimental Ti-Ag Alloys*. Dental Materials Journal, 2008. **27**(2): p. 216-220.
71. Martínez, M.T., et al., *Sensitivity of single wall carbon nanotubes to oxidative processing: structural modification, intercalation and functionalisation*. Carbon, 2003. **41**: p. 2247-2256.
72. Ansón-Casaos, A., et al., *Surfactant-free assembling of functionalized single-walled carbon nanotube buckypapers*. Carbon, 2010. **48**: p. 1480-1488.
73. Blanch, A.J., C.E. Lenahan, and J.S. Quinton, *Parametric analysis of sonication and centrifugation variables for dispersion of single walled carbon nanotubes in aqueous solutions of sodium dodecylbenzene sulfonate*. Carbon, 2011. **49**(15): p. 5213-5228.
74. Ansón-Casaos, A., et al., *Choosing the Chemical Route for Carbon Nanotube Integration in Poly(vinylidene fluoride)*. The Journal of Physical Chemistry C, 2012. **116**(30): p. 16217-16225.
75. Ansón-Casaos, A., et al., *Influence of air oxidation on the surfactant-assisted purification of single-walled carbon nanotubes*. Langmuir : the ACS journal of surfaces and colloids, 2011. **27**: p. 7192-8.
76. Itkis, M.E., et al., *Purity Evaluation of As-Prepared Single-Walled Carbon Nanotube Soot by Use of Solution-Phase Near-IR Spectroscopy*. Nano Letters, 2003. **3**: p. 309-314.

77. Ansón-Casaos, A., J.M. González-Domínguez, and M.T. Martínez, *Separation of single-walled carbon nanotubes from graphite by centrifugation in a surfactant or in polymer solutions*. Carbon, 2010. **48**: p. 2917-2924.
78. Bottino, A., et al., *Solubility parameters of poly(vinylidene fluoride)*. Journal of Polymer Science Part B: Polymer Physics, 1988. **26**: p. 785-794.
79. Beeby, S., et al., *MEMS mechanical sensors*. 2004, Boston: Artech House.
80. González-Domínguez, J.M., et al., *Solvent-Free Preparation of High-Toughness Epoxy-SWNT Composite Materials*. ACS Applied Materials & Interfaces, 2011. **3**: p. 1441-1450.
81. Cardoso, P., et al., *The dominant role of tunneling in the conductivity of carbon nanofiber-epoxy composites*. Physica Status Solidi (a), 2010. **207**: p. 407-410.
82. Alsaleh, M. and U. Sundararaj, *A review of vapor grown carbon nanofiber/polymer conductive composites*. Carbon, 2009. **47**: p. 2-22.
83. Yui, H., et al., *Morphology and electrical conductivity of injection-molded polypropylene/carbon black composites with addition of high-density polyethylene*. Polymer, 2006. **47**: p. 3599-3608.
84. Bar, H., M. Narkis, and G. Boiteux, *The electrical behavior of thermosetting polymer composites containing metal plated ceramic filler*. Polymer Composites, 2005. **26**: p. 12-19.
85. Wichmann, M.H.G., et al., *Direction sensitive bending sensors based on multi-wall carbon nanotube/epoxy nanocomposites*. Nanotechnology, 2008. **19**: p. 475503.
86. Foreman, J., et al., *Hierarchical modelling of a polymer matrix composite*. Journal of Materials Science, 2008. **43**(20): p. 6642-6650.
87. Wang, L. and Z.-M. Dang, *Carbon nanotube composites with high dielectric constant at low percolation threshold*. Applied Physics Letters, 2005. **87**: p. 042903.
88. Carmona, F., R. Canet, and P. Delhaes, *Piezoresistivity of heterogeneous solids*. Journal of Applied Physics, 1987. **61**: p. 2550, 2557.
89. Celzard, A., et al., *Conduction mechanisms in some graphite-polymer composites: Effects of temperature and hydrostatic pressure*. Journal of Applied Physics, 1998. **83**: p. 1410.
90. Tamulevich, T.W. and V.E. Moore. *The Significance Of Glass Transition Temperature on epoxy Resins for Fiber Applications*. in *Fiber Optics Weekly Update*. 1980. Information Gatekeepers Inc.
91. Wisanrakkit, G. and J.K. Gillham, *The glass transition temperature (T_g) as an index of chemical conversion for a high-T_g amine/epoxy system: Chemical and diffusion-controlled reaction kinetics*. Journal of Applied Polymer Science, 1990. **41**: p. 2885-2929.
92. Zhou, J., *Hygrothermal effects of epoxy resin. Part II: variations of glass transition temperature*. Polymer, 1999. **40**: p. 5513-5522.
93. Gregorio, R. and E.M. Ueno, *Effect of crystalline phase, orientation and temperature on the dielectric properties of poly (vinylidene fluoride) (PVDF)*. Journal of Materials Science, 1999. **34**: p. 4489-4500.
94. Costa, P., et al., *The effect of fibre concentration on the α to β -phase transformation, degree of crystallinity and electrical properties of vapour grown carbon nanofibre/poly(vinylidene fluoride) composites*. Carbon, 2009. **47**: p. 2590-2599.

95. Lin, L., et al., *Modified resistivity-strain behavior through the incorporation of metallic particles in conductive polymer composite fibers containing carbon nanotubes*. Polymer International, 2013. **62**(1): p. 134-140.
96. Silva, J., et al., *Applying complex network theory to the understanding of high-aspect-ratio carbon-filled composites*. EPL (Europhysics Letters), 2011. **93**(3): p. 37005.
97. Rahman, R. and P. Servati, *Effects of inter-tube distance and alignment on tunnelling resistance and strain sensitivity of nanotube/polymer composite films*. Nanotechnology, 2012. **23**(5): p. 055703.
98. Chekanov, Y., et al., *Electrical properties of epoxy resin filled with carbon fibers*. Chemical Physics, 1999. **4**: p. 5589 - 5592.
99. Miller, B., *Plastics World*. 1996. 73.
100. Kang, J.H., et al., *Piezoresistive characteristics of single wall carbon nanotube/polyimide nanocomposites*. Journal of Polymer Science Part B: Polymer Physics, 2009. **47**(16): p. 1635-1636.
101. Mano, J., et al., *Dynamic mechanical analysis and creep behaviour of β -PVDF films*. Materials Science and Engineering A, 2004. **370**: p. 336-340.
102. Grimaldi, C., P. Ryser, and S. Straessler, *Gauge factor enhancement driven by heterogeneity in thick-film resistors*. 2000: p. 6.
103. Grimaldi, C., et al., *Piezoresistivity and conductance anisotropy of tunneling-percolating systems*. Production, 2002: p. 6.
104. Cao, C.L., et al., *Temperature dependent piezoresistive effect of multi-walled carbon nanotube films*. Diamond and Related Materials, 2007. **16**(2): p. 388-392.
105. Sheng, P., *Fluctuation-induced tunneling conduction in disordered materials*. Physical Review B, 1980. **21**(6): p. 2180-2195.
106. Dawson, J.C. and C.J. Adkins, *Conduction mechanisms in carbon-loaded composites*. Journal of Physics: Condensed Matter, 1996. **8**(43): p. 8321.
107. Moonen, P.F., I. Yakimets, and J. Huskens, *Fabrication of Transistors on Flexible Substrates: from Mass-Printing to High-Resolution Alternative Lithography Strategies*. Advanced Materials, 2012. **24**(41): p. 5526-5541.
108. Stutzmann, N., R.H. Friend, and H. Sirringhaus, *Self-Aligned, Vertical-Channel, Polymer Field-Effect Transistors*. Science, 2003. **299**(5614): p. 1881-1884.
109. Stroud, D. and D.J. Bergman, *Frequency dependence of the polarization catastrophe at a metal-insulator transition and related problems*. Physical Review B, 1982. **25**(3): p. 2061-2064.
110. Ferreira, A., et al., *Relationship between electromechanical response and percolation threshold in carbon nanotube/poly(vinylidene fluoride) composites*. Carbon, 2013(0).
111. Chekanov, Y., et al., *Electrical properties of epoxy resin filled with carbon fibers*. Journal of Materials Science, 1999. **34**(22): p. 5589-5592.
112. Hou, Y., et al., *Positive piezoresistive behavior of electrically conductive alkyl-functionalized graphene/polydimethylsilicone nanocomposites*. Journal of Materials Chemistry C, 2013. **1**(3): p. 515-521.
113. Costa, P., et al., *Mechanical, electrical and electro-mechanical properties of thermoplastic elastomer styrene-butadiene-styrene/multiwall carbon nanotubes composites*. Journal of Materials Science, 2013. **48**(3): p. 1172-1179.

114. Pauw, L.J.v.d., *A method of measuring specific resistivity and hall effect of discs of arbitrary shape*. 1958. **13**: p. 1-9.
115. Pauw, L.J.v.d., *A method of measuring the resistivity and hall coefficient on lamellae of arbitrary shape*. Philips Technical Review, 1958. **20**: p. 220-224.
116. Lintymer, J., et al., *Glancing angle deposition to modify microstructure and properties of sputter deposited chromium thin films*. Surface and Coatings Technology, 2003. **174-175**: p. 316-323.
117. Lintymer, J., et al., *Glancing angle deposition to control microstructure and roughness of chromium thin films*. Wear, 2008. **264**(5-6): p. 444-449.
118. Pedrosa, P., et al., *Electrical characterization of Ag:TiN thin films produced by glancing angle deposition*. Materials Letters, 2014. **115**: p. 136-139.
119. Rauch, J.-Y., et al., *METAL-TO-DIELECTRIC TRANSITION INDUCED BY ANNEALING OF ORIENTED TITANIUM THIN FILMS*. Functional Materials Letters, 2013. **06**(01): p. 1250051.
120. Mayadas, A.F. and M. Shatzkes, *Electrical-Resistivity Model for Polycrystalline Films: the Case of Arbitrary Reflection at External Surfaces*. Physical Review B, 1970. **1**(4): p. 1382-1389.
121. Sluis, O.v.d., et al., *Stretching-induced interconnect delamination in stretchable electronic circuits*. Journal of Physics D: Applied Physics, 2011. **44**(3): p. 034008.
122. Shokuhfar, A., et al., *Low-cost polymeric microcantilever sensor with titanium as piezoresistive material*. Microelectronic Engineering, 2012. **98**(0): p. 338-342.